PASSIVE NOSETIP TECHNOLOGY (PANT) PROGRAM

VOLUME XVIII. NOSETIP ANALYSES USING THE EROS COMPUTER CODE

ACUREX CORPORATION

PREPARED FOR
SPACE AND MISSILE SYSTEMS ORGANIZATION

JUNE 1975

SAMSO-TR-74-86
Volume XVIII

INTERIM REPORT
PASSIVE NOSETIP TECHNOLOGY
(PANT) PROGRAM

Volume XVIII. Nosetip Analyses Using the EROS Computer Code

G. J. Neuner
N. R. Wool
R. A. Berry

Aerotherm Division/Acurex Corporation

SAMSO-TR-74-86

June 1975

AEROTHERM REPORT 74-100

Air Force Space and Missile
Systems Organization
Los Angeles, California

Contract F04701-74-C-0069

SAMSO-TR-74-86
Volume XVIII

C/N 7102.137

INTERIM REPORT
PASSIVE NOSETIP TECHNOLOGY
(PANT) PROGRAM

Volume XVIII. Nosetip Analyses Using the EROS Computer Code

G. J. Neuner
M. R. Wool
R. A. Berry

Letter on File

FOREWORD

This document is Volume XVIII of the Interim Report series for the Passive Nosetip Technology (PANT) program. A summary of the documents in this series prepared to date is as follows:

Volume I – Program Overview (U)

Volume II – Environment and Material Response Procedures for Nosetip Design (U)

Volume III – Surface Roughness Data

- Part I – Experimental Data
- Part II – Roughness Augmented Heating Data Correlation and Analysis (U)
- Part III – Boundary Layer Transition Data Correlation and Analysis (U)

Volume IV – Heat Transfer and Pressure Distributions on Ablated Shapes

- Part I Experimental Data
- Part II – Data Correlation

Volume V – Definition of Shape Change Phenomenology from Low Temperature Ablator Experiments

- Part I – Experimental Data, Series C (Preliminary Test Series)
- Part II – Experimental Data, Series D (Final Test Series)

Volume VI – Graphite Ablation Data Correlation and Analysis (U)

Volume VII – Computer User's Manual, Steady-State Analysis of Ablating Nosetips (SAANT) Program

Volume VIII – Computer User's Manual, Passive Graphite Ablating Nosetip (PAGAN) Program

Volume IX – Unsteady Flow on Ablated Nosetip Shapes – PANT Series G Test and Analysis Report

Volume X – Summary of Experimental and Analytical Results for the Period May 1973 to December 1974.

Volume XI – Analysis and Review of the ABRES Combustion Test Facility for High Pressure Hyperthermal Reentry Nosetip Systems Tests

Volume XII – Nosetip Transition and Shape Change Tests in the AFFDL 50 MW RENT Arc – Data Report

Volume XIII – An Experimental Study to Evaluate Heat Transfer Rates to Scalloped Surfaces – Data Report

Volume XIV – An Experimental Study to Evaluate the Irregular Nosetip Shape Regime – Data Report

Volume XV – Roughness Induced Transition Experiments – Data Report

Volume XVI – Investigation of Erosion Mechanics on Reentry Materials (U)

Volume XVII – Computer User's Manual, Erosion Shape (EROS) Computer Program

Volume XVIII – Nosetip Analyses Using the EROS Computer Program

This report series was prepared by Aerotherm Division/Acurex Corporation under Contract F04701-71-C-0027. Volumes I through IX covered PANT activities from April 1971 through April 1973. Volumes X through XV represent contract efforts from May 1973 to December 1974. Volumex XVI through XVIII describe the background, development, and checkout of the PANT EROsion Shape (EROS) computer code and document efforts performed under supplementary agreements to the Minuteman Natural Hazards Assessment program (Contract F04701-74-C-0069) between April 1974 and March 1975.

This work was administered under the direction of the Space and Missile Systems Organization with Lieutenant A. T. Hopkins and Lieutenant E. G. Taylor as Project Officers with Mr. W. Portenier and Dr. R. L. Baker of the Aerospace Corporation serving as principal technical monitors. Mr. D. L. Baker was Aerotherm Program Manager and Mr. M. R. Wool was Aerotherm Project Engineer. Mr. G. J. Neuner was principal Aerotherm investigator for the work described in this volume.

This technical report has been reviewed and is approved.

Edward G Taylor

E. G. Taylor, Lt., USAF
Project Officer
Aero and Materials Division
Directorate of Systems Engineering
Deputy for Reentry Systems

ABSTRACT

The results of nosetip response calculations using the newly-developed, EROsion Shape (EROS) computer code are documented. The code enables the evaluation of nosetip coupled erosion and ablation and shape change for arbitrary materials including fine weave carbon/carbon, polycrystalline graphite, and reinforced phenolics. Transient heat conduction is also treated through an innovative explicit differencing scheme. Calculations are presented for wind tunnel test environments, ICBM clear air flight conditions, and Terrier-Recruit sounding rocket flight conditions. In the analysis matrix, modeling techniques are varied to identify response sensitivity to modeling uncertainties.

The primary conclusions are that:

- Transition altitude and overall recession of ICBM nosetips in clear air are critically sensitive to material roughness characteristics.
- Hydrometeor impacts cause significant nosetip erosion mass loss and increased surface thermochemical mass loss.

TABLE OF CONTENTS

LIST OF ILLUSTRATIONS

LIST OF ILLUSTRATIONS (Concluded)

LIST OF TABLES

SECTION 1

INTRODUCTION

Nosetip ablation and erosion performance is critical to the survival of high performance ICBM reentry vehicle systems. Analytical procedures have been developed under the Passive Nosetip Technology (PANT) program (Contract F04701-71-C-0027) and the Minuteman Natural Hazards Assessment Program (Contract F04701-74-C-0069) to evaluate nosetip design concepts and to assess survival probabilities. The most recent nosetip shape and thermal analysis code includes the hydrometeor effects modeling described in Reference 1 and a transient heat conduction package described in Reference 2. The code is entitled EROsion Shape (EROS) computer program, and Reference 3 is the computer user's manual. Results generated during the preliminary exercise of the code are presented herein.

Solutions have been obtained for conditions corresponding to:

- Pressure, calorimeter, and shape change tests from PANT wind tunnel series
- Sounding rocket erosion-ablation flight environments
- ICBM flight environments

The comparisons, included herein, between data and code results for a wide range of modeling assumptions and variations provide insight into the validity and consistency of the computational tool. The majority of solutions were performed for a material that is well characterized and typical of advanced nosetip design. Shape change solutions were also performed for a SAMS carbon/carbon composite nosetip and a SAMS carbon phenolic nosetip.

Section 2 presents a brief summary of the EROS code features. Clear air flight and ground test solutions showing response sensitivity to modeling perturbations are given in Section 3, and weather related sensitivity analyses are presented in Section 4. Carbon/carbon composite and carbon phenolic weather response solutions are presented in Section 5, and conclusions are summarized in Section 6.

SECTION 2

ABLATION/SHAPE CHANGE ANALYSIS PROCEDURES

The EROsion Shape (EROS) computer code combines the environmental modeling techniques developed under the PANT and Natural Hazards Assessment Program with the in-depth transient conduction routines developed at the Aerospace Corporation. This code numerically models the shape history of an ablating nosetip being subjected to a reentry environment. The code calculates the inviscid flow and heat transfer distribution for arbitrarily-shaped, axisymmetric, blunt bodies in hypersonic flow. In addition, the boundary layer and heat transfer distributions are modeled for a variety of environments including the effects of hydrometer erosion. Two material response prediction techniques are available:

- Steady state surface energy balance
- A surface energy balance fully coupled to the in-depth transient thermal response

The in-depth thermal response is capable of calculating the three-dimensional temperature field and surface recession of nosetips at angle of attack. However, since the environment package is limited to axisymmetric geometries, the present code is restricted to nosetips at zero angle of attack. Three additional assumptions implicit in the formulation of these computerized ablation/shape change analyses procedures are as follows:

- Flow separations do not occur
- Oscillatory inviscid flow fields do not develop
- Secondary shocks do not occur

The elements of shape change analyses in the EROS code are illustrated in the computation procedure sketch in Figure 2-1. Brief descriptions of each of these elements are presented in this section. The inviscid flow field modeling is described in Section 2.1. Boundary layer analysis procedures are discussed in Section 2.2. The graphite ablation model is summarized in Section 2.3 with a description of the body movement and shape redefinition procedures in Section 2.4. Erosion modeling capabilities are reviewed in Section 2.5.

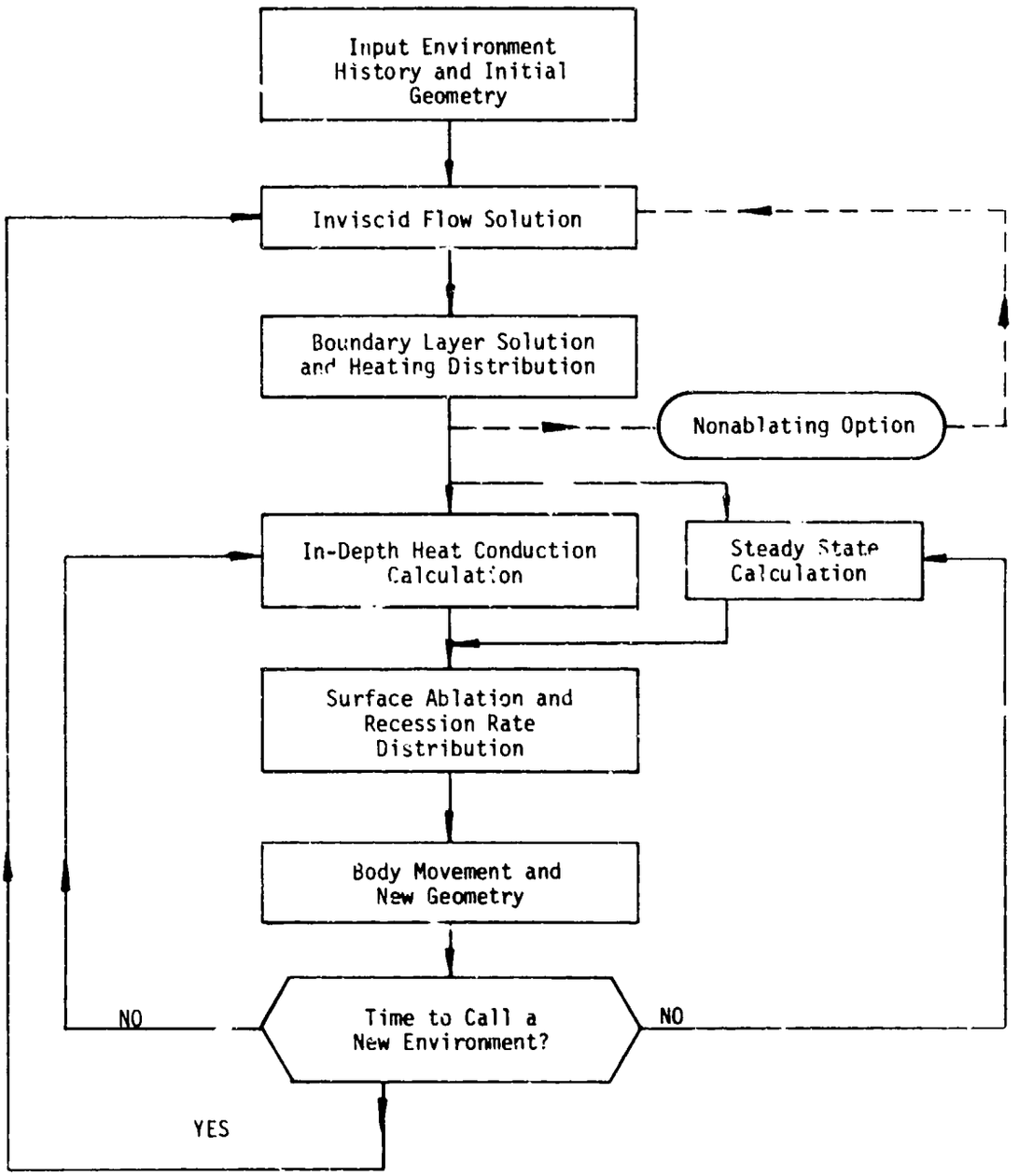

Figure 2-1. Nosetip shape change calculation procedure.

2.1 INVISCID FLOW FIELD

Calculation of the inviscid flow field over an ablating shape provides the required boundary conditions for the boundary layer solution. One aspect of the inviscid flow field solution in the PANT computer codes is the pressure distribution calculation. The pressure distribution over a nosetip contour is calculated based on regional correlations, defined as (1) subsonic forebody, (2) supersonic forebody including recompression, and (3) the aft body. The pressure distribution in the subsonic region depends upon the free stream Mach number. The correlation in this region is an empirical extension and synthesis of the modified Newtonian correlation, valid for spheres, but including a correlation for flat faced cylinders. This correlation strongly depends on the sonic point location which is evaluated assuming modified Newtonian flow with perturbations in the nominal solution depending on (1) free stream Mach number, (2) specific heat ratio, (3) nosetip bluntness, and (4) surface streamline recompression on biconic shapes.

On the supersonic forebody of the nosetip, pressure distributions are computed either using the modified Newtonian expression, or for biconic type configurations, using a conic surface recompression correlation. The cone recompression model is based on sphere/cone and ellipsoid/cone exact solutions performed at various Mach numbers.

The correlation for aft cone pressures is one developed at the Aerospace Corporation (Reference 4). Its form is such that the predicted conic pressure asymptotically approaches the sharp cone value. Coupling the three regimes into a continuous distribution is achieved by a smoothing technique based on a weighted average of the incremental modified Newtonian expression and a linear decay expression. Details regarding the various aspects of the pressure distribution correlations are available in Reference 3.

2.2 BOUNDARY LAYER HEAT AND MASS TRANSFER

The boundary layer heat and mass transport events are modeled using a film coefficient approach. The two aspects of the heating distribution predictions which were emphasized in the upgrading of the EROS code were (1) transition and transitional flow and (2) rough wall heating perturbations to both laminar and turbulent flow. Development of the transition model is discussed in Reference 5. The laminar and turbulent rough wall heating augmentation models are discussed in Reference 6. The sensitivity of ablation shape change predictions for ATJ-S graphite to uncertainties in the rough wall heating levels and transition location are reviewed in Reference 7.

2.3 THERMOCHEMICAL ABLATION MODEL

In the EROS computer code, the ablation thermochemistry events are modeled by the generalized approach described in Reference 8. Through a tabular coupling to a thermochemistry computer code, the surface energy balance routine can consider any combination of surface material elemental compositions in an air environment. The film coefficient approach enables the modeling of heterogeneous reaction and sublimation kinetics, unequal species diffusion coefficients, and/or unequal heat and mass transfer coefficients. For the case of graphite in air, dominant surface ablation and reaction products include CO, CN, C_2N, C_2N_2, NO, NO_2, CO_2, and carbon vapor species.

2.4 BODY MOVEMENT AND SURFACE SMOOTHING

A significant amount of development work in the area of shape stability and body point movement has occurred within the PANT program. Previous stability problems resulted from surface movement schemes which allowed body point migration toward the stagnation point. The steady state option of the EROS code eliminates these problems by restricting body point movement to be along lines of constant radius. In addition, an effective nose radius scheme is used in the shape change procedure. This specification controls only the detailed shape dependent environmental parameters at the stagnation point and does not limit or redefine the overall nosetip shape. These shape change mechanics and body point movement criteria are fundamental to the computational stability of the EROS code.

2.5 EROSION MODELING

Coupled erosion ablation computations may be performed with the EROS code. Surface erosion due to hydrometeor impacts is currently modeled for graphitic type brittle materials and malleable type metal materials. Various erosion modeling assumptions available in the EROS code are documented in Reference 1 and summarized in Section 4.

SECTION 3

ABLATION AND SHAPE CHANGE MODELING SENSITIVITY STUDIES

The EROS code was exercised to determine code reliability and computational consistency for noneroding environments including wind tunnel tests and clear air flight environments. Solutions were generated for reasonable perturbations to several modeling features which have recently been upgraded and incorporated in the PANT codes (in this case, the EROS code). From these solutions, the sensitivity of the EROS code predictions to key modeling uncertainties was demonstrated, and code numerical difficulties were identified.

In Section 3.1 comparisons with PANT, wind-tunnel test data are presented. Shock shape and heat transfer distributions over ablated-shape calorimeters are shown, and the results of two low-temperature-ablator shape change predictions are compared to data. In Section 3.2, several code calculations for two typical reentry cases are presented. For each flight case, a baseline steady state ablation solution is presented. The effects of perturbed modeling are then referenced to the baseline result.

3.1 COMPARISONS TO PANT WIND TUNNEL TEST DATA

Wind tunnel test data from calorimeter and low-temperature-ablator shape change models provide data to assess the nosetip response methodology in the EROS code. For example, ablated shape calorimeter data from the Series B tests (Reference 9) and the more recent Series J tests (Reference 10) are ideal for evaluating shock shape and heat transfer modeling techniques. In addition, exact, inviscid flow field solutions have been performed for the Series B test geometries at the Mach 5 wind tunnel condition and at a Mach 20 condition. The high Mach number exact solutions enable comparison at flight conditions where data are unavailable.

Four model configurations were selected for analysis of EROS shock shape and heat transfer modeling. These have nosetip profiles characterized as:

- Convex (Series B)
- Concave (Series B)

- 45° conic (Series B)
- 60° conic (Series J)

In each case, a 0.4-inch radius stagnation region fairs into the nosetip profile which fairs into an 8° aft cone. The model profiles are shown along with the computed and measured shock shapes in Figures 3-1 through 3-4.

The EROS modeling of shock shape (Reference 1) includes two improvements over the previous PANT model (Reference 11). First, an alternate shock standoff correlation is used and, second, an improved procedure is used for computing the shock shape downstream of the sonic flow line. No change was made to the subsonic region shock shape computation procedure. The convex shape comparisons in Figure 3-1 demonstrate a large improvement in the shock standoff calculation and a small improvement in overall shape. The comparisons for the concave profile in Figure 3-2 show a substantial improvement in the shock shape both at Mach 5 and 20, whereas Figure 3-3 shows no difference in the results for the 45° biconic. Both the previous model and the EROS model produced an accurate shock shape for the 45° conic. The results for the 60° conic profile in Figure 3-4 are not as good, however. The centerline shock standoff calculation is closer to the data, but, since the subsonic region model was not changed, the overall shock shape in front of this high angle conic was not changed from the previous result. No high Mach number solution was run for the 60° conic.

Smooth wall heat transfer distribution predictions for the convex, concave, and 45 degree conic configurations are compared to SAANT code predictions (Reference 12) and data in Figure 3-5. Of the three, only the 45° conic prediction differs substantially from the SAANT results. The EROS code incorporates the composite heat transfer prediction technique described in Reference 3 and includes different modelings of boundary layer growth, entropy layer swallowing, Reynolds analogy, and, of course shock shape. For the convex and concave shape, the modifications compensated to give similar predictions.

As an exercise of the shape change numerical procedures in the EROS computer code, two camphor shape change solutions were generated for comparison with PANT Series D Runs 207 and 208. The model in Run 207 was tested at a relatively high Reynolds number condition and experienced shape change to a blunt turbulent configuration. Run 208, performed at a lower Reynolds number condition, resulted in a slender shape. Figures 3-6 and 3-7 present the shape and recession predictions for Runs

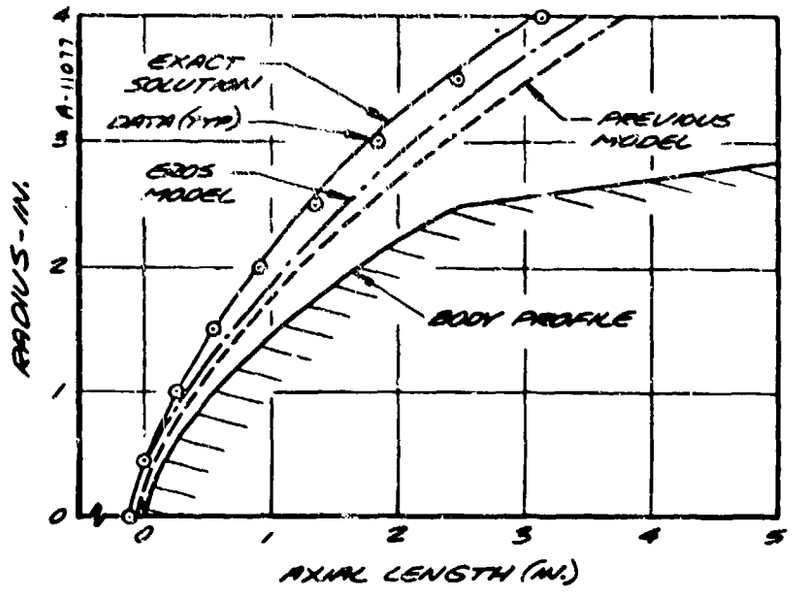

a) Mach 5

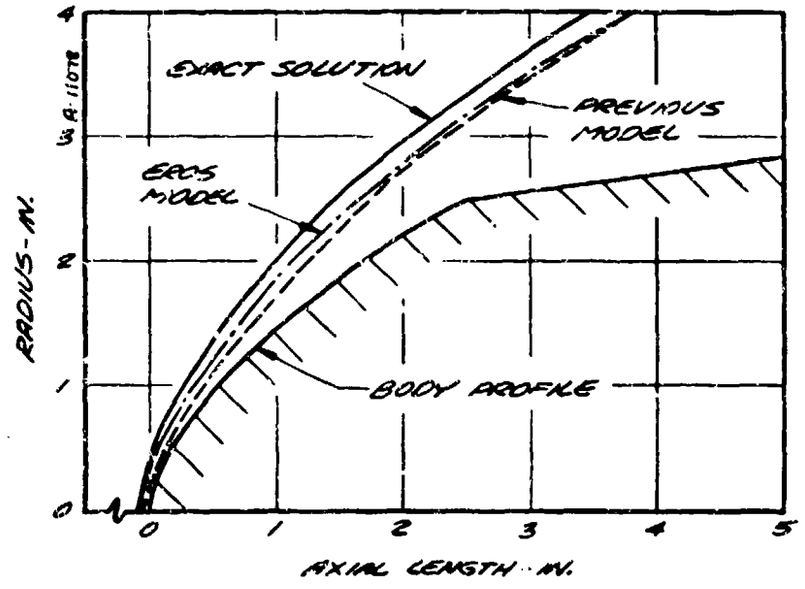

b) Mach 20

Figure 3-1. Shock shape comparisons for convex nosetip profile.

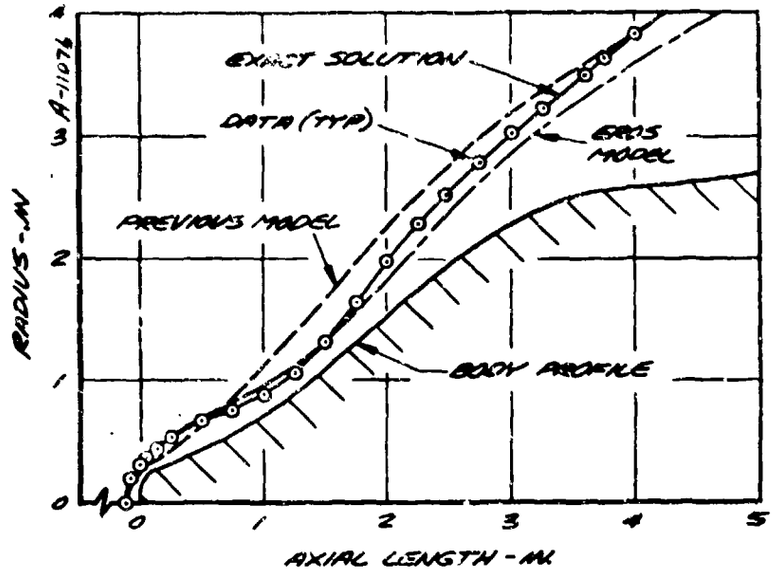

a) Mach 5

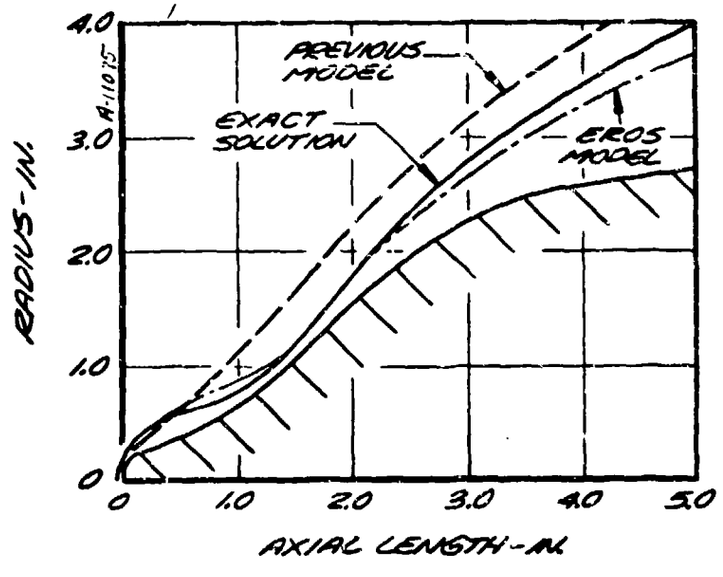

b) Mach 20

Figure 3-2. Shock shape comparisons for concave nosetip profile.

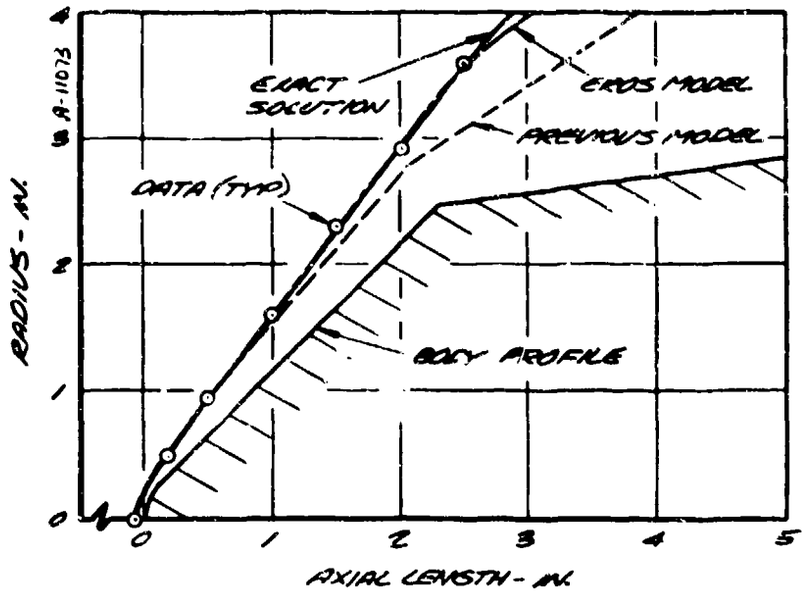

a) Mach 5

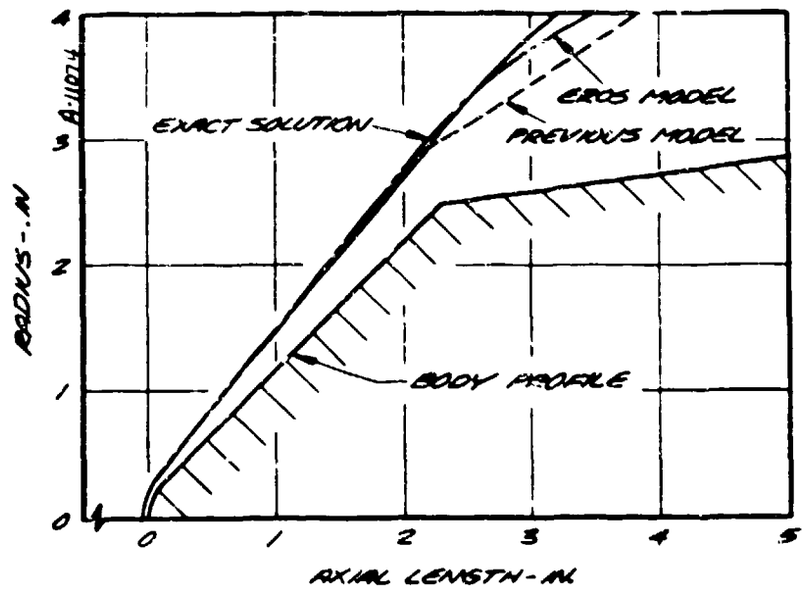

b) Mach 20

Figure 3-3. Shock shape comparisons for 45 degree conic nosetip profile.

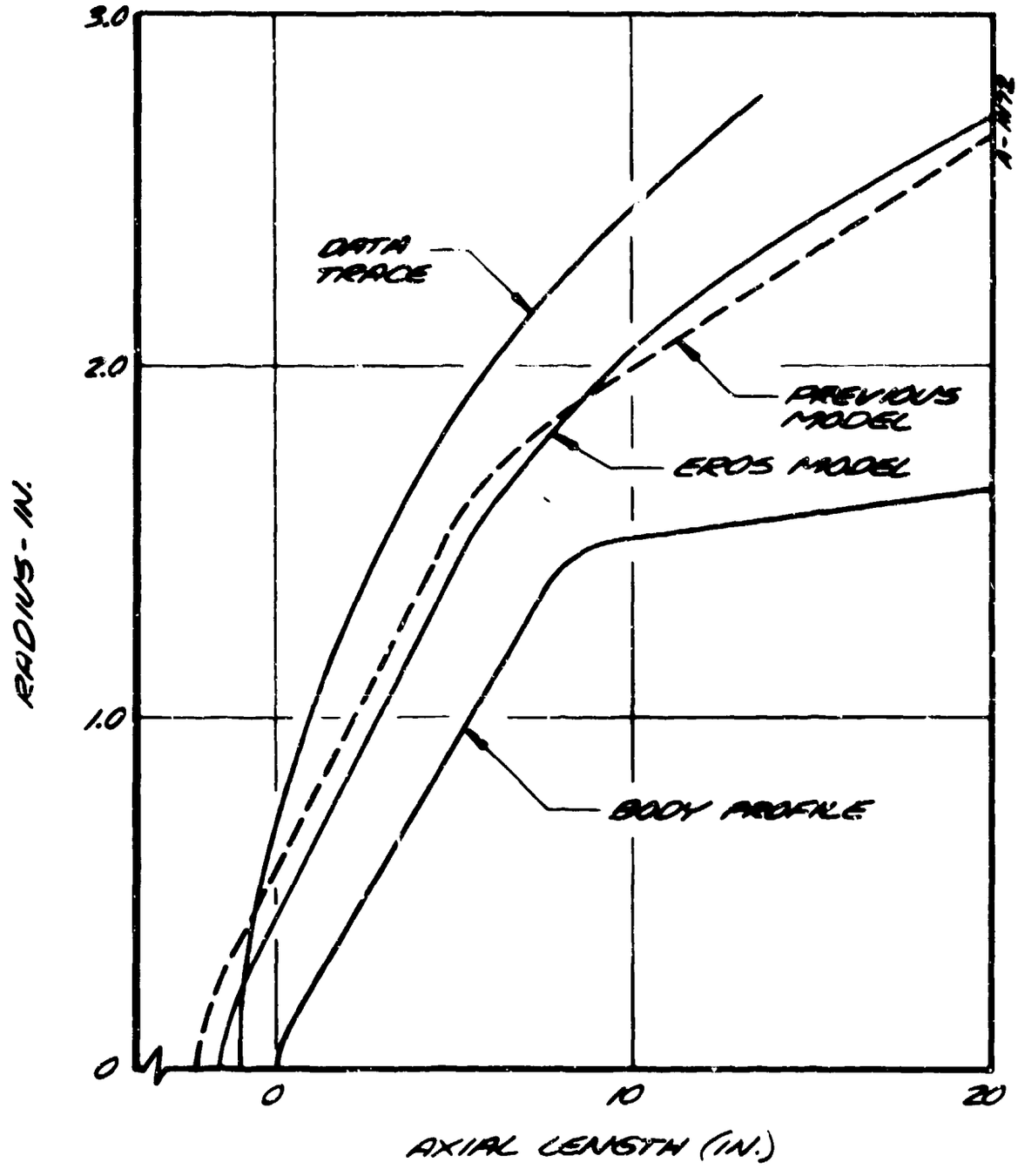

Figure 3-4. Shock shape comparisons for 60 degree conic nosetip profile.

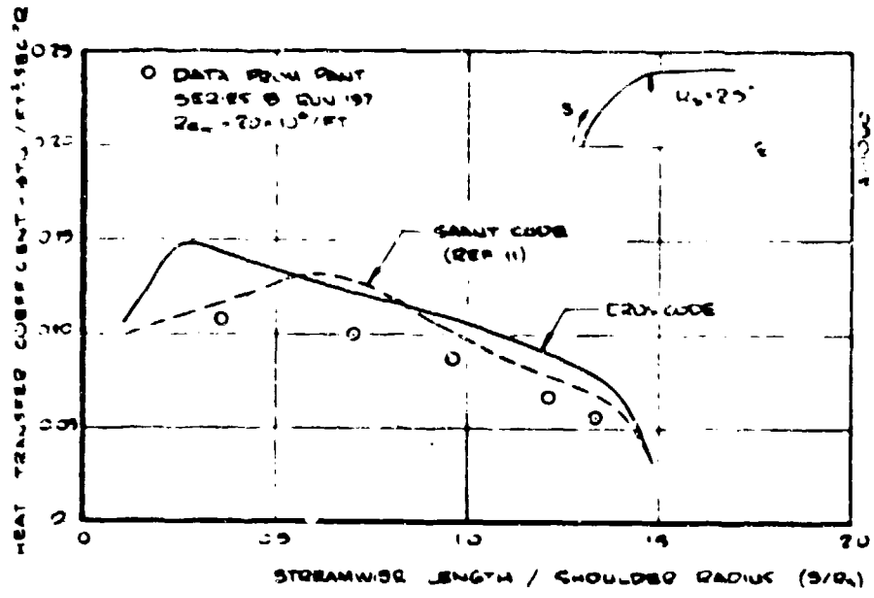

(a) Convex.

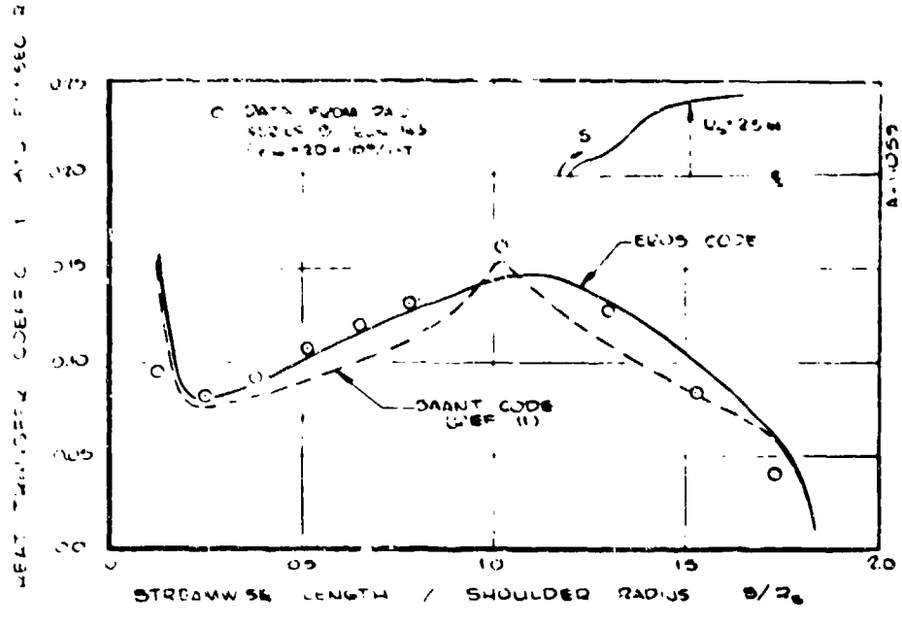

(b) Concave.

Figure 3-5. Smoothwall heat transfer distribution comparisons.

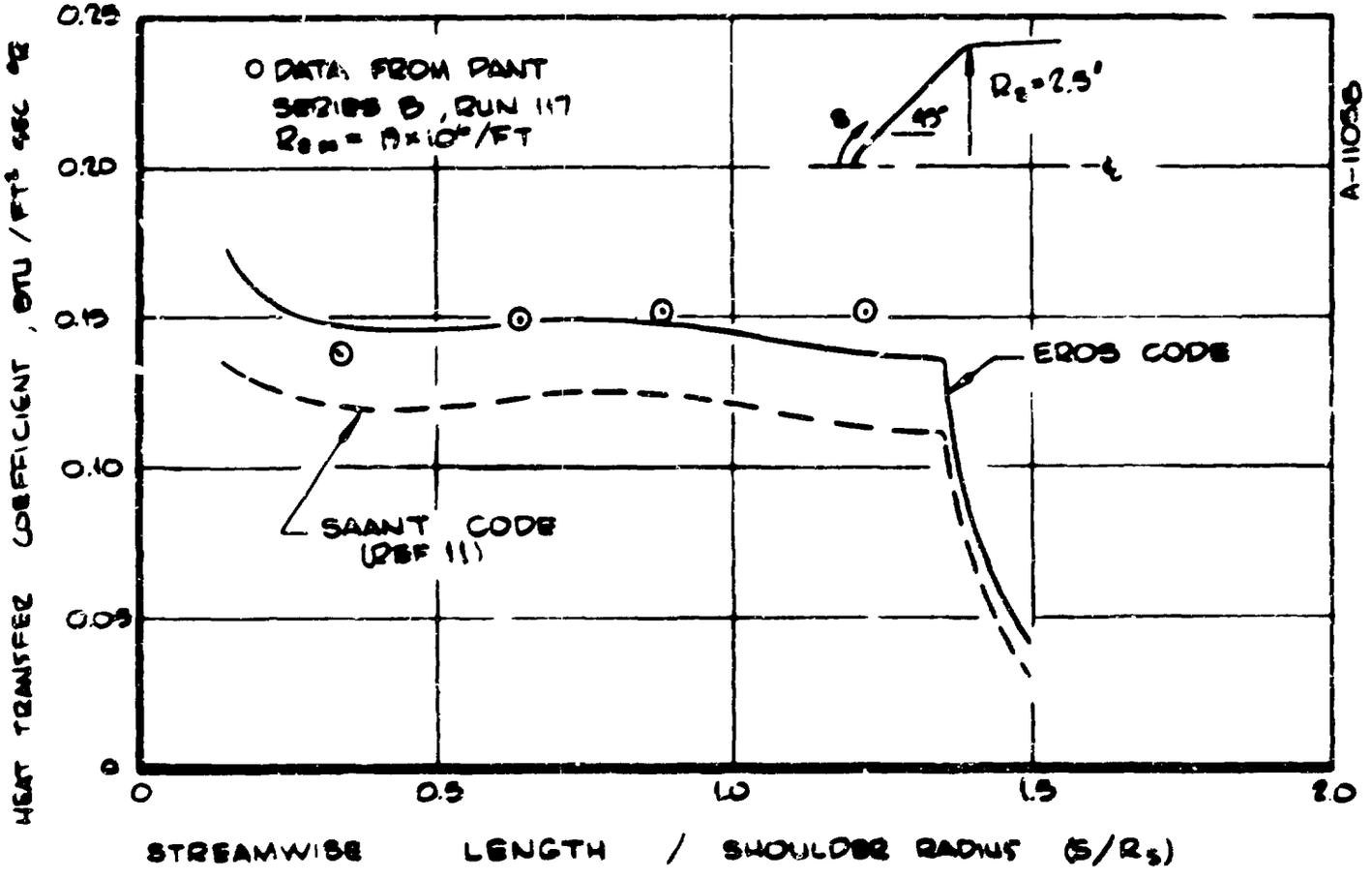

C.) 45 DEGREE CONIC

Figure 3-5. Concluded.

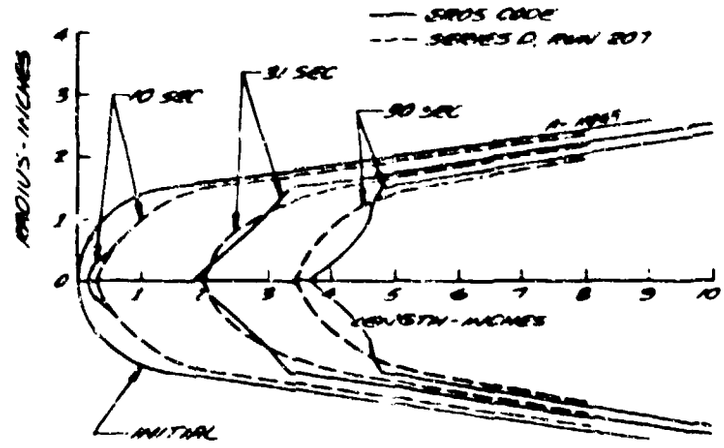

(a) Shape change.

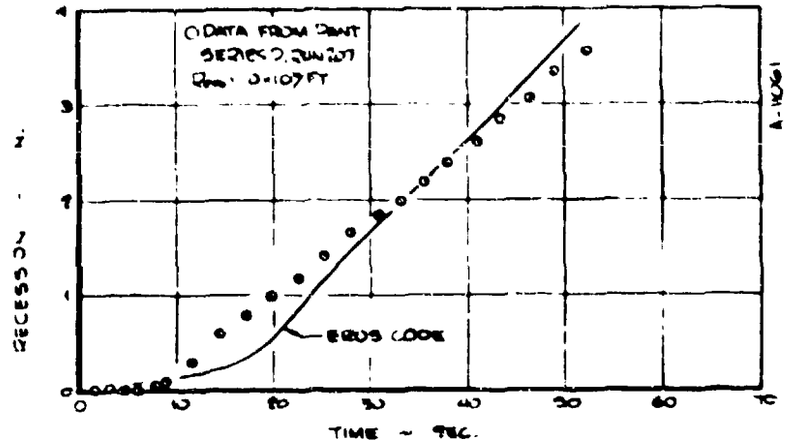

(b) Stagnation point recession.

Figure 3-6. Run 207 camphor shape change prediction (Re_∞ = 10 x 10^6/ft).

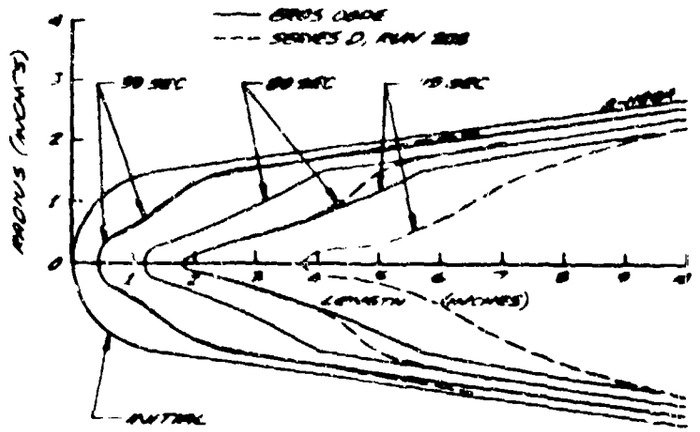

(a) Shape change.

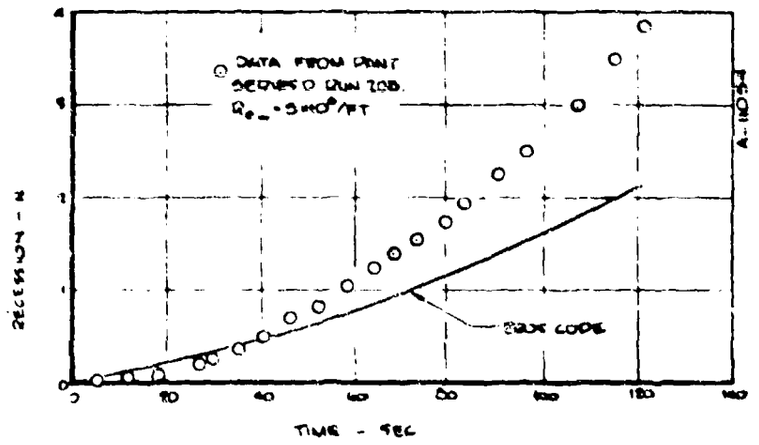

(b) Stagnation point recession

Figure 3-7. Run 208 camphor shape change prediction (Re_∞ = 5.23 x 10^6/ft).

207 and 208, respectively. When compared with the wind tunnel data, one observes that the predicted shape generally agrees with data. However, the solution for Run 208 underpredicts the stagnation point recession. This underprediction is attributed to the uncertainty in forecone macroroughness modeling.

3.2 REENTRY VEHICLE NOSETIP SOLUTIONS

The upgraded PANT computer code (EROS) was exercised for two high performance reentry situations. The objectives of the calculations were two fold:

- Exercise and "debug" erosion/ablation coupling logic for clear air solutions.
- Understand the sensitivity of clear air nosetip shape and recession predictions to uncertainties in and modifications to modeling techniques.

Trajectory parameters and nosetip configurations for these two cases are described in Section 3.2.1. In Section 3.2.2, the matrix of clear air response modeling variations are summarized. Results are discussed in Section 3.2.3.

3.2.1 Trajectory Parameters and Nosetip Configurations

Two typical trajectory and nosetip configuration cases were analyzed. Table 3-1 summarizes basic features of the cases. Trajectory properties (vehicle velocity and stagnation pressure) are plotted versus attitude and reentry time for the two cases in Figure 3-8. Initial configurations are shown in Figure 3-9.

TABLE 3-1. TRAJECTORY/CONFIGURATION PARAMETERS

	Case 1	Case 2
Entry Velocity, kft/sec	22.8	22.3
Entry Angle, Degree	-38	-26
Ballistic Coefficient, lb_f/ft^2	2150	3300
Nose Radius, in.	1.25	0.75
Cone Half Angle, Degree	6.7	6.3
Material Type	Fine Grain Graphite	Polycrystalline Graphite or Fine Weave Carbon/Carbon
Nosetip Design	Shell	Plug

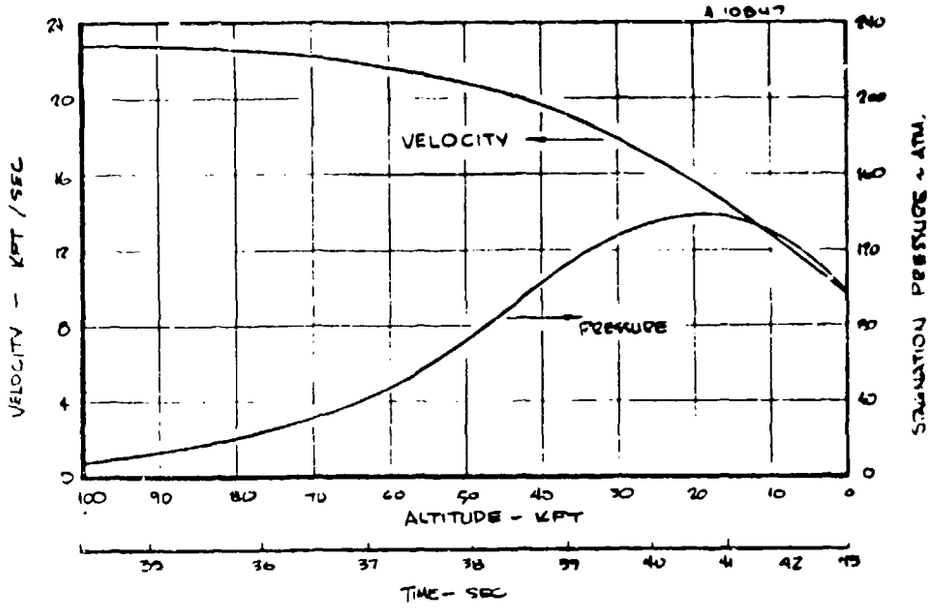

a) Case 1 (R_N = 1.25 in.)

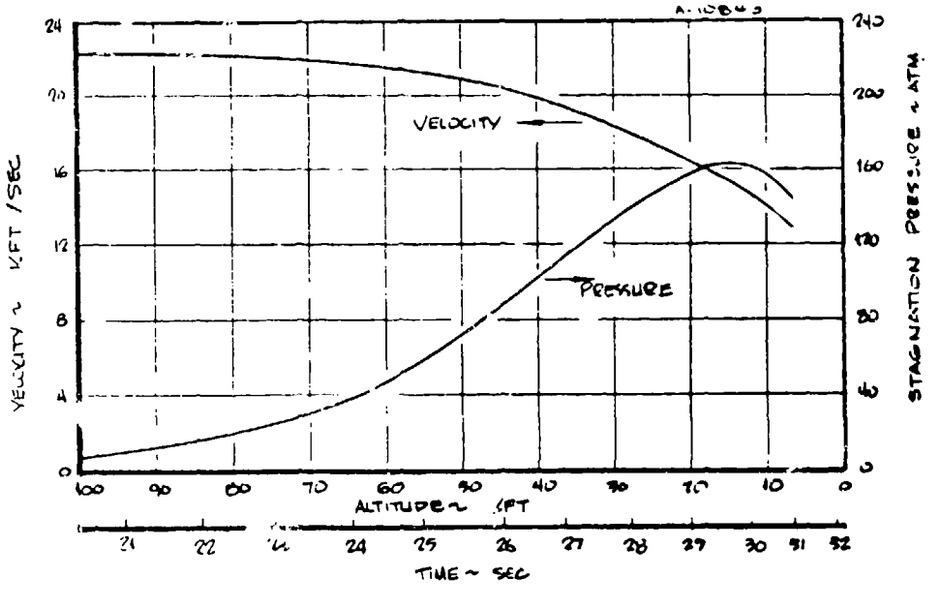

b) Case 2 (R_N = 0.75 in.)

Figure 3-8. Trajectory definition for clear air flight response sensitivity calculations.

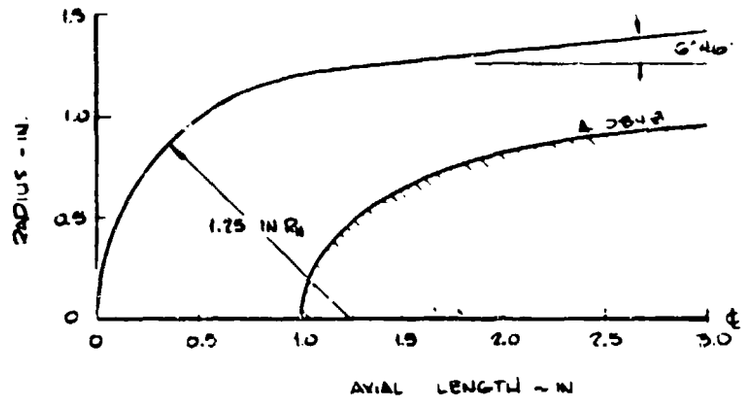

a) Case 1 (R_N = 1.25 in.)

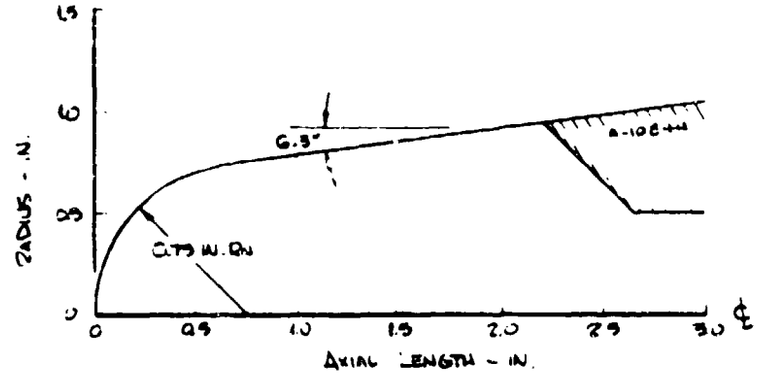

b) Case 2 (R_N = 0.75 in.)

Figure 3-9. Initial configurations for clear air flight response sensitivity calculations.

The two cases represent a significant variation in several parameters, yet within current conditions of interest to nosetip and reentry vehicle system designers. Both nosetip materials are basically graphitic with the primary distinction (from a shape change point of view) coming from the micro or intrinsic roughness used as the baseline for analysis sensitivity studies. The smaller nose radius, high ballistic coefficient case (Case 2) is representative of a higher recession situation than Case 1. Thus the two cases exercised the shape code differently.

3.2.2 Matrix of Ablation Modeling Parametric Solutions

For each trajectory-configuration case, baseline modeling and material property values were selected and a solution was generated. Systematic variations from the baseline were then defined and the cases were run for comparison. Variations in the following were considered:

- transition due to microroughness variations
- transition due to alternate transition criteria specifications
- turbulent heat transfer due to macroroughness (scallop) effects
- shock shape definition procedures

Table 3-2 summarizes the modeling assumptions used for the respective trajectory-configuration calculations. Shape profile histories for the fifteen solutions are shown in the Appendix. Suitable comparisons between respective solutions are presented in the following section.

3.2.3 Results of Parametric Solutions

Parametric calculations including variations in critical modeling provide an excellent basis to check out computer code logic and simultaneously to clarify the effects of modeling uncertainties on computations. In this section, several results from the parametric analysis matrix (Table 3-2) are compared and conclusions are summarized. For reference, the nominal baseline solutions for cases 1 and 2 are shown in Figure 3-10 and 3-11, respectively. The figures include both the shape profile history (shape profile at roughly 10 kft intervals) and the stagnation point recession history for the two cases. Both the shape and recession responses are significantly different.

Two solutions, in addition to the baseline runs, were performed for both cases 1 and 2 to assess the affect of material microroughness on the nosetip transition onset altitude and on the resulting stagnation point recession.

TABLE 3-2. MATRIX FOR ABLATION MODELING PARAMETRIC SOLUTIONS

Solution	Reentry Case	Transition Modeling		Macroroughness Modeling[b]	Shock Shape Modeling	Objective Relative to Baseline Assumptions
		Microroughness (mil)	Criterion[a]			
1	1 (R_N = 1.25 in)	0.27	$Re_k\ (S/\delta^*)^{1/3}$	$k_t = 0.93\ P_e^{-0.77}$	New (Ref 1)	Baseline for Case 1
2		0.20				Smaller microroughness
3		0.30				Larger microroughness
4		0.20		$k_t = 0.93\ P_{t2}^{-0.77}$		Smaller microroughness and macroroughness
5		0.27		$k_t = 0.93\ P_e^{-0.77}$	Old (Ref 11)	Change from old shock shape modeling
6	2 (R_N = 0.75 in)	0.40			New (Ref 1)	Baseline for Case 2
7		0.20				Smaller microroughness
8		0.60				Larger microroughness
9[c]		0.60	$Re_\theta\ (k/\psi\theta)^{0.7}$			Alternate transition criterion with larger microroughness
10		0.40	$Re_k\ (S/\delta^*)^{1/3}$			Transitional heating assumption
11		0.40	$Re_k\ (S/\delta^*)^{1/3}$	$k_t = 0.93\ P_{t2}^{-0.77}$		Smaller macroroughness
12[c]		0.40	$Re_\theta\ (k/\psi\theta)^{0.7}$	k_t = 1.0 mil		Alternate transition criterion plus lower macroroughness
13		0.40	$Re_k\ (S/\delta^*)^{1/3}$	$k_t = 0.93\ P_e^{-0.77}$	Old (Ref 11)	Change from old shock shape modeling

[a]Column identifies various PANT transition criteria described in Reference 5 and 11; "Sharp" means immediate transition with no transitional heating length allowed.

[b]Terminal scallop dimensions modeled as a function of either stagnation pressure (P_{t2}) or edge pressure (Pe); K_t used directly in PANT roughwall heating correlation (Reference 6).

[c]Solutions 9 and 12 performed using both transient and steady state conduction modeling.

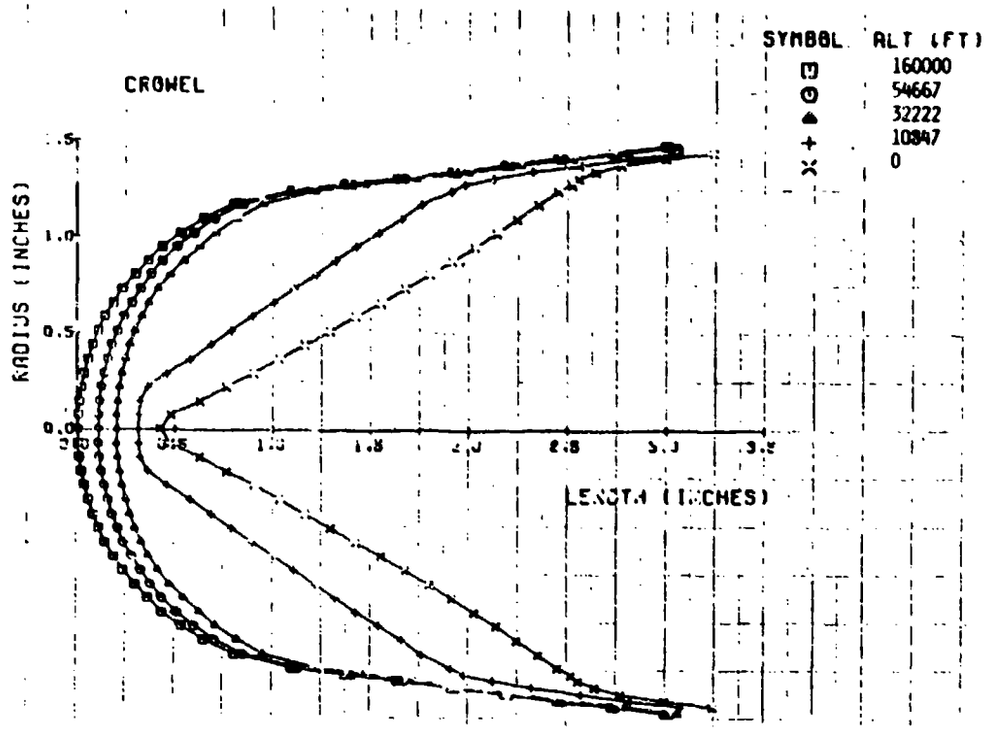

(a) Shape change

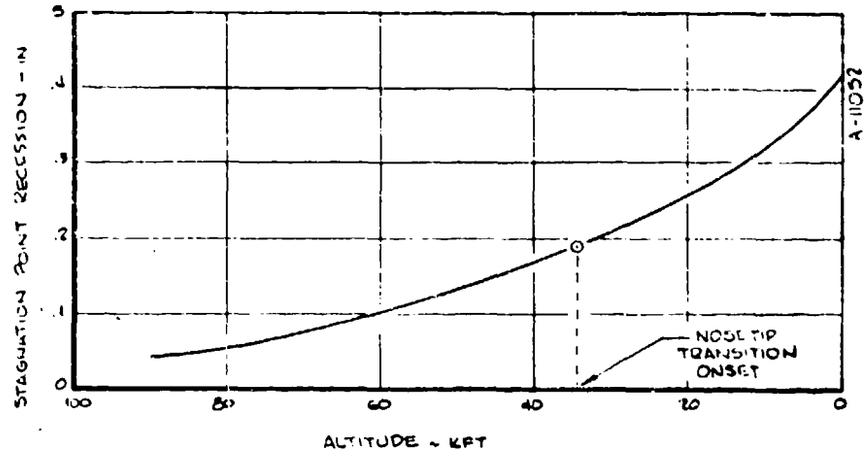

(b) Stagnation point recession

Figure 3-10. Nominal baseline prediction (Solution 1) for Case 1.

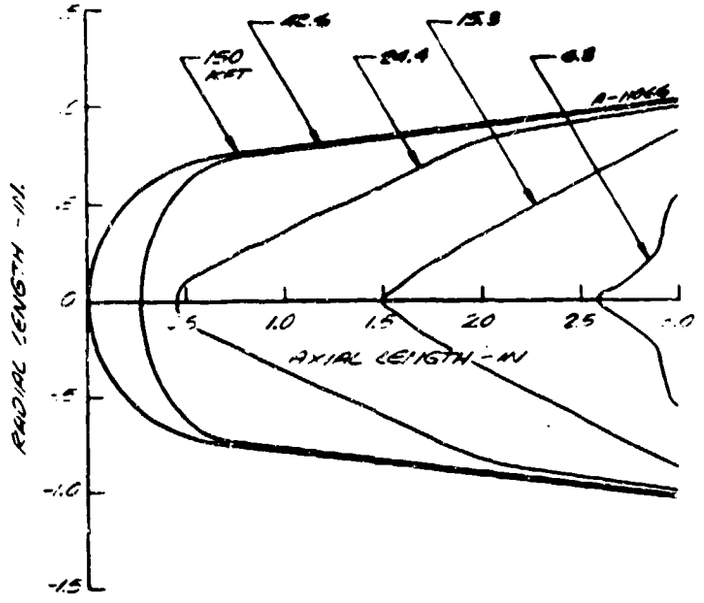

(a) Shape change.

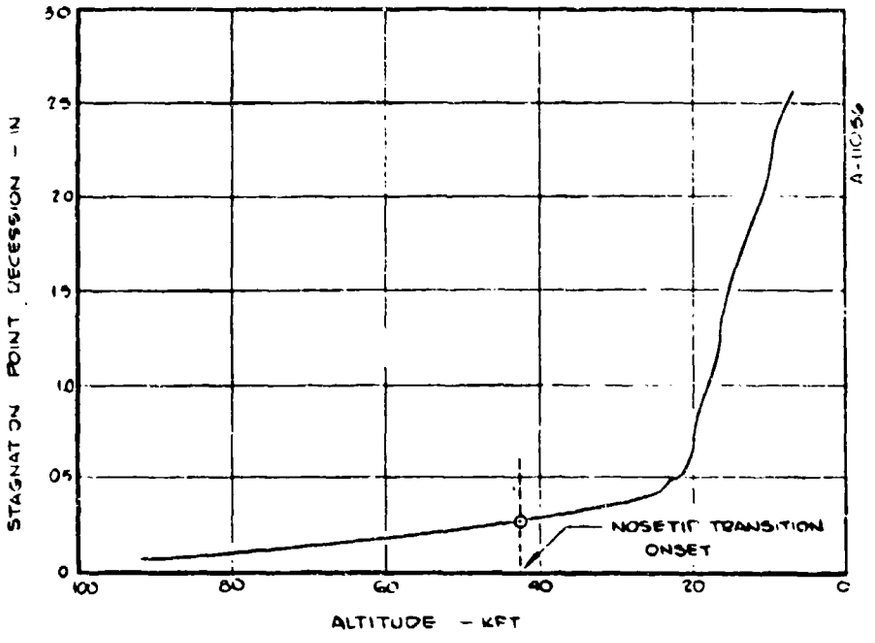

(b) Stagnation point recession.

Figure 3-11. Nominal baseline prediction (Solution 6) for Case 2.

Recession histories for these six predictions (Solutions 1, 2, 3, 6, 7, and 8 in Table 3-2) are compared in Figure 3-12. For each case, larger roughness means earlier transition and more total recession. Some amount of time is required between transition onset and the time when stagnation point recession is affected. During this period, the nosetip shape is changing from the blunt, laminar profile to a conic type shape. Once the sharpening process nears completion, the stagnation region radius of curvature decreases, and heating and recession rate increase. The earlier transition onset occurs, then the sooner the shape will become sharp. Figure 3-12b indicates the significant increase in recession rate once sharpening is complete.

Figures 3-13 and 3-14 further demonstrate the sensitivity of the clear air nosetip response prediction to the value of the material microroughness. Figure 3-13 gives nosetip transition onset altitude as a function of microroughness. Symbols indicate the results from the parametric solution matrix, including those solutions using the updated PANT transition criterion. The figure indicates the following:

- Transition onset altitude is very sensitive to microroughness;
- Essentially no difference exists between cases 1 and 2 (effects of nose radius and trajectory differences compensate);
- Use of the updated PANT transition criterion gives a slightly higher transition onset.

Figure 3-14 shows the sensitivity of overall stagnation point recession to the material microroughness value for cases 1 and 2. The estimated trends are based on the anticipated sharpening altitude and recession rate. An additional data point from Reference 13 has been added. Note the significant increase in recession that can occur for a small change in microroughness.

Once transition onset occurs, the turbulent boundary layer interacts with the ablation process to increase the surface roughness through the formation of crosshatches or scallops on the nosetip. Based on results from Reference 14, the effective scallop roughness (macroroughness) has been modeled as a function of edge pressure,

$$K_t = AP_e^{-0.77} \qquad (3\text{-}1)$$

where A has been defined for materials of interest by evaluating ablation data taken in the AFFDL 50 MW arc jet. A convenient means of varying the macroroughness within the uncertainty of the 50 MW data analysis is to use the stagnation pressure in place

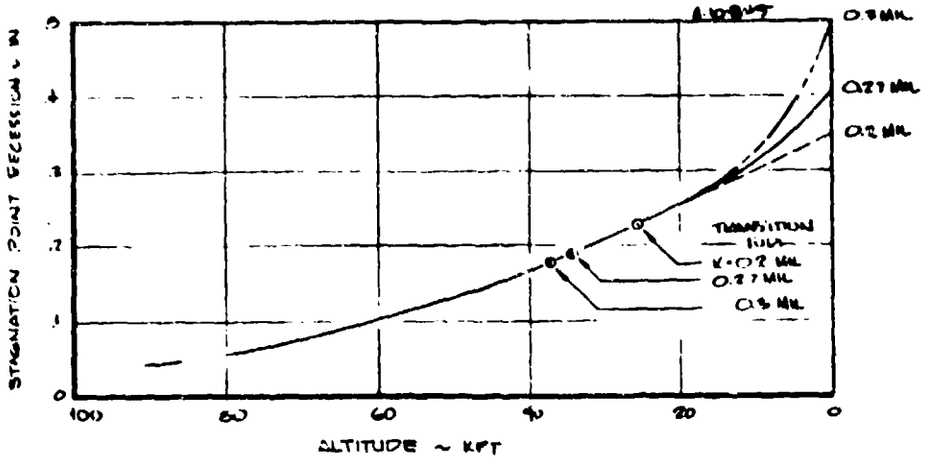

(a) Case 1.

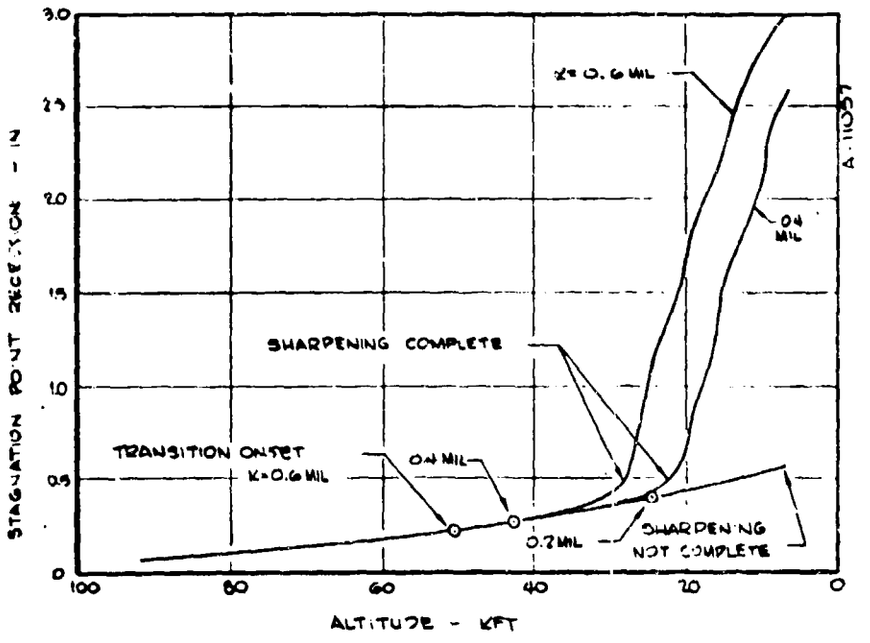

(b) Case 2.

Figure 3-12. Effect of microroughness on nosetip transition altitude and resulting stagnation point recession.

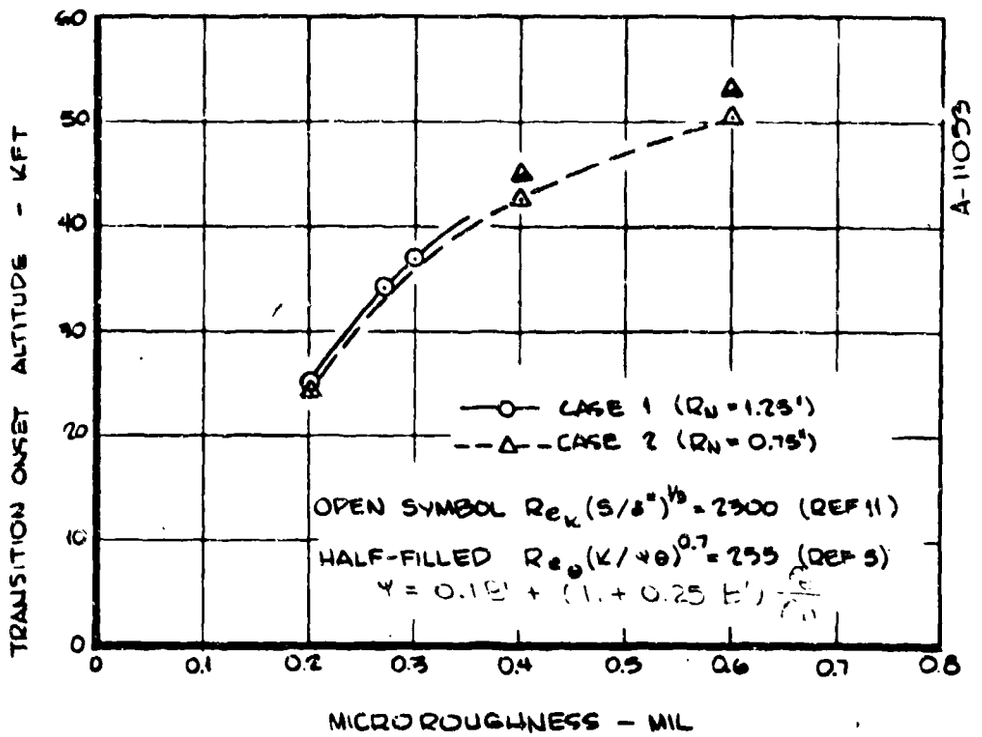

Figure 3-13. Nosetip transition onset sensitivity to microroughness.

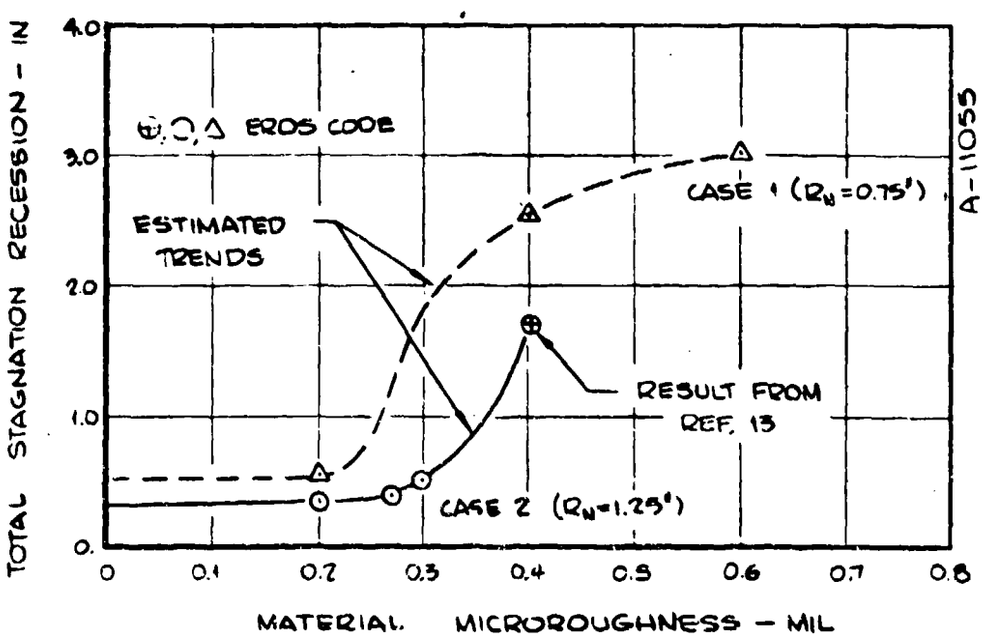

Figure 3-14. Total stagnation point recession sensitivity to microroughness.

of the edge pressure in the above correlation. This was done for solutions 4 and 11 of the parametric matrix (Table 3-2) as shown in Figure 3-15, this modeling change has the following effects:

- Sharpening time is longer because the turbulent forecone heating and recession rate are less;
- Recession rate after sharpening is roughly 12 percent lower when stagnation pressure is used (See Case 2, Figure 3-15b).

Nosetip response predictions comparing the SAANT shock model (Reference 11) and the revised shock model (Reference 1) demonstrated the effect of this modeling update. Figure 3-16 shows the final shape profile comparison for Case 1 and the recession history comparison for Case 2. For the large nose radius case, which experiences relatively little turbulent recession, the effect was negligible. For the small nose radius case, the new shock model produced slightly more stagnation point recession and a slightly higher angle turbulent-forecone shape. This trend agrees with the expected effects of the improved shock model since the principle modification came in the supersonic, ablated shape situations, not in the laminar or sharpening situations.

The importance of modeling transitional heating was assessed by a comparison between the baseline solution and a solution based on a "sharp" transition assumption (Solutions 6 and 10 in Table 3-2). Sharp transition means immediate increase to fully turbulent heating rate at the nosetip location where transition is predicted. Figure 3-17 shows the recession history comparisons for Case 2 (Rn = 0.75 in.). The primary effect of this modeling variation was a reduction in the time required for the nosetip to sharpen from the shape at transition onset to a fully turbulent shape where recession increases significantly. For the small nose radius analysis case, the net recession increased roughly 10 percent due to the higher sharpening altitude.

Two nosetip response predictions for the small nose radius case were obtained using the transient, 2-D heat conduction logic in the EROS code. Comparable steady state solutions indicated that modeling of transient, 2-D heat conduction was important but not critical to the evaluation of shape and recession trends. Two-dimensional heat conduction towards the nosetip centerline generally increases stagnation point recession and produces a slightly larger nose radius shape than predicted in steady state. A secondary effect of the stagnation region blunting can be a reduction in heat transfer and a net reduction in recession. These trends can be seen in the transient, steady state comparisons in Figure 3-18.

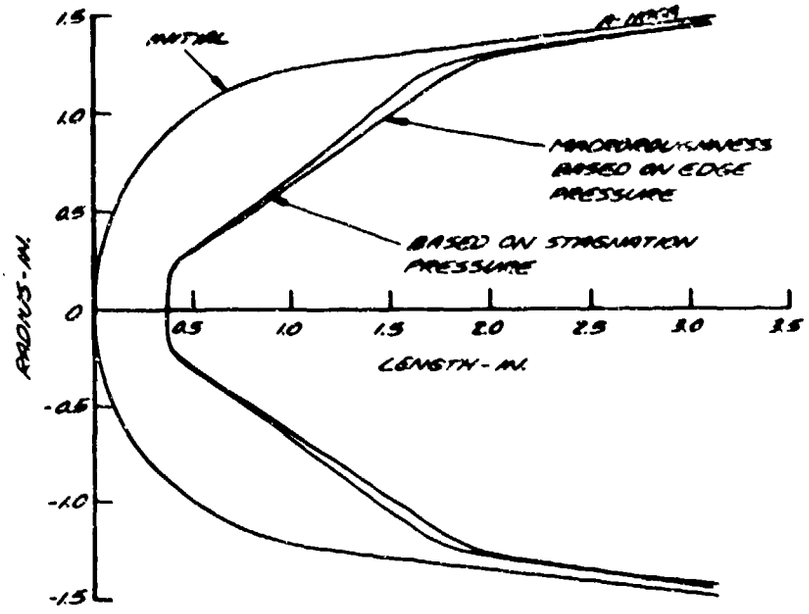

(a) Shape change (case 1).

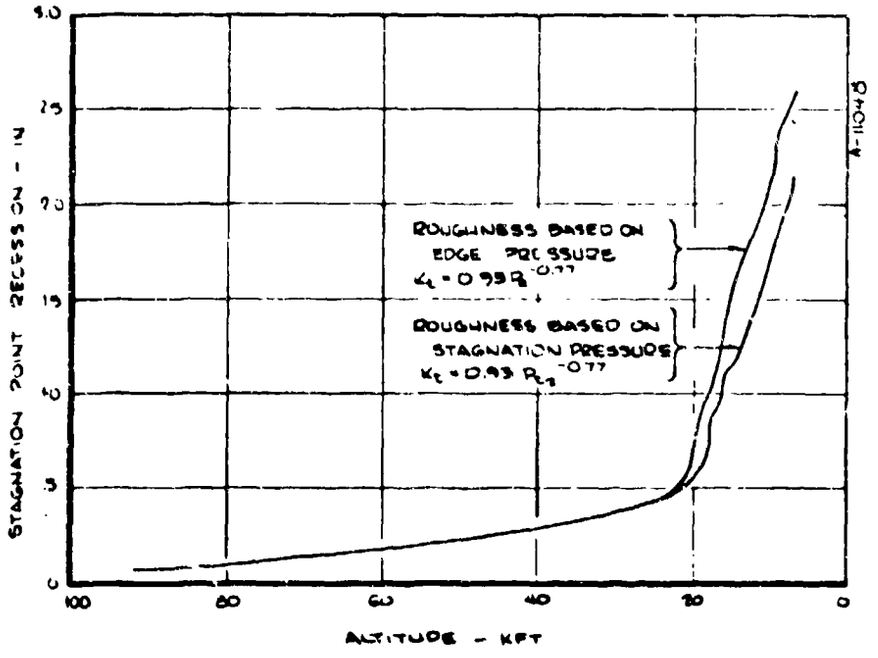

(b) Stagnation point recession (case 2).

Figure 3-15. Effect of macroroughness upon nosetip response prediction.

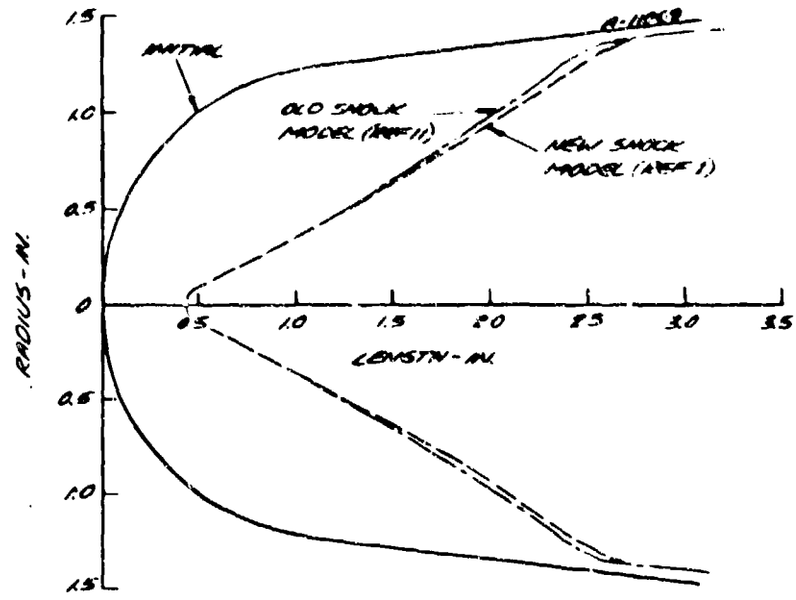

(a) Shape change (Case 1).

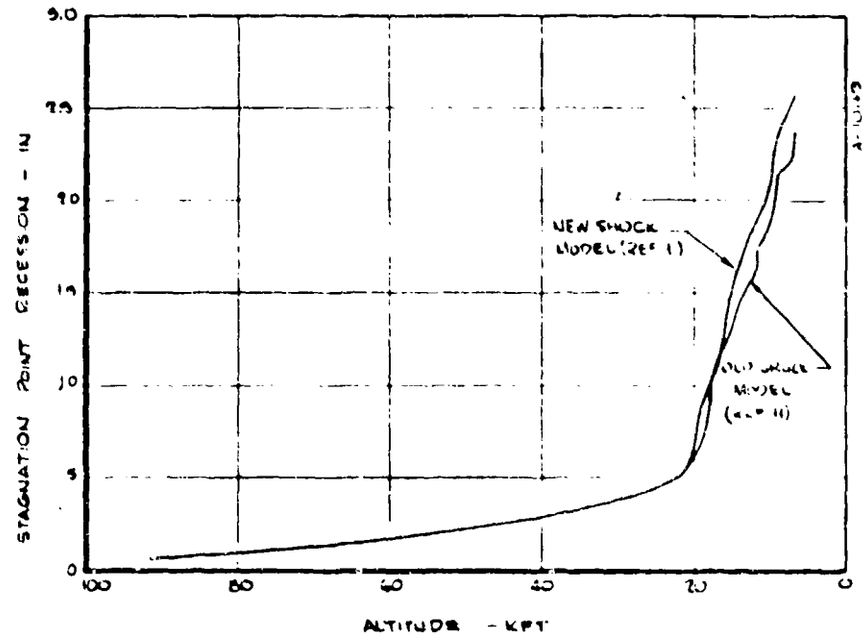

(b) Stagnation point recession (Case 2).

Figure 3-16. Effect of shock model upon nosetip response prediction.

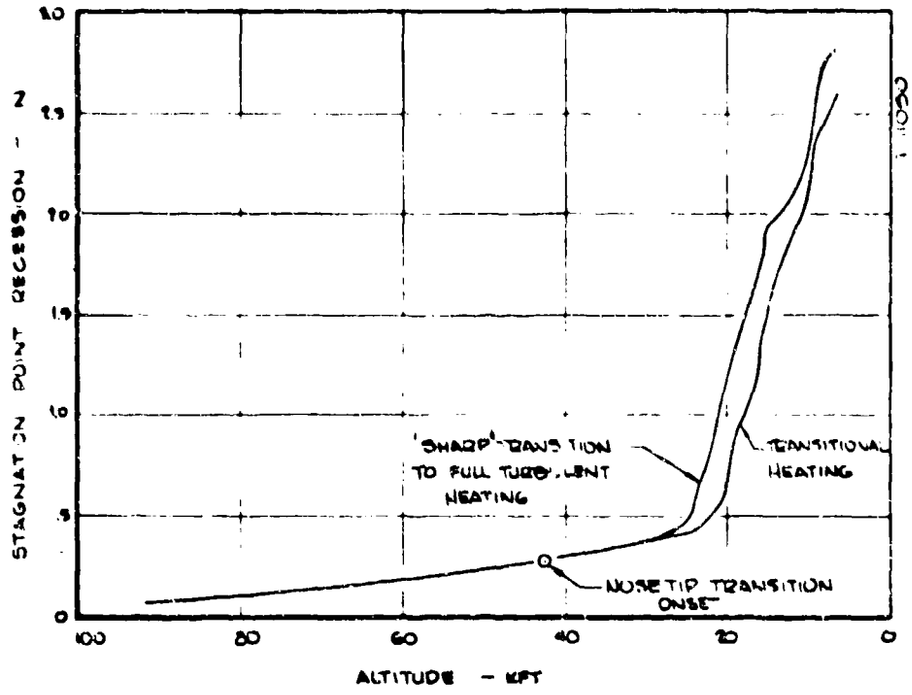

Figure 3-17. Effect of transitional heating model on Case 2 recession history.

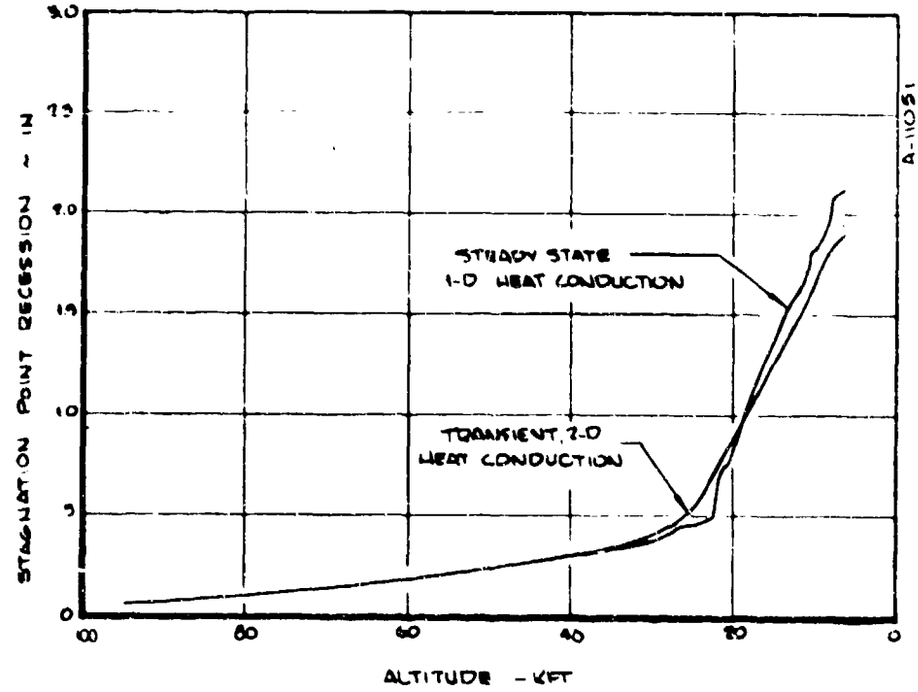

Figure 3-18. Effect of transient heat conduction on Case 2 recession history.

In summary, several aspects of modeling were addressed in the parametric code check out matrix. The solutions confirmed that the code was functioning properly in the recommended mode of operation. The solutions indicated that the most important code input is the material microroughness since this parameter controls transition onset attitude. The response predictions were generally less sensitive to other modeling changes and uncertainties.

SECTION 4

WEATHER EFFECTS SENSITIVITY SOLUTIONS

The EROsion shape (EROS) computer code combines the environmental and shape modeling techniques developed under the PANT program with weather effects modeling developed under the basic National Hazards Assessment Program and the preliminary studies under this effort (Reference 1). In this section, the results of the initial code solutions generated using the weather related modeling features are presented. These solutions were performed primarily to check out code logic. However, the resulting sensitivity study does provide a basis for identifying critical modeling assumptions.

Two sounding rocket test flights performed under the SAMSO sponsored SAMS/ Terrier-Recruit series were selected for analysis. These relatively low velocity flights of graphitic type nosetips provided weather, trajectory, and nosetip response data for code assessment purposes. Trajectory, configuration, and weather parameters for the two flights are presented in Section 4.1.

Each of the weather effects modeling features developed in this program and reported in Reference 1 was exercised in the check out matrix. These included:

- nominal and lower bound mass loss correlations for the flight material
- crater formation and/or crater healing effects on rough wall heat transfer
- erosion related heating augmentation
- particle slowdown and mass loss in the shock layer.
- particle stripping and breakup in the shock layer

The specific analysis matrix is presented in Section 4.2.

Comparisons of results to each other and to the nosetip response data are presented in Section 4.3.

4.1 FLIGHT TEST CONDITIONS

Two similar flight tests were analyzed using the EROS computer code. The tests were conducted from Wallops Station, Wallops Island, Virginia in February and March of 1972. The flights were performed by Sandia Corporation under joint sponsorship of Sandia and SAMSO. The booster for each flight was the SAMS/Terrier-Recruit which achieved peak velocities of roughly 8600 ft/sec. A recovery package enabled retrieval of the nosetip payload. The flights are designated Sandia Test No. R341412 and R341413 or, more typically, SAMS 6 and SAMS 7. Trajectory, configuration, and nosetip response data are given in Reference 15. Weather data were obtained from Reference 16. Key flight test parameters are summarized in Table 4-1. Pertinent trajectory quantities are shown in Figure 4-1; the initial configuration for both tests in shown in Figure 4-2, and the weather parameters (liquid water content and median particle diameter) used in the computer analyses are shown in Figure 4-3.

TABLE 4-1. SAMS FLIGHT TEST PARAMETERS

	SAMS 6	SAMS 7
Peak Velocity, ft/sec	8602	8575
Peak Stag. Press., atm.	58	57
Nose Radius, in.	0.625	0.625
Cone Angle, degrees	9.0	9.0
WSI, km^2-gm/m^3	7.5	2.9

4.2 EROSION MODELING SENSITIVITY MATRIX

For each flight case the matrix of EROS code solutions shown in Table 4-2 were generated. The various models are discussed in detail in Reference 1 and summarized below

Mass Loss Correlations

The nominal mass loss correlation used for the EROS code solutions was derived from single impact and ballistic range erosion data. The form of the correlation is

$$G_{nom} \propto V^{1.8} \sin^{0.62}\theta$$

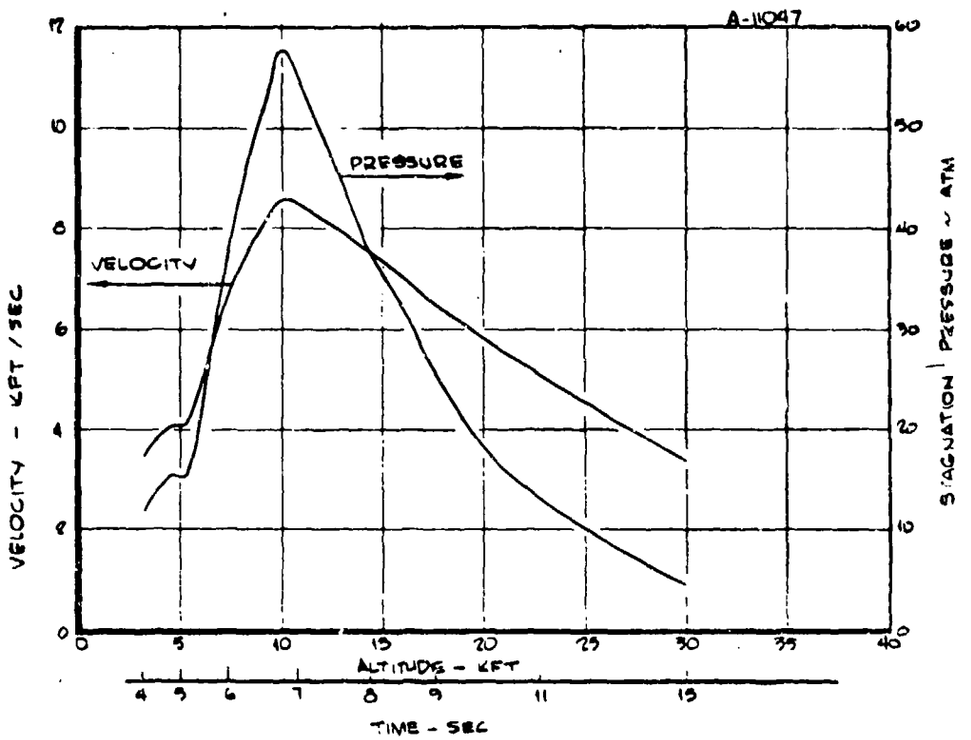

(a) SAMS 6.

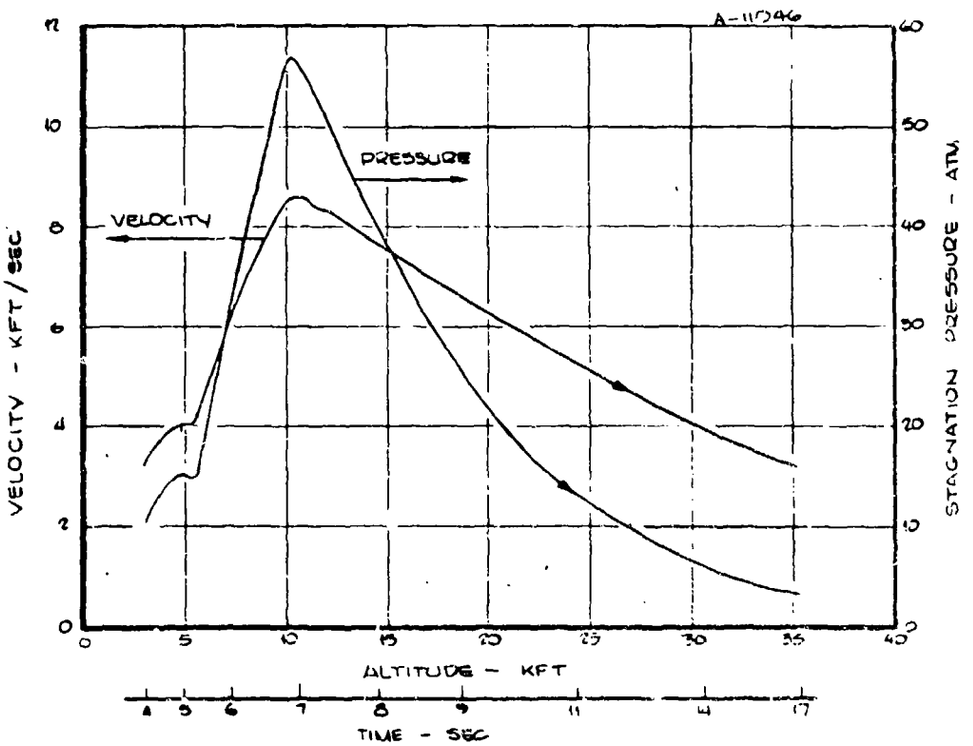

(b) SAMS 7.

Figure 4-1. Trajectory parameters.

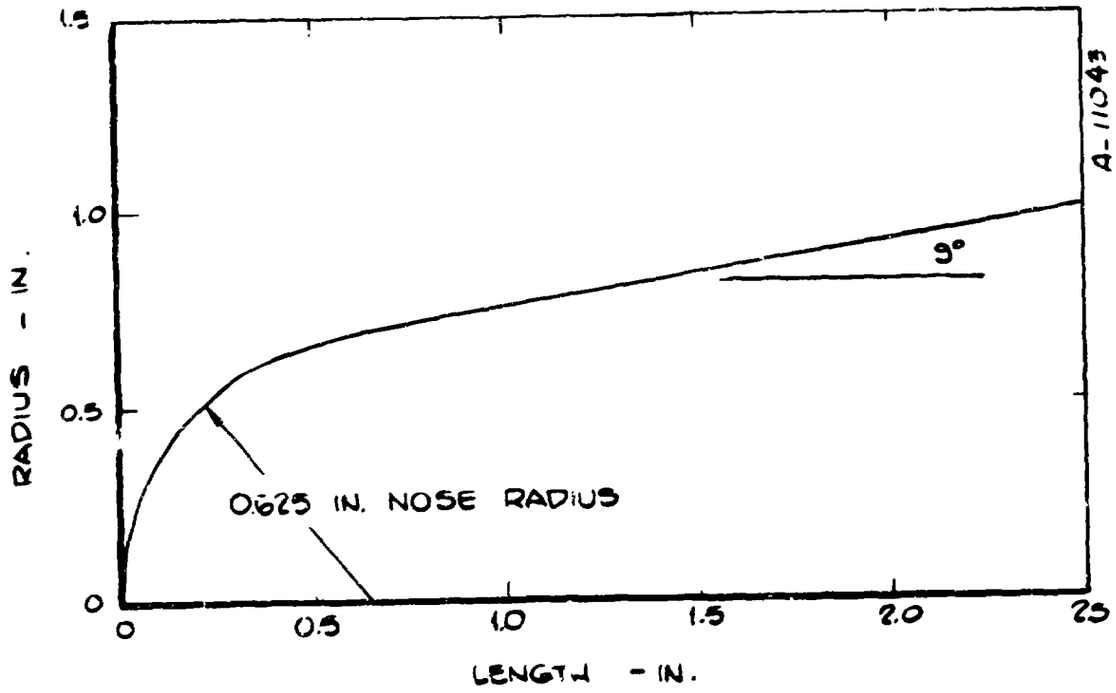

Figure 4-2. Initial nosetip profile for erosion modeling sensitivity study.

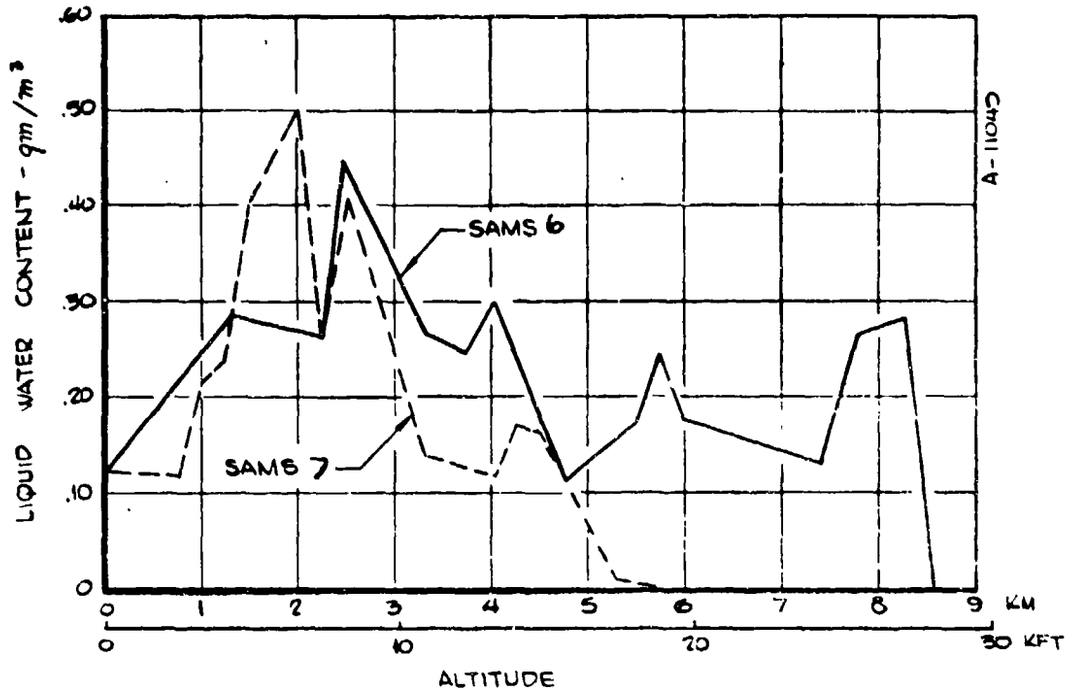

(a) Equivalent liquid water content distributions.

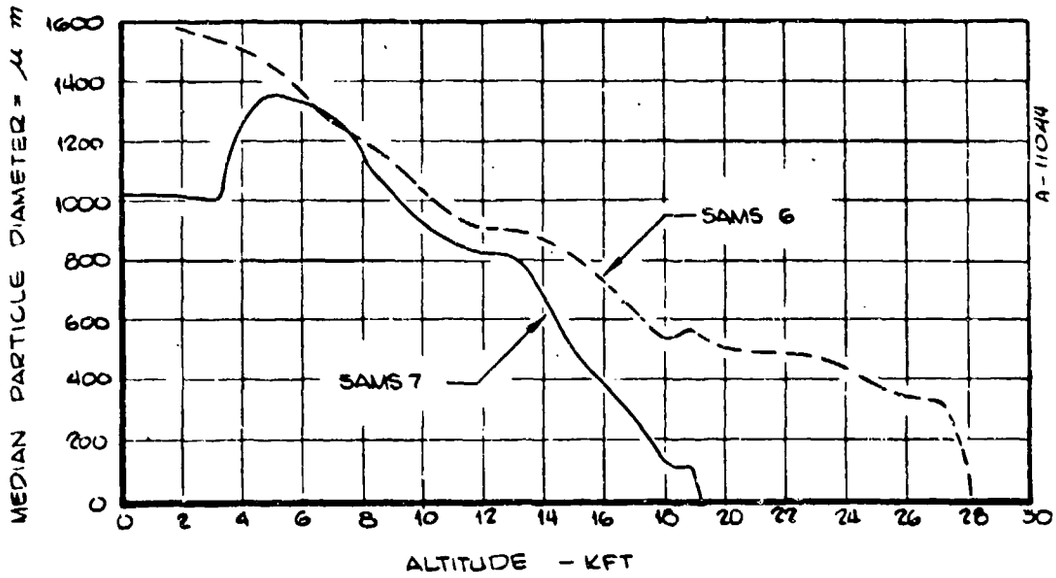

(b) Median particle diameter.

Figure 4-3. Weather parameters for erosion sensitivity studies.

TABLE 4-2. EROSION MODELING SENSITIVITY MATRIX

Solution*	Mass Loss Correlation	Crater Roughness Heating	Erosion Augmentation	Particle Slowdown/Ablation	Particle Breakup	Solution Objective
1	None	No	No	No	No	Clear Air Reference
2	Nominal	Yes	Yes	No	No	Baseline Solution
3	Lower	Yes	Yes	No	No	Minimum G Law
4	Nominal	No	Yes	No	No	No Crater Effects
5	Nominal	Crater Healing	Yes	No	No	Ablation Healing of Crater
6	Nominal	Yes	No	No	No	No Erosion Augmentation
7	Nominal	No	No	No	No	Uncoupled (No Crater or Erosion Heating Effects)
8	Nominal	Yes	Yes	Yes	No	Slowdown Model
9	Nominal	Yes	Yes	Slowdown Only	Yes	Particle Breakup

*Matrix of runs for both SAMS 6 and SAMS 7 analysis.

where

G_{nom} = ratio of ejected mass to incident mass

V = incident particle velocity at the surface

Θ = incident impact angle

This "G-Law" relation is given as Equation 3-9 of Reference 1.

A second mass loss correlation used to assess the sensitivity to mass loss was defined as the lower bound of the erosion data. The ratios of the lower mass loss correlation to the nominal is:

$$\frac{G_{low}}{G_{nom}} = 4.44\ V^{-0.2}$$

These two correlations give the same mass loss at V = 1734 ft/sec but the lower correlation gives roughly 30 percent less mass loss at the Terrier-Recruit peak velocity condition (8600 ft/sec).

Crater Roughness Heating

The modeling of crater effects on surface heat transfer includes two parts:

- evaluation of equivalent peak-to-valley sandgrain roughness dimension
- application of the PANT roughwall heat transfer modeling.

The application of the PANT roughwall correlation is described in Reference 11. The crater roughness is evaluated from the erosion mass loss and an assumed crater configuration assumption. For a hemispherical crater, the crater roughness, r_c, (Equation 3-16 of Reference 1) is:

$$r_c = \left(\frac{G\rho_p}{4\rho_t} \right)^{1/3} d_p$$

where

G is the mass loss ratio

ρ_p is the particle density

ρ_t is the surface material density

d_p is the incident particle diameter

The solutions which include the crater effects used the larg[illegible] of either the crater roughness, the intrinsic microroughness in laminar flow (0.4 mils), or the scallop macroroughness is turbulent flow. Scallop dimensions were found from

$$k = 0.93\ p_e^{-0.77}$$

For one matrix point, the effects of crater healing were modeled. Healing refers to the reduction of crater roughness between impacts due to ablation from the top of the crater. The healing model is formulated such that the average roughness dimension between successive impacts is used for heat transfer calculations. For example if the time between successive impacts (obscuration time, t_{obs}) equals the time to ablate away the crater dimension (t_{des}), then the average crater roughness is:

$$k = r_c/2 \qquad t_{obs} = t_{des}$$

Also for $t_{obs} < t_{des}$

$$k = r_c - \frac{\dot{s}t_{obs}}{2} \qquad t_{obs} < t_{des}$$

For $t_{obs} > t_{des}$

$$k = r_c^2/2\dot{s}t_{obs} \qquad t_{obs} > t_{des}$$

where $\dot{s}$ is the [illegible]ace r[illegible]ion rate from the top of the crater.

Erosion Augmentation

In the erosive environment, the presence of hydrometeors and surface erosion ejecta augment the heat tr[illegible]r to the nosetip. The physical mechanisms for this heating increase are not [illegible] defined, but the effect has been correlated by the following expression (Reference 17):

$$\dot{q} = \rho_\infty u_\infty (H_o - H_w) C_{H,u}$$

where $\dot{q}$ is incident laminar heat flux

$H_o - H_w$ is the total to wall enthalpy potential

$\rho_\infty u_\infty$ is the freestream air mass flux

$C_{H,u}$ is the erosion augmentation Stanton number, given by:

$$C_{H,u} = 0.098\ X^{0.317} \sin^2\theta$$

θ = local body angle

$$\chi = \rho_p V_p (1+G)/\rho_\infty u_\infty$$

$\rho_p V_p$ = particle freestream mass flux

G = mass loss ratio

This correlation is applied in parallel with the crater roughness heating modeling, for the laminar and transitional regions of the nosetip. That is, the larger of the two, usually the erosion augmentation, is used in the ablation calculation.

Particle Slowdown/Ablation

As the hydrometeor traverses the bow shock layer, it is exposed to relatively high temperature, dense air. Under these conditions water, ice, and snow particles slowdown and lose mass to the air. The model developed originally in Reference 18 and improved slightly in Reference 1 accounts for the particle slowdown and mass loss but does not consider particle deflection in the shock layer.

Particle Stripping and/or Breakup

As liquid rain drops traverse the shock layer, data indicate that mechanisms exist to cause surface layers of the drop to be stipped off, thus reducing the effective particle mass. Furthermore at certain conditions the drops can breakup catastrophically. Modeling described in Reference 19 was incorporated in the EROS code to study these phenomena, however, the residence time comes from the slowdown/ablation calculation. In the EROS code stripping breakup model, Bond number,

Bo*, is assumed to be in the range where stripping and/or breakup will occur (Bo > 10). As such, a critical normalized time, $\bar{T}_c^{\dagger}$ is defined from the Weber number, W^{+}, as follows:

$$\bar{T}_c = 45\ W^{-0.25}$$

For $\bar{T} > \bar{T}_c$, breakup occurs and no mass hits the surface. For $\bar{T} < \bar{T}_c$, no breakup occurs but stripping may be important. In the stripping model, the mass of the raindrop is given by:

$$\frac{M}{M_0} = \frac{1}{2}\left(1 + \cos \pi \frac{\bar{T}}{3.5}\right)$$

where

M = impact raindrop mass

M_0 = initial raindrop mass

Note that for $\bar{T} > 3.5$ all mass is stripped off and the effective impact mass is zero.

For the one sensitivity solution which exercised this model, the procedure was applied to all hydrometeor types (water, snow and ice). Furthermore, only the median particle size was considered. The effects of particle size distribution in either the slowdown/ablation or the stripping/breakup calculations were not addressed during these code checkout calculations.

---

* $Bo = g\ \rho_p r_o^{\,2}/\sigma$

Where g = particle acceleration
ρ_p = particle density
r_o = particle initial radius
σ = particle surface tension

† $\bar{T} = t u_2/D_o(\rho_2/\rho_p)^{1/2}$

Where t = resident time in shock layer
u_2 = gas velocity behind shock, relative to particle
ρ_2 = gas density behind shock
D_o = initial particle diameter

+ $W = 2\ \rho_2 u_2^{\,2} r_o/\sigma$

4.3 RESULTS OF EROSION EFFECTS SOLUTIONS

Results from the solution matrix (Table 4-2) are compared in this section to evaluate the sensitivity of nosetip response to erosion modeling variations; these evaluations are presented in the form of stagnation point recession comparisons. In addition, flight data are presented as an indication of the overall modeling accuracy. The ablation modeling for graphitic materials, summarized in Section 3, was used in the erosion effects computations. The erosion modeling is described in Reference 1 and Section 4.2. The effects of respective modeling features are discussed in the the following paragraphs.

Baseline Calculations

Baseline calculations for the two SAMS flights reveal that the coupling between erosion and ablation is significant. Figure 4-4 shows the relative contributions to the total recession. Using the baseline modeling, only 50 to 60 percent of the recession is directly due to erosive mass loss. The ablation component (40 to 50 percent of the total) results primarily from heat transfer increases associated with the hydrometeor encounter. Clear air heat transfer and ablation produces very little nosetip recession in these Terrier-Recruit flight tests (less than 0.1 in.). The comparison with data shows that the baseline modeling gives generally too much recession, 35 percent high for SAMS 6, 16 percent high for SAMS 7. This level of differences and the differences between the computed and measured recession histories are well within cloud profile uncertainties. The solutions described below provide insight into erosion related modeling which significantly affect the calculated recession and which may also explain the differences between prediction and data.

Minimum Erosion Mass Loss Correlation

The effects of uncertainties in erosion mass loss data were assessed by using an alternate mass loss correlation. Since the baseline solutions were above the flight data, a lower bound interpretation of the mass loss data given in Reference 1 was used. As described in Section 4.2,

$$\frac{G_{low}}{G_{nom}} = 4.44\ V^{-0.2}$$

where V is the velocity of the impacting mass. The solutions for the two SAMS flights are compared to the respective baseline computations in Figure 4-5. The results are a 20 percent reduction in stagnation point recession for SAMS 6 and 22 percent reduction for SAMS 7.

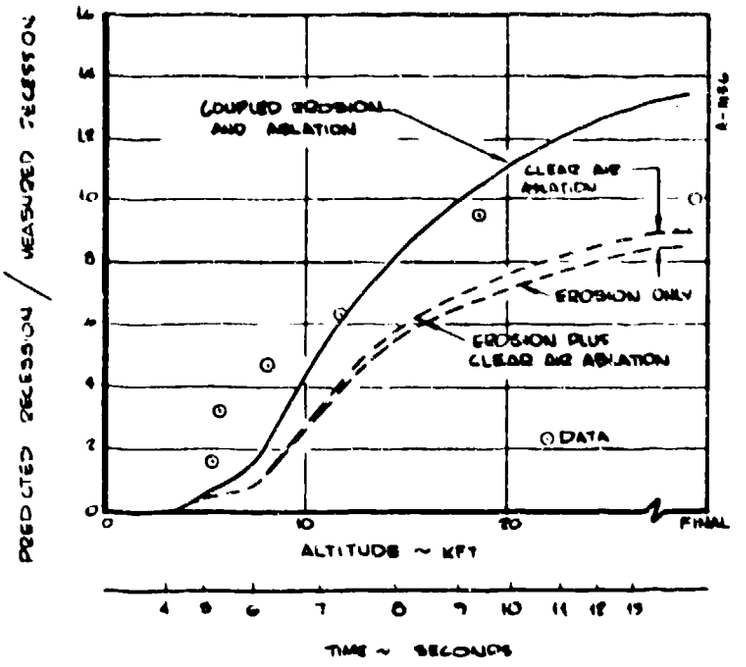

(a) SAMS 6

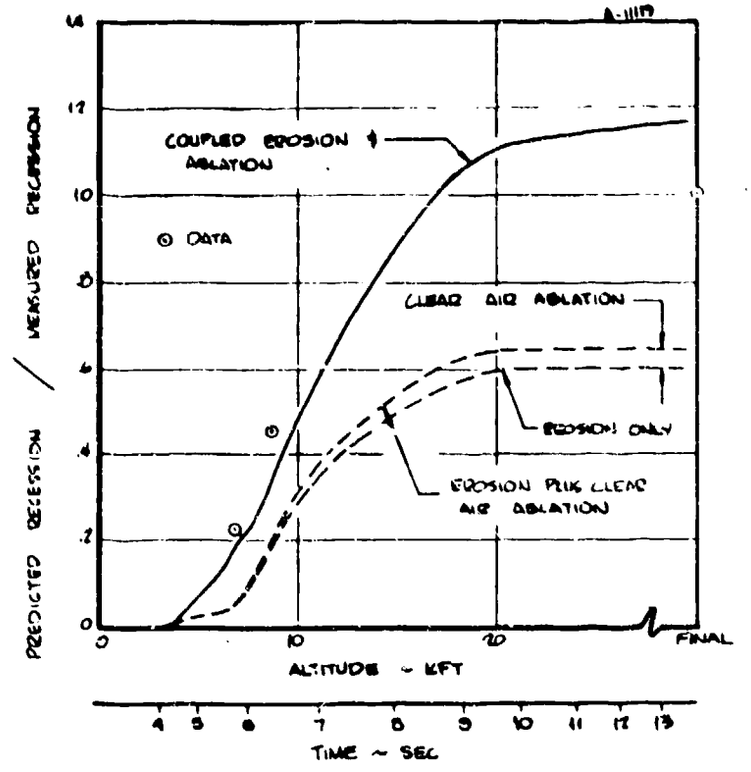

(b) SAMS 7

Figure 4-4. Baseline erosion/ablation calculations.

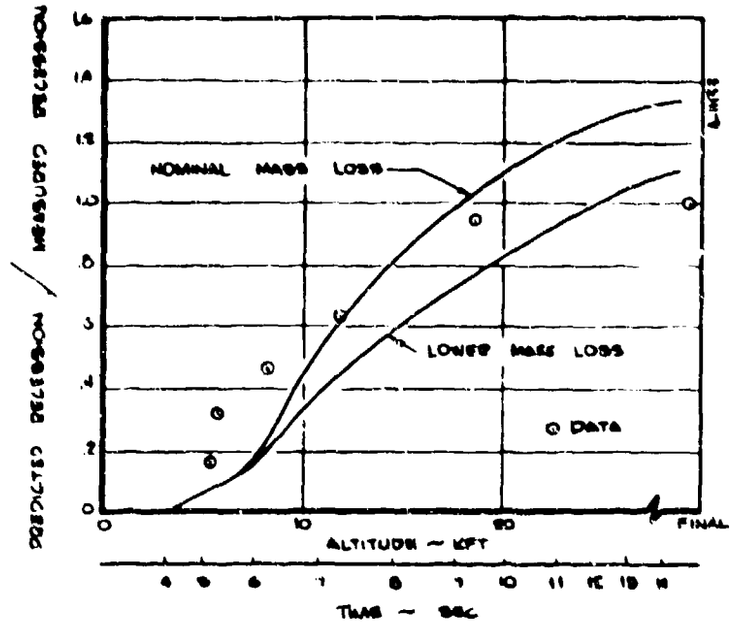

(a) SAMS 6

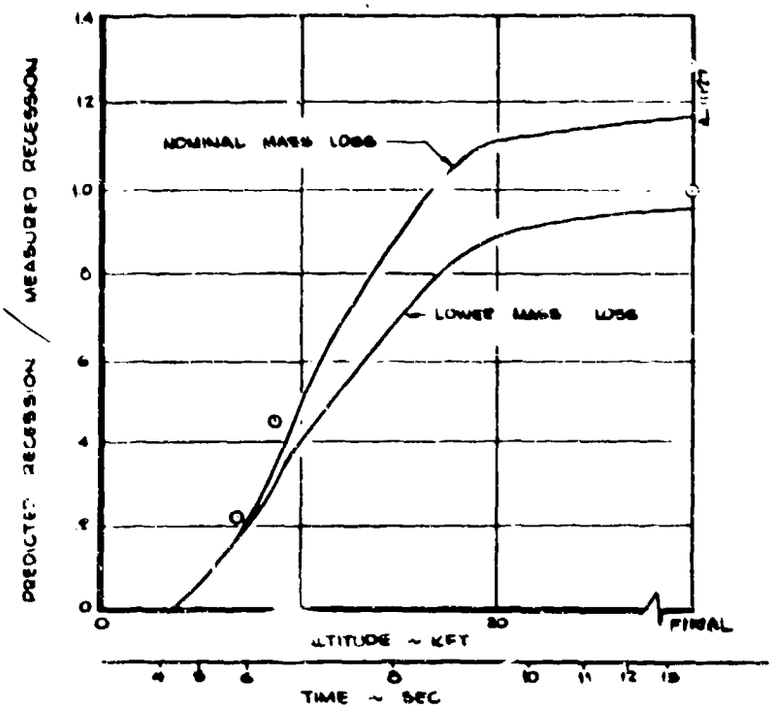

(b) SAMS 7

Figure 4-5. Erosion/ablation calculations using lower mass loss correlation.

For the velocity conditions typical of the Terrier-Recruit trajectory (6 to 8.6 kft/sec), the lower "G"-law gives between 23 and 27 percent reduction in mass loss ratio (G). Hence, the erosion component of recession is reduced directly by these amounts. The ablation component is also reduced because both crater roughness and erosion heating augmentation are dependent on the mass loss ratio. The overall 20 to 22 percent reduction in computed stagnation point recession consists of:

- Up to 14 percent from reduced erosion mass loss
- About 7 percent from reduced erosion effects on heat transfer and ablation

These reduction do provide better agreement with the final recession measurements. However, recession histories do not agree as well.

Erosion Effects on Heat and Mass Transfer

The baseline erosion modeling accounts for the effects of erosion augmentation and crater roughness on surface heat and mass transfer. In the EROS code, the modeling of these phenomena compete with the clear air models to determine the heat transfer boundary condition. The relative importance of cratering effects and erosion augmentation during the two SAMS flights was assessed through a series of EROS code calculations (Solutions 4 through 7 of Table 4-2). The following discussions compare the results.

- Solution 4 shows the effect of complete crater healing (i.e., no crater formation) on the computed recession
- Solution 5 was run to compute the amount of crater roughness reduction given by the ablation healing model derived in Reference 1.
- Solution 6 indicates the effect of eliminating the erosion augmentation model.
- Solution 7 allows only clear air heat transfer modeling by eliminating both crater effects on heat transfer and erosion augmentation. Thus, the solution could be considered uncoupled (no erosion/ablation coupling).

The Solution 5 calculations indicate that ablation healing does not significantly reduce crater roughness for the ablation rates and obscuration times typical of graphitic nosetips in a Terrier-Recruit flight. The maximum reduction in roughness was roughly 10 percent. Since roughness heating factors are correlated in terms of the logarithm of roughness (Reference 1), the 10 percent reduction has a negligible effect on the roughwall heat transfer. Computed recessions for SAMS 6 and SAMS 7 agreed closely with the baseline results.

When crater roughness is eliminated entirely, as in Solution 4, clear air scallop roughness dominates the turbulent heating computation, and erosion augmentation dominates the laminar and transitional distributions. As demonstrated in Figure 4-6, however, elimination of crater roughness has a minimal effect on the computed recession history. Slight differences late in the flights are associated with shape change effects. Similar results are achieved when crater roughness is allowed but augmentation is eliminated (Solution 6). Comparative recession histories are shown in Figure 4-7. In this case, craters promote transition very close to the stagnation region and dominate the roughness effects on laminar, transitional, and turbulent heat and mass transfer. Since the crater and erosion augmentation effects are modeled to act in parallel, it is concluded that they have a nearly equal magnitude for these flight conditions.

Figure 4-8 demonstrates that elimination of both cratering and erosion augmentation (Solution 7 of the sensitivity matrix) substantially reduces the overall computed recession. The recession in this case is roughly comparable to the erosion plus clear air ablation line shown in Figure 4-4. Erosion/ablation coupling is, therefore, a result of either surface cratering or erosion augmentation.

Figure 4-9 compares the stagnation point heat transfer coefficient histories for four SAMS 7 calculations. The curves demonstrate the significant heat transfer increase when either erosion augmentation or crater roughness are included in the solution. Furthermore, since the no crater solution is identical to the baseline case, it may be concluded that, for the Terrier-Recruit environment, the erosion augmentation controls the response when both effects are being considered.

Particle/Shock Layer Interactions

Two particle/shock layer interaction models are included in the EROS computer code. Solutions 8 and 9 of the sensitivity matrix indicate the effects of these models on the SAMS 6 and SAMS 7 computations. The particle slowdown/ablation model significantly reduces stagnation point recession, as shown in Figure 4-10. The primary cause is the ablation mass loss of the particle. Very little slowdown occurred. Indeed, for the aft cone region of the nosetip, the path length (shock to body) is sufficient to allow complete particle demise.

Calculations were also performed using the particle stripping and breakup model. This model applies only to raindrop encounters. Although the two flights were conducted in weather containing predominantly ice particles, the modeling was exercised for the full trajectory range. The median particle size as a function of altitude was used in the calculation. In all cases, the modeling had a negligible effect on the particle mass. Thus, the solutions were identical to the baseline results. This is reasonable considering the particle size assumptions.

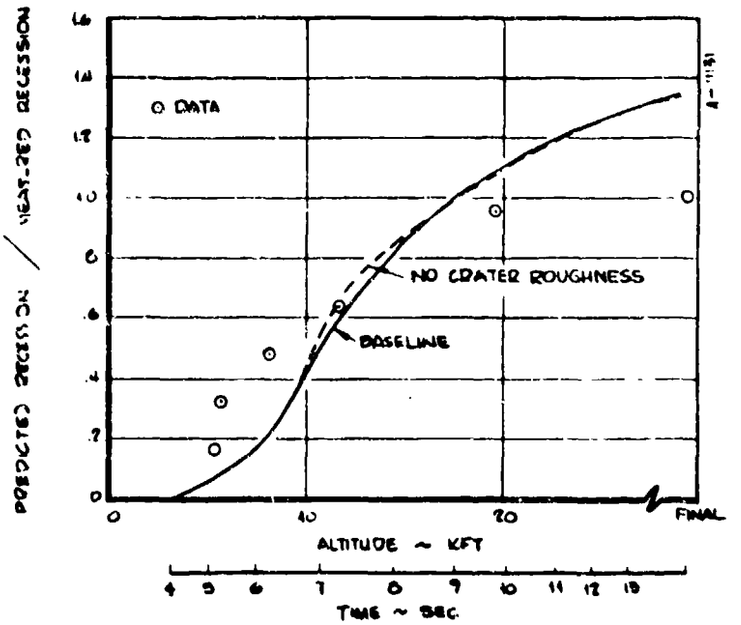

(a) SAMS 6

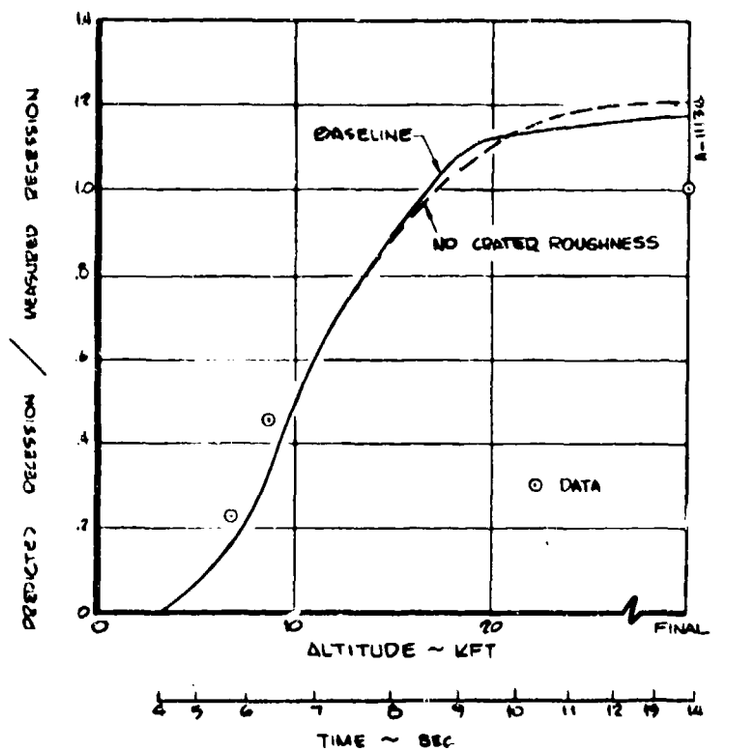

(b) SAMS 7

Figure 4-6. Erosion/ablation calculations allowing no crater roughness.

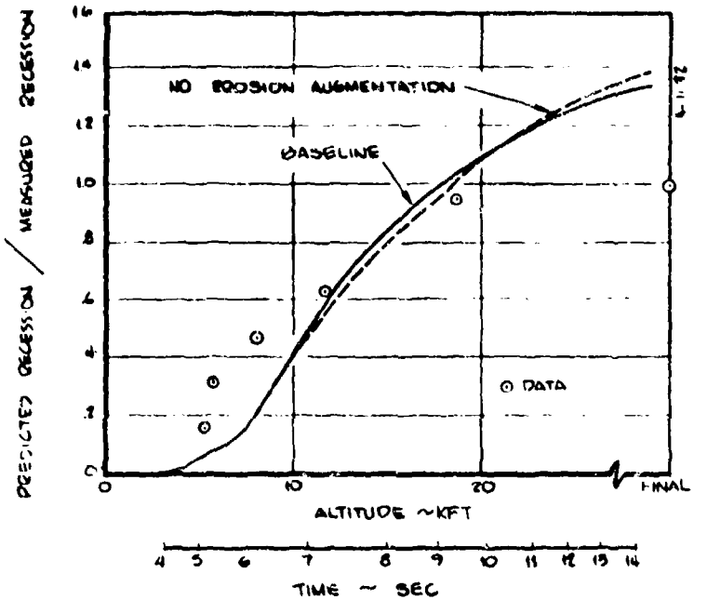

(a) SAMS 6

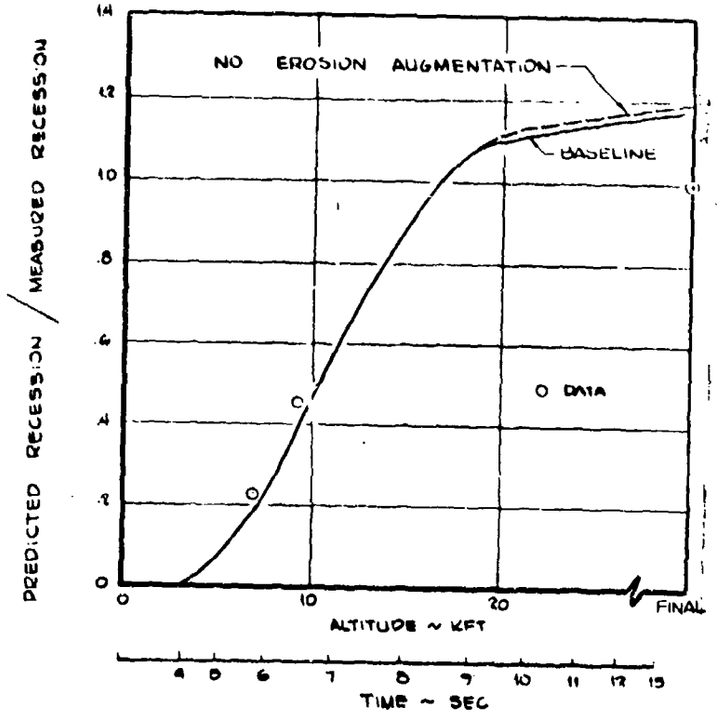

(b) SAMS 7

Figure 4-7. Erosion/ablation calculations allowing no erosion augmentation.

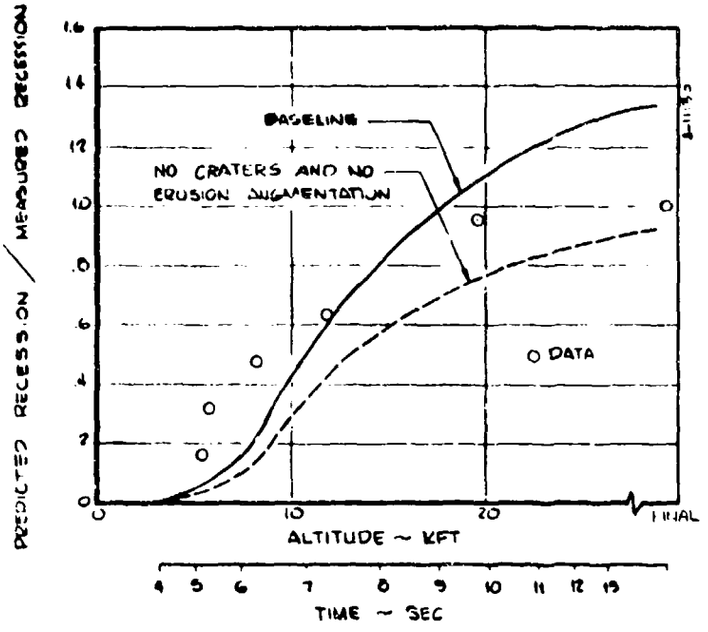

(a) SAMS 6

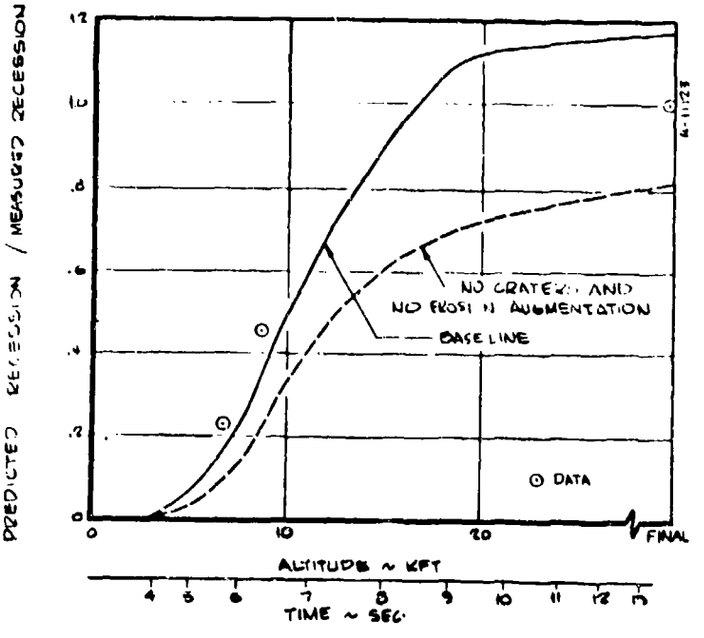

(b) SAMS 7

Figure 4-8. Erosion/ablation calculations allowing no crater roughness and no erosion augmentation.

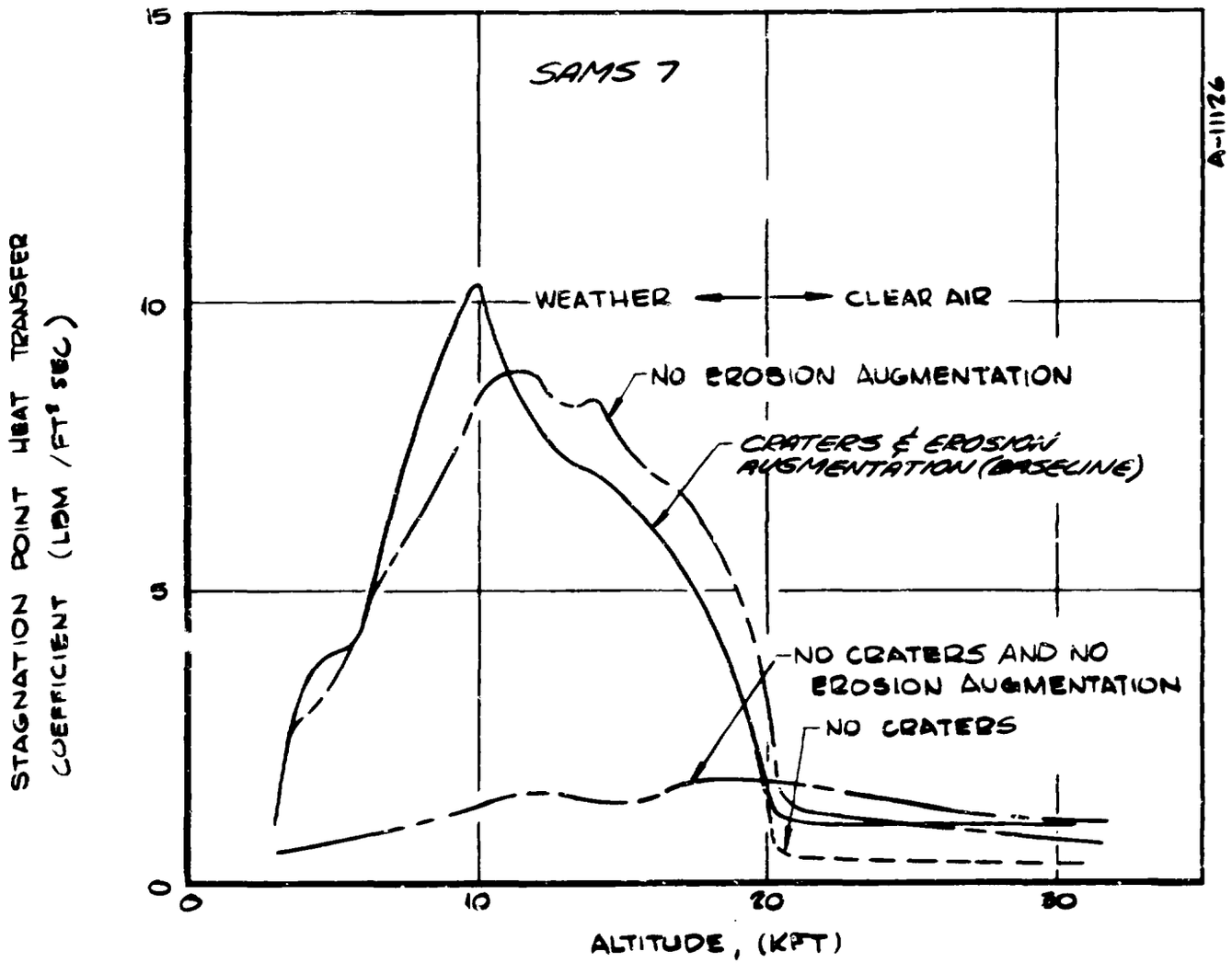

Figure 4-9. Comparison of stagnation point heat transfer coefficients versus altitude for SAMS 7.

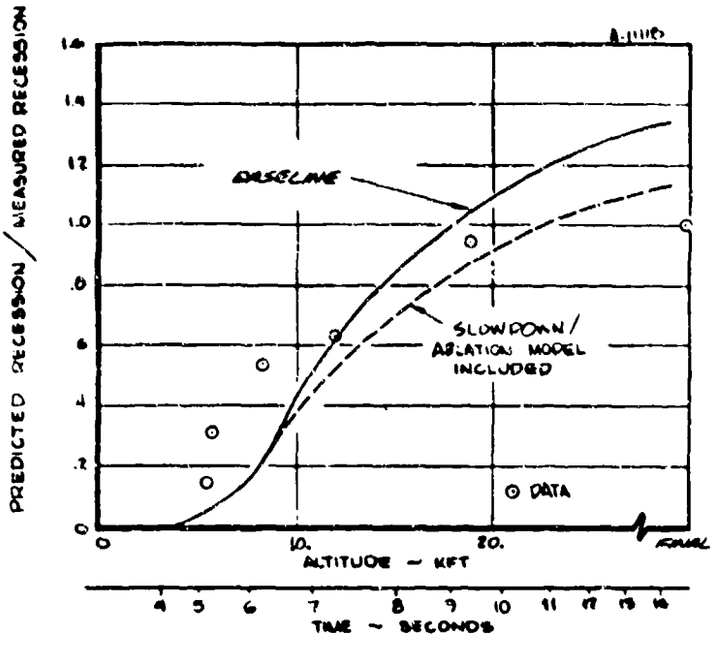

(a) SAMS 6

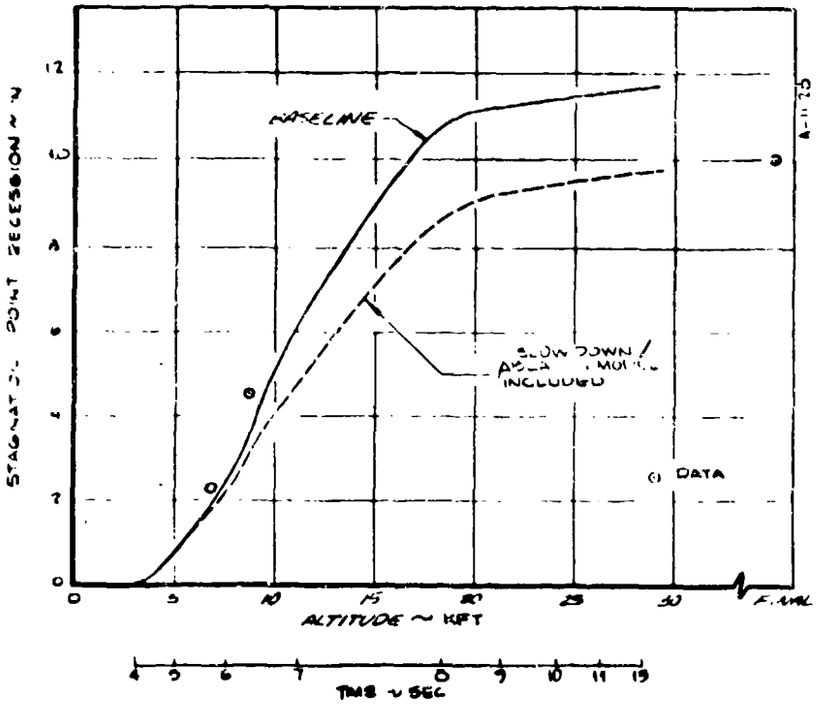

(b) SAMS 7

Figure 4-10. Erosion/ablation calculations allowing particle slowdown/ablation.

Summary

The significant results of the weather effects sensitivity calculations for the Terrier-Recruit flight conditions are as follows:

- A significant portion of the mass loss is associated with ablation due to the coupled effects of hydrometeor encounters on the surface heat transfer.
- The coupling between erosion and ablation is accomplished through either crater roughness or erosion augmentation modeling.
- For the Terrier-Recruit flight conditions, crater roughness and erosion augmentation effects are comparable although augmentation generally dominates slightly.
- Ablation healing of craters reduces crater roughness less than 10 percent for the SAMS 6 and SAMS 7 trajectory and weather conditions; this reduction makes a negligible change in surface heat transfer.
- For the SAMS 6 and SAMS 7 flight cases, the particle slowdown and ablation model significantly affects predicted recession by reducing the mass of the impacting particles.* The particle slowdown was small.
- The water drop stripping and breakage model had little effect on the predicted nosetip response; presumably because only a single, relatively large, particle size was assumed.
- Because both erosion and ablation at Terrier-Recruit flight are closely dependent upon the erosion mass loss ratio, recession is directly related to changes in the mass loss correlation.

The recovered nosetips from SAMS tests indicate both the overall stagnation point recession and the nosetip shape, including the cone surface recession. Comparisons between computed and measured shape profiles show the adequacy of the shape modeling numerics. Figure 4-11 presents scaled comparisons of shape profiles for SAMS 6. The measured shape is shown by the short dashed lines, solid lines indicate the two solutions from the sensitivity matrix which best matched the overall recession data (Solutions 3 and 8 of Table 4-2). The computed side surface recession is much greater than observed, even for the slowdown/ablation case where cone region particles demise before impact. It is probable that transient heat conduction effects, not modeled in the sensitivity solutions, would reduce side wall recession substantially. The comparisons of nose region shapes are quite favorable, in that both the measured and computed were quite blunt.

---

*The particle slowdown/ablation model is derived for steady state particle vaporization. Later calculations reported in PANT Interim Volume XIX showed that droplets do not vaporize at SAMS conditions (Mach < 10.).

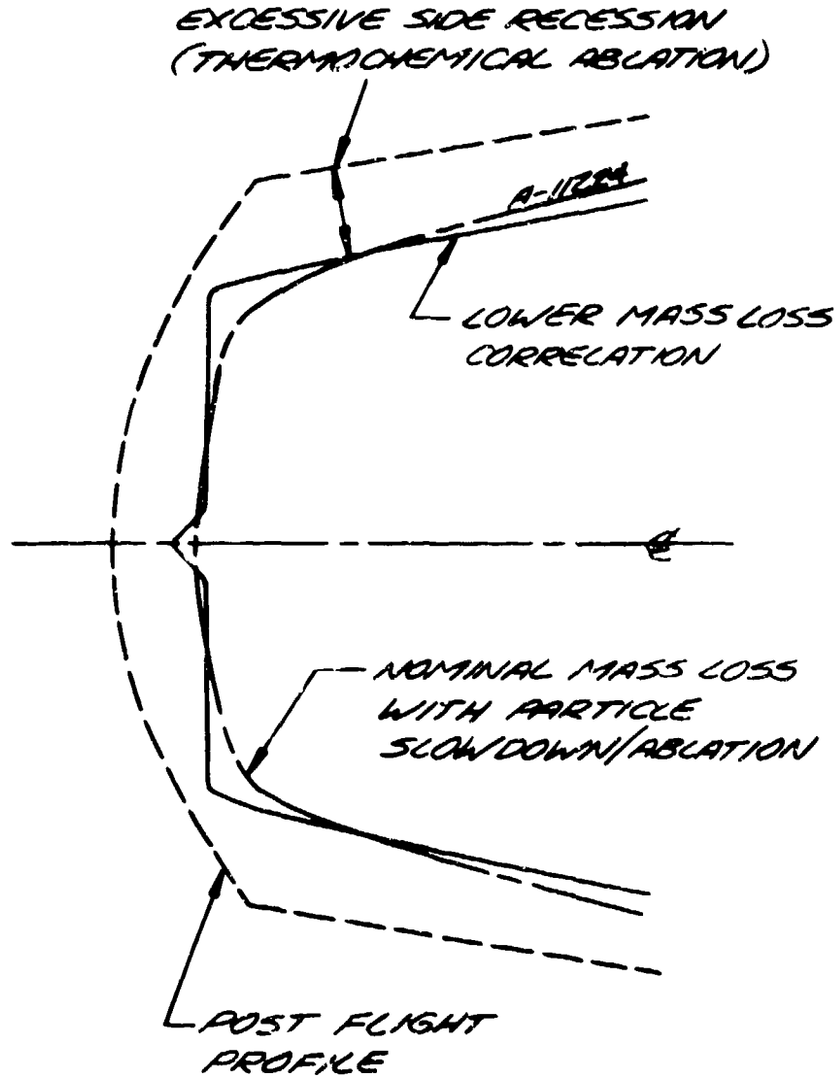

Figure 4-11. Relative final shape comparisons for SAMS 6.

SECTION 5

ALTERNATE-MATERIAL EROS CODE CALCULATIONS

Two additional SAMS, Terrier-Recruit, flight cases were analyzed using the EROS computer code. There were Sandia Tests Number R487411 and R487406. The objective of these analyses is to check out the alternate material modeling capability of the EROS code on a charring ablator and an alternate graphitic material. These tests were conducted from Wallops Station, Wallops Island, Virginia on 8 April 1974. Trajectory and weather data were obtained from Reference 16, and the key flight test parameters are summarized in Table 5-1. Pertinent trajectory quantities are shown in Figure 5-1; the weather parameters (liquid water content and median particle diameter) used in the computer analyses are displayed in Figure 5-2. The nosetip configuration is unchanged from the SAMS 6 and SAMS 7 flight (refer to Figure 4-2).

TABLE 5-1. SAMS FLIGHT TEST PARAMETERS

Parameter	R487411	R487406
Peak Velocity ft/sec	8600	8600
Peak Stag. Press., atm	58	58
Nose Radius, inches	.625	.625
Core Angle, degrees	9	9
WSI, km^2-gm/m^3	2.1	2.1
Nosetip Material	Carbon/Carbon	Carbon Phenolic

The erosion mass loss modeling for the carbon phenolic material (Flight R487406 is summarized in Reference 20. The mass loss correlation for Flight R487411 taken to be the one recommended for use with M III-A carbon/carbon in Reference 1. It has the form:

$$G \propto V^{1.4} \sin(\quad)$$

The ablation response modeling of carbon phenolic is reviewed in Reference 20. The modeling of the carbon/carbon was assumed identical to that used for the SAMS 6 and SAMS 7 solutions (Section 4).

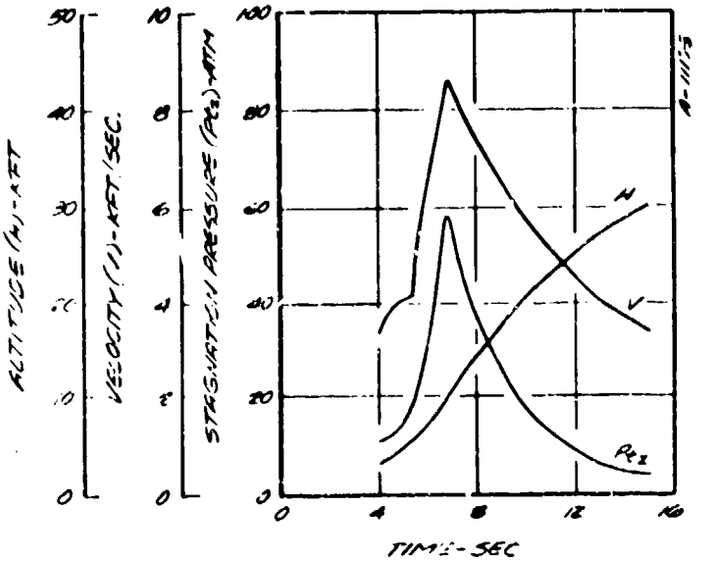

(a) SAMS Test R487411, carbon/carbon

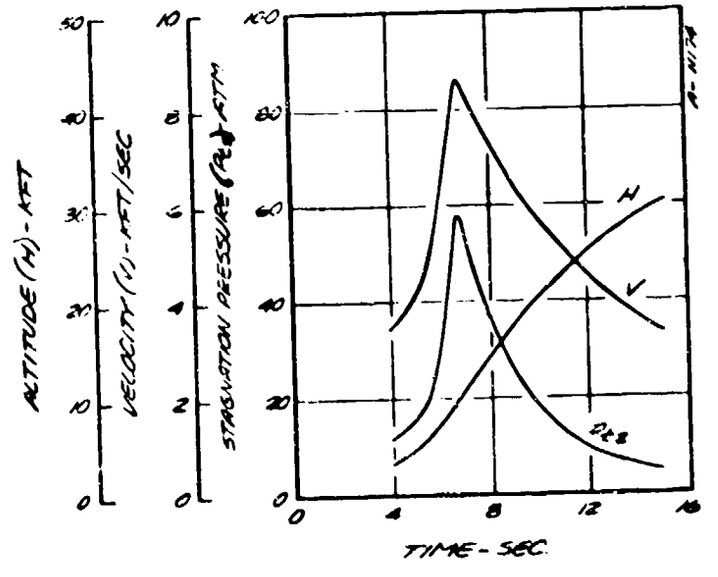

(b) SAMS Test R487406, carbon phenolic

Figure 5-1. Trajectory parameters.

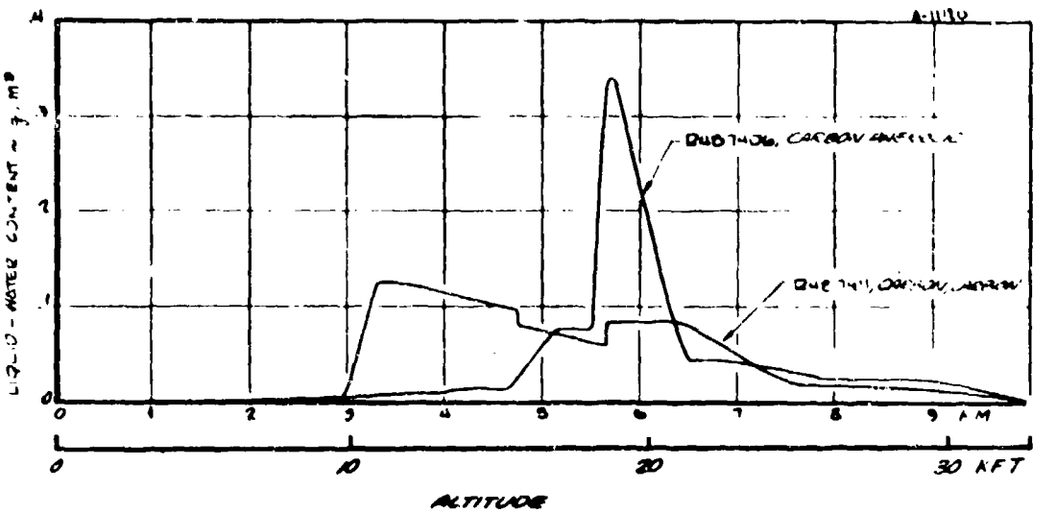

(a) Liquid water content distributions

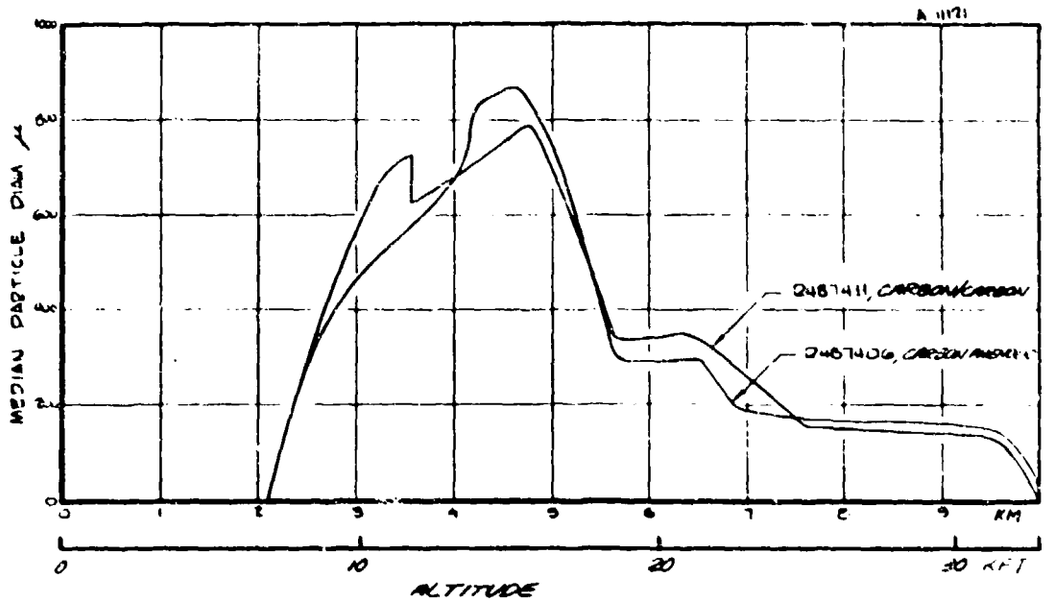

(b) Median particle diameter distributions

Figure 5-2. Weather profiles.

The analysis results are presented as shape profile histories and stagnation point recession histories in Figures 5-3 and 5-4.

The conclusions is that the EROS code functioned properly for the two alternate material flight test cases. No data were available at this writing for comparison with the EROS code solutions.

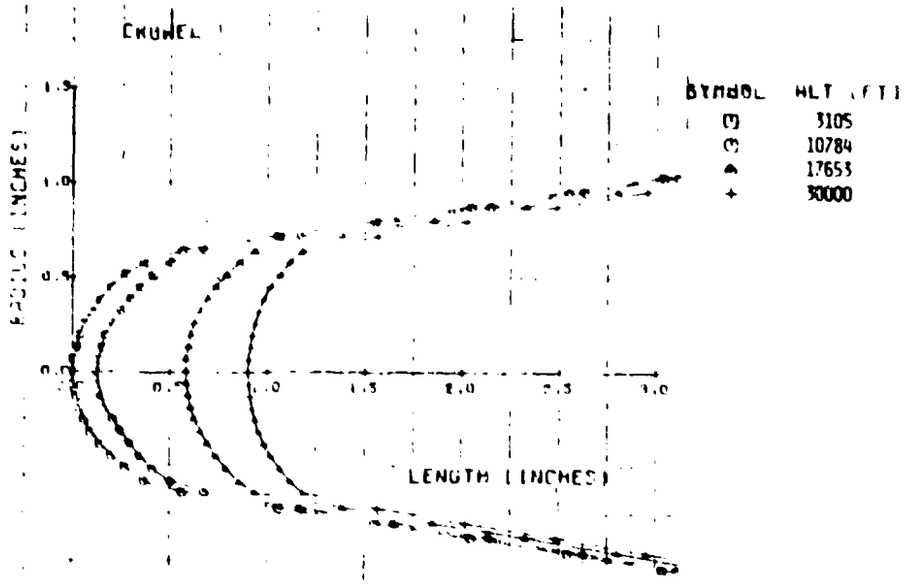

(a) Shape profile history

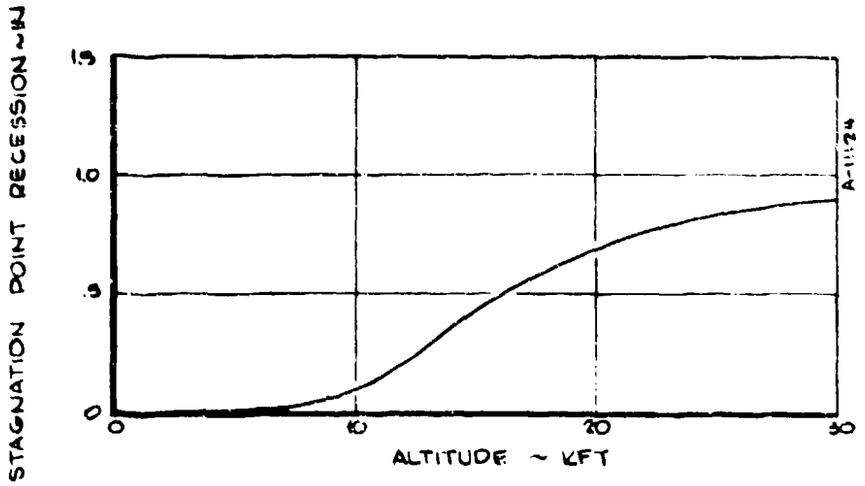

(b) Recession history

Figure 5-3. Nosetip response prediction for SAMS Flight R487411, carbon/carbon.

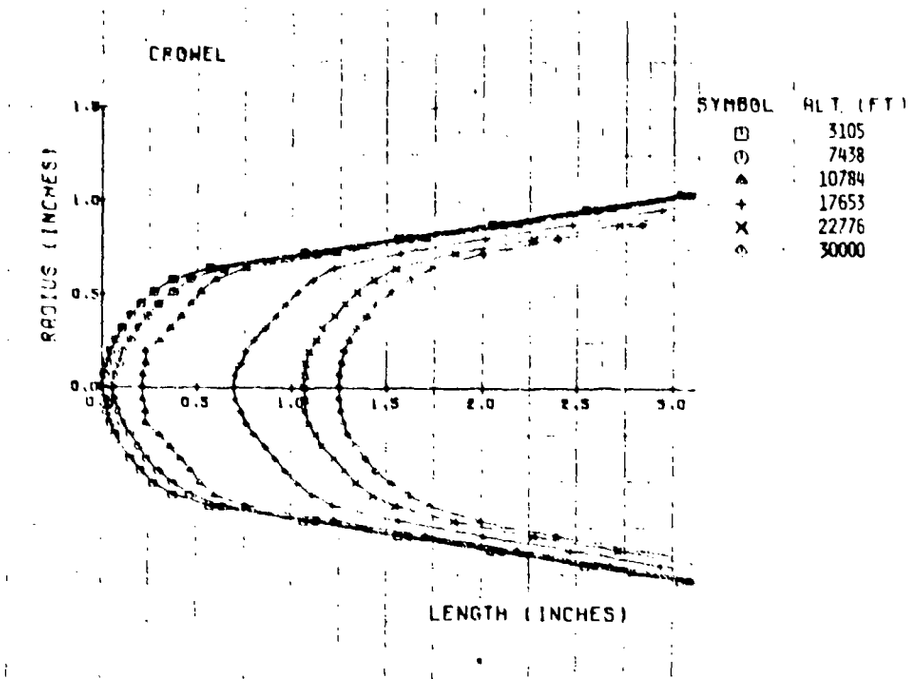

(a) Shape profile history

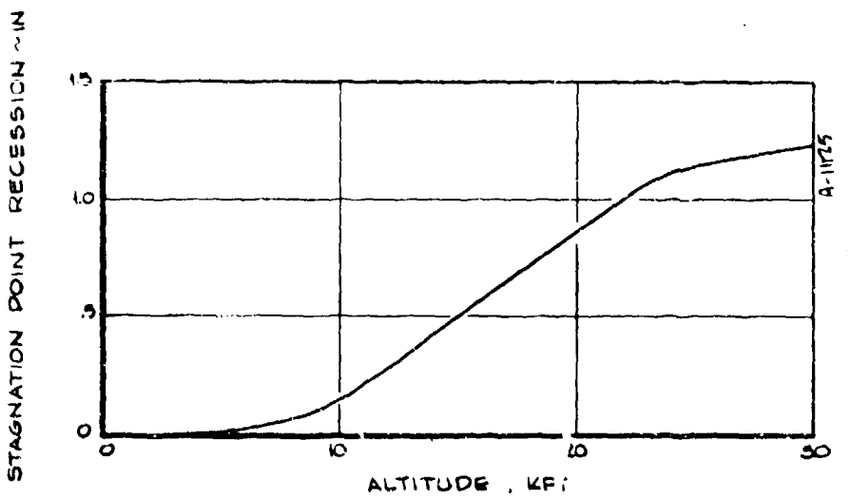

(b) Recession history

Figure 5-4. Nosetip response prediction for SAMS Flight R487406, carbon phenolic.

SECTION 6

CONCLUSIONS AND RECOMMENDATIONS

Conclusions are summarized in Section 6.1 and recommendations are listed in Section 6.2.

6.1 CONCLUSIONS

The EROS code was exercised to determine code reliability and computational consistency for wind tunnel test environments, clear air flight environments, and weather flight environments. Solutions were performed exercising various modeling perturbations, and from these solutions, the sensitivity of the EROS code predictions to key modeling variations and/or uncertainties was demonstrated. The primary conclusions from the code calculations may be summarized as follows:

Comparisons to Wind Tunnel Data

1. Slight improvements in the calculations of bow shock and turbulent heat transfer were achieved.
2. Shape change solutions compared favorably with low temperature ablation data, although for one case overall recession was inaccurate because of deficiencies in scallop roughness modeling.

Clear Air Shape Change Sensitivity Studies

3. The total recession of an ICBM nosetip at typical conditions is overwhelmingly dependent upon the transition altitude.
4. Based on the PANT roughwall transition criterion, transition altitude is extremely sensitive to the value of the surface roughness which exists during laminar ablation; greatest sensitivity occurs for roughness values between 0.2 and 0.4 mils for typical reentry situations.
5. If the PANT roughwall heating model is correct and applicable to ablation-induced scalloped surfaces, then a factor of two decrease in scallop dimension produces a relatively small (12 to 18 percent) decrease in nosetip recession rate.

6. The transitional heat transfer modeling affects the flight time required for nosetip sharpening.

7. Two-dimensional heat conduction is important but not critical to the evaluation of shape and recession trends for graphitic materials. The two-dimensional heat conduction towards the centerline generally increases stagnation point recession and produces a slightly larger nose radius shape than is predicted assuming steady-state, one-dimensional heat conduction.

Coupled Erosion/Ablation Sensitivity Calculations for Graphite

8. For the Terrier-Recruit flights analyzed, the coupled effect of erosion on ablation mass loss is very significant. Computed ablation including weather effects is 40 to 50 percent of total mass loss. Coupled effects would also be significant for light or mild weather encounters at ICBM conditions.

9. The hydrometeor encounter increases surface heat transfer and ablation through either erosion augmentation or crater roughness formation. For the Terrier-Recruit conditions, erosion augmentation was slightly greater than the crater effects.

10. Uncertainties in mass loss ratio correlations have a significant impact on the nosetip recession calculation. However, mass loss uncertainties at Terrier-Recruit conditions are probably within weather definition uncertainties.

11. For the nominal erosion mass loss correlation, modeling of particle slowdown and ablation in the shock layer significantly affected the computed response.

12. The crater healing and particle stripping/breakup models had negligible effect on the Terrier-Recruit calculations.

Alternate Material Erosion/Ablation Calculations

13. Two coupled erosion/ablation shape change solutions were performed to check out the generalized material modeling capability of the EROS code. These solutions were successfully completed.

6.2 RECOMMENDATIONS

Recommendations apparent from the EROS code checkout calculations are as follows:

1. Since clear air nosetip response is critically dependent upon the intrinsic surface roughness during laminar ablation, this material property, its uncertainty and its variability within a particular billet should be thoroughly characterized prior to qualification of the material.
2. Additional effort is required to understand the effects of roughness variabilities on the nosetip response.
3. Applicability of the PANT, roughwall, turbulent heating model to scalloped surfaces should be assessed in relation to other techniques currently in use.
4. The sensitivity of EROS code predictions to time step size and surface coordinate definition procedures should be evaluated.
5. The EROS code heat conduction procedure requires generalization to allow multiple in-depth back-up materials and improvement of stagnation point recession calculation.
6. Physical justifications for the erosion mass loss correlations and the erosion augmentation formulations in current use are required before extrapolation to ICBM conditions can be done with confidence.
7. Particle/shock layer interactions should be included in coupled effects modeling for Mach > 10.*

*See PANT Interim Volume XIX.

REFERENCES

1. Berry, R. A. Lee, L. C., Kreibel, A. R., Nardo, C. T., and Wool M. R., "Passive Nosetip Technology (PANT) Program, Interim Report, Vol. XVI – Investigation of Erosion Mechanics on Reentry Materials (U)," SAMSO-TR-74-86, Aerotherm Report 75-139, Aerotherm Division/Acurex Corporation, Contract F04701-74-C-0069, CDRL B001, March 1975 (SECRET).

2. Crowell, P., "Turbulent Heating Near a Stagnation Point," Interoffice Memorandum 73-5134.5-010, The Aerospace Corporation, March 19, 1973.

3. Rafinejad, D. A. and Derbidge, T. C., "Passive Nosetip Technology (PANT) Program, Interim Report, Vol. XVII – Computer User's Manual, EROsion Shape (EROS) Computer Code," SAMSO-TR-74-86, Aerotherm Report UM-74-57, Aerotherm Division/Acurex Corporation, Contract F04701-74-C-0069, CDRL B002, December 1974.

4. Private communication with P. Crowell, The Aerospace Corporation, March 1971.

5. Wool, M. R., "Passive Nosetip Technology (PANT) Program, Interim Report, Vol. X – Summary of Experimental and Analytical Results for the Period May 1973 to December 1974," SAMSO-TR-74-86, Aerotherm Report 74-100, Aerotherm Division/Acurex Corporation, January 1975.

6. Powars, C. A., "Passive Nosetip Technology (PANT) Program, Interim Report, Vol. III – Surface Roughness Effects, Part II – Roughness Augmented Heating Data Correlation and Analysis (U)," SAMSO TR-74-86, Aerotherm Report 74-90, Aerotherm Division/Acurex Corporation, January 1974 (Confidential).

7. Maurer, R. E., et al., "Passive Nosetip Technology (PANT) Program, Interim Report, Vol. VI – Graphite Ablation Data Correlation and Analysis (U)," SAMSO TR-74-86, Aerotherm Report 74-90, Aerotherm Division/Acurex Corporation, January 1974 (Confidential).

8. Moyer, C. B. and Rindal, R. A., "Finite Difference Solution of the In-Depth Response of Charring Materials Considering Surface Chemical and Energy Balances, NASA CR-1061, June 1968.

9. Jackson, M. D. and Baker, D. L., "Passive Nosetip Technology (PANT) Program, Interim Report, Vol. IV – Heat Transfer and Pressure Distributions on Ablated Shapes, Part I – Experimental Data, SAMSO-TR-74-86, Aerotherm Report 74-90, Aerotherm Division/Acurex Corporation, January 1974.

10. Jackson, M. D., "Passive Nosetip Technology (PANT) Program, Interim Report, Vol. XV – Roughness Induced Transition Experiments – Data Report," SAMSO TR-74-86, Aerotherm Report 74-100, Aerotherm Division/Acurex Corporation, August 1974.

11. Wool, M. R., Overly, P. T., and Derbidge, T. C., "Passive Nosetip Technology (PANT) Program, Interim Report, Vol. VII – Computer User's Manual, Steady-State Analysis of Ablating Nosetips (SAANT) Program," SAMSO TR-74-86, Aerotherm Report 74-90, Aerotherm Division/Acurex Corporation, January 1974.

12. Abbett, M. J. and Davis, J. E., "Passive Nosetip Technology (PANT) Program, Interim Report, Vol. IV – Heat Transfer and Pressure Distribution on Ablated Shapes, Part II – Data Correlation and Analysis, SAMSO TR-74-86, Aerotherm Report 74-90, Aerotherm Division/Acurex Corporation, January 1974.

13. Neuner, G. J., et al., Passive Nosetip Technology (PANT), Interim Report, Vol. XXIII – Nosetip Flight Data Analyses," SAMSO TR-74-86, to be published.

14. White, C. A. and Grabow, R. M., "Influence of Scallop Roughness on Nosetip Shape Behavior," SAMSO TR-73-88, January 1973.

15. Cole, J. K., Church, H. W., and Rollstin, L. R., "Test Report for SAMS Rain Erosion Flights 6, 7, and 8 (U)," Sandia Laboratories Report SLA-73-0813, February 1974.

16. Private communication with W. Portenier, Aerospace Corporation, El Segundo, California, October 22, 1975.

17. Courtney, J. F., et al., "Nosetip Material and Geometry Effects on Aerodynamic Heating in Erosion Environments," DNA 3481F, Science Applications, Inc., Report 74-540-LA, August 1974.

18. Jaffe, N. A., "Droplet Dynamics in a Hypersonic Shock Layer," AIAA Journal, Vol. 11, No. 11, November 1973.

19. Waldman, G. D., Reinecke, W. G., and Glenn, D. C., "Raindrop Breakup in the Shock Layer of a High-Speed Vehicle, AIAA Journal, Vol. 10, No. 9, Septemer 1972.

20. Wool, M. R., et al., "Minuteman MK12 Nosetip Performance Assessment (U)," Aerotherm Report 74-124, Aerotherm Division/Acurex Corporation, Contract F04701-74-C-0069, CDRL A001-A003, Novebmer 1974.

APPENDIX

SHAPE PROFILE HISTORIES FROM CLEAR AIR PARAMETRIC SOLUTIONS

Table A-1 identifies the fifteen shape response solutions completed as a part of the EROS code check out calculations. The shape profile histories for these solutions are given in Figures A-1 through A-15.

TABLE A-1. MATRIX FOR ABLATION MODELING PARAMETRIC SOLUTIONS

Solution	Reentry Case	Transition Modeling		Macroroughness Modeling[b]	Shock Shape Modeling	Objective Relative to Baseline Assumptions
		Microroughness (mil)	Criterion[a]			
1	1 (R_N = 1.25 in)	0.27	$Re_k\ (S/\delta^*)^{1/3}$	$k_t = 0.93\ P_e^{-0.77}$	New (Ref 1)	Baseline for Case 1
2		0.20				Smaller microroughness
3		0.30				Larger microroughness
4		0.20		$k_t = 0.93\ P_{t2}^{-0.77}$		Smaller microroughness and macroroughness
5		0.27		$k_t = 0.93\ P_e^{-0.77}$	Old (Ref 11)	Change from old shock shape modeling
6	2 (R_N = 0.75 in)	0.40			New (Ref 1)	Baseline for Case 2
7		0.20				Smaller microroughness
8		0.60				Larger microroughness
9[c]		0.60	$Re_\theta\ (k/\psi\theta)^{0.7}$			Alternate transition criterion with larger microroughness
10		0.40	$Re_k\ (S/\delta^*)^{1/3}$ Sharp			Transitional heating assumption
11		0.40	$Re_k\ (S/\delta^*)^{1/3}$	$k_t = 0.93\ P_{t2}^{-0.77}$		Smaller macroroughness
12[c]		0.40	$Re_\theta\ (k/\psi\theta)^{0.7}$	k_t = 1.0 mil		Alternate transition criterion plus lower macroroughness
13		0.40	$Re_k\ (S/\delta^*)^{1/3}$	$k_t = 0.93\ P_e^{-0.77}$	Old (Ref 11)	Change from old shock shape modeling

[a] Column identifies various PANT transition criteria described in Reference 5 and 11; "Sharp" means immediate transition with no transitional heating length allowed.

[b] Terminal scallop dimensions modeled as a function of either stagnation pressure (P_{t2}) or edge pressure (Pe); K_t used directly in PANT roughwall heating correlation (Reference 6).

[c] Solutions 9 and 12 performed using both transient and steady state conduction modeling.

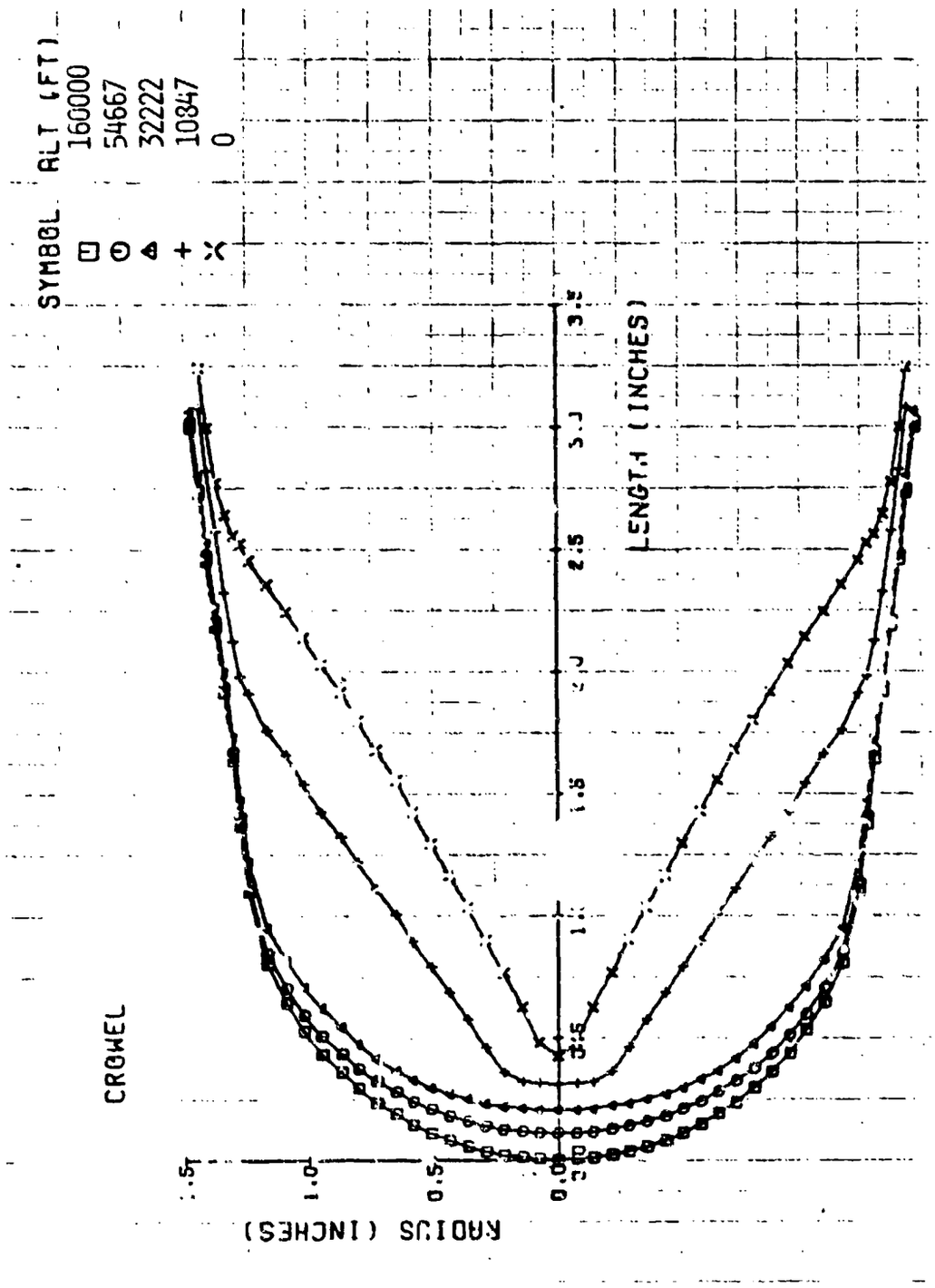

Figure A-1. Solution 1, case 1 baseline prediction.

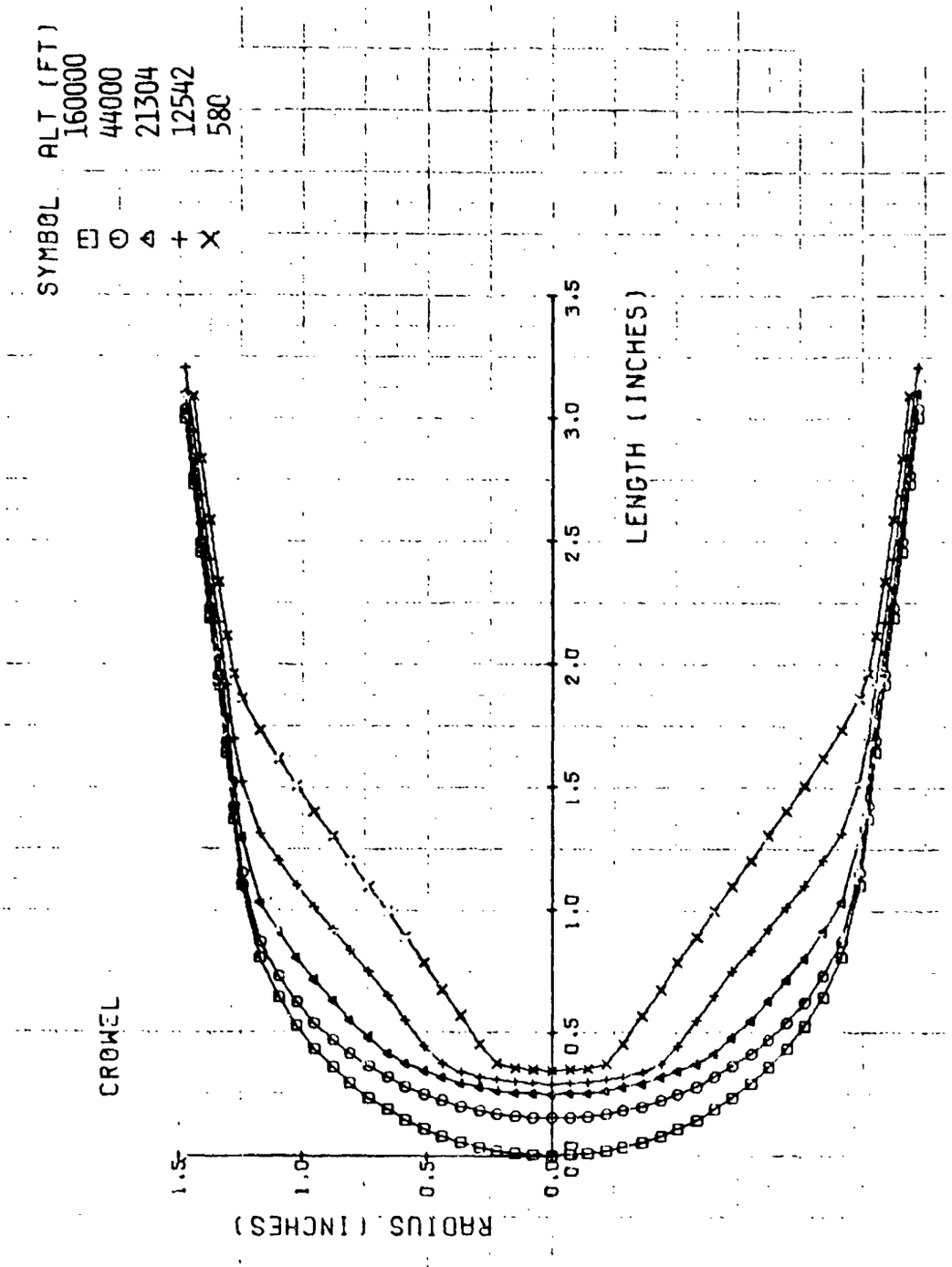

Figure A-2. Solution 2, case 1 smaller microroughness.

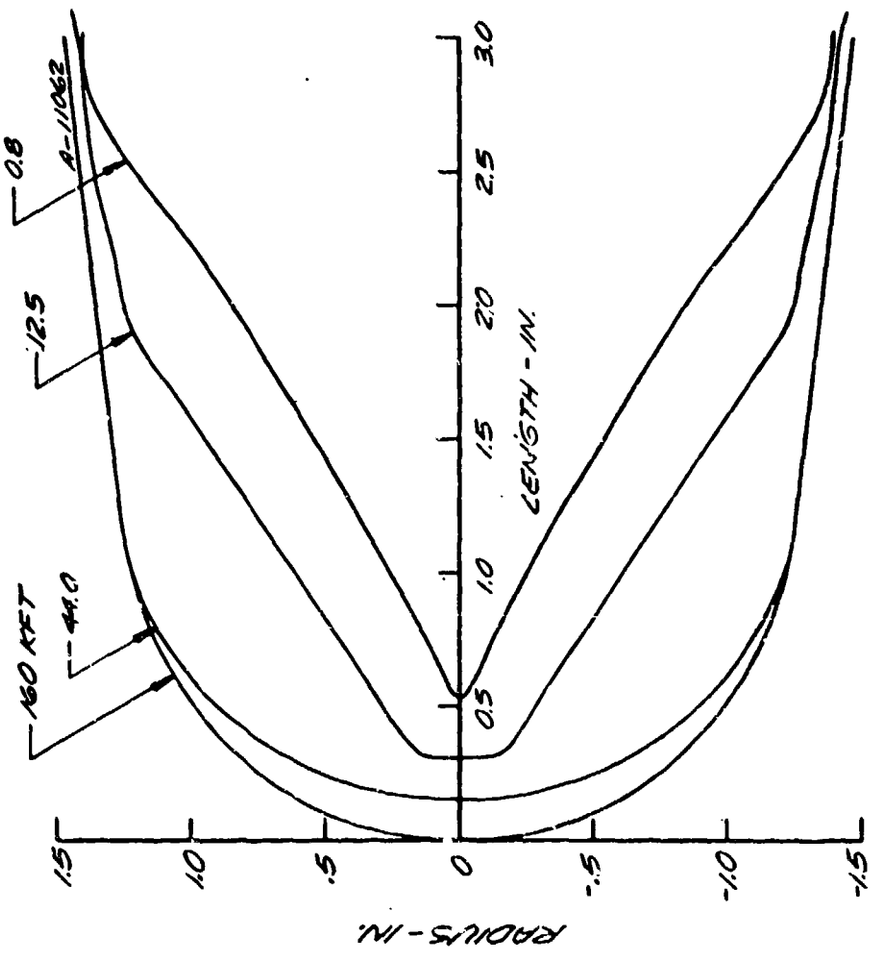

Figure A-3. Solution 3, case 1 larger microroughness.

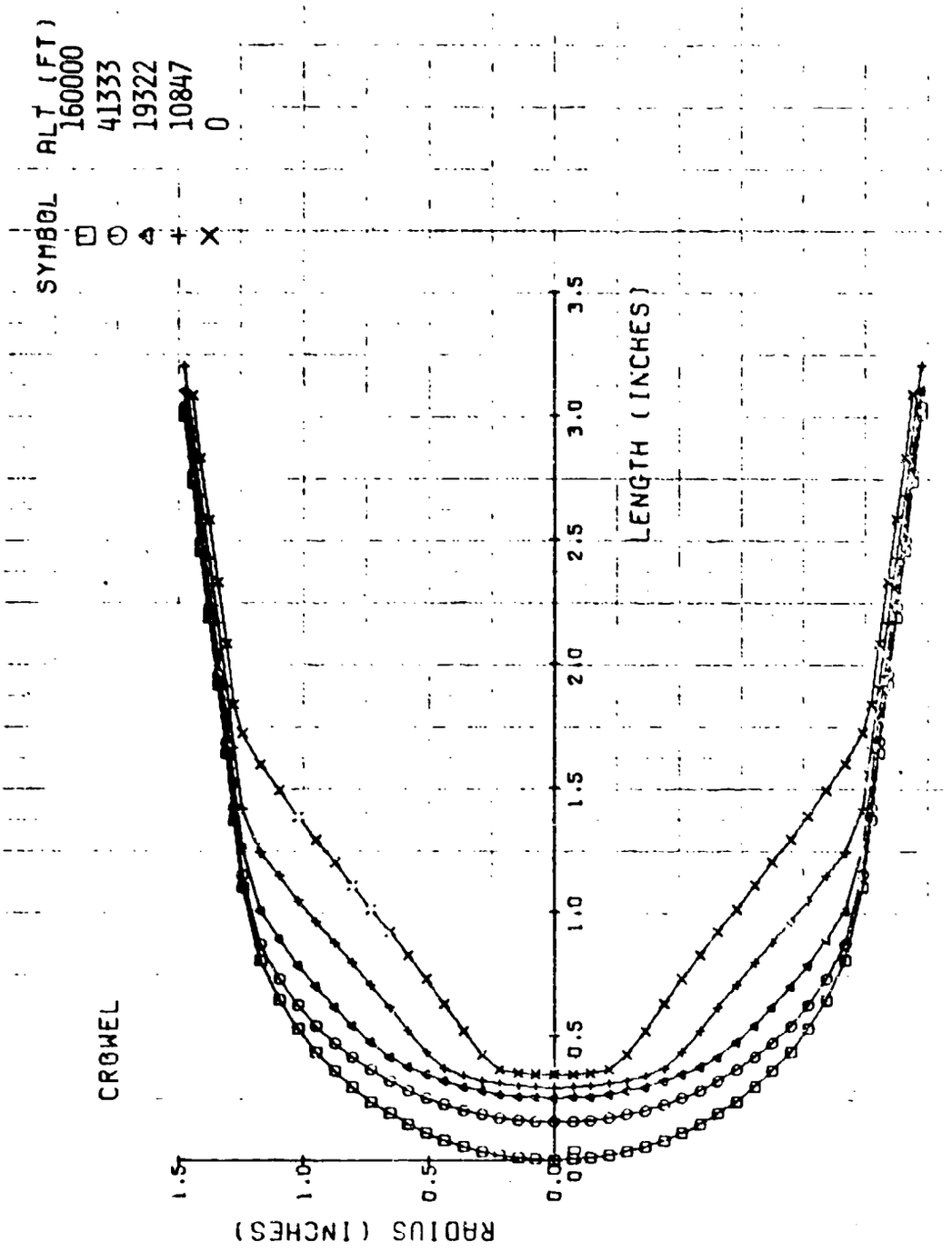

Figure A-4. Solution 4, case 1 smaller micro and macroroughness.

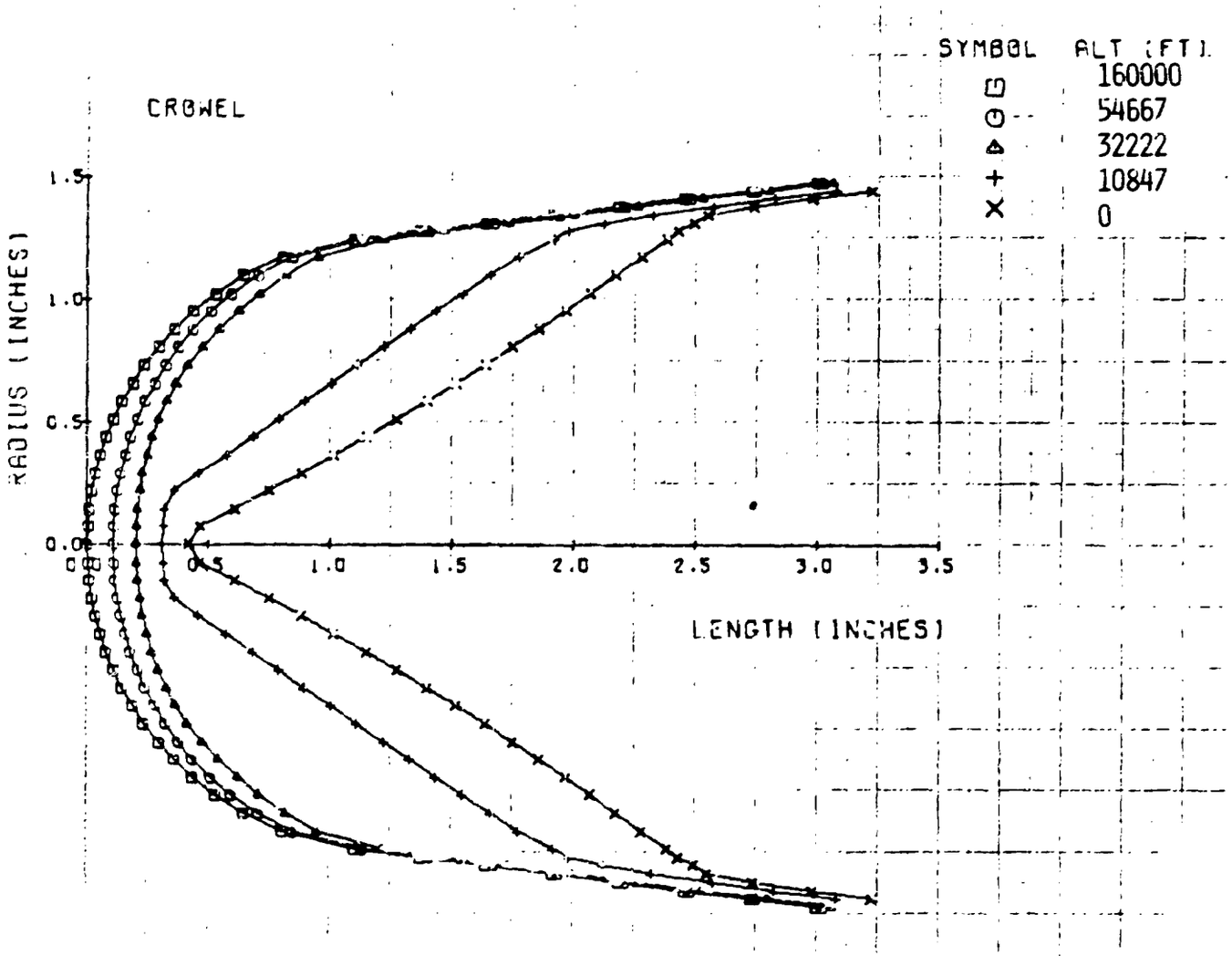

Figure A-5. Solution 5, case 1 effect of shock shape model.

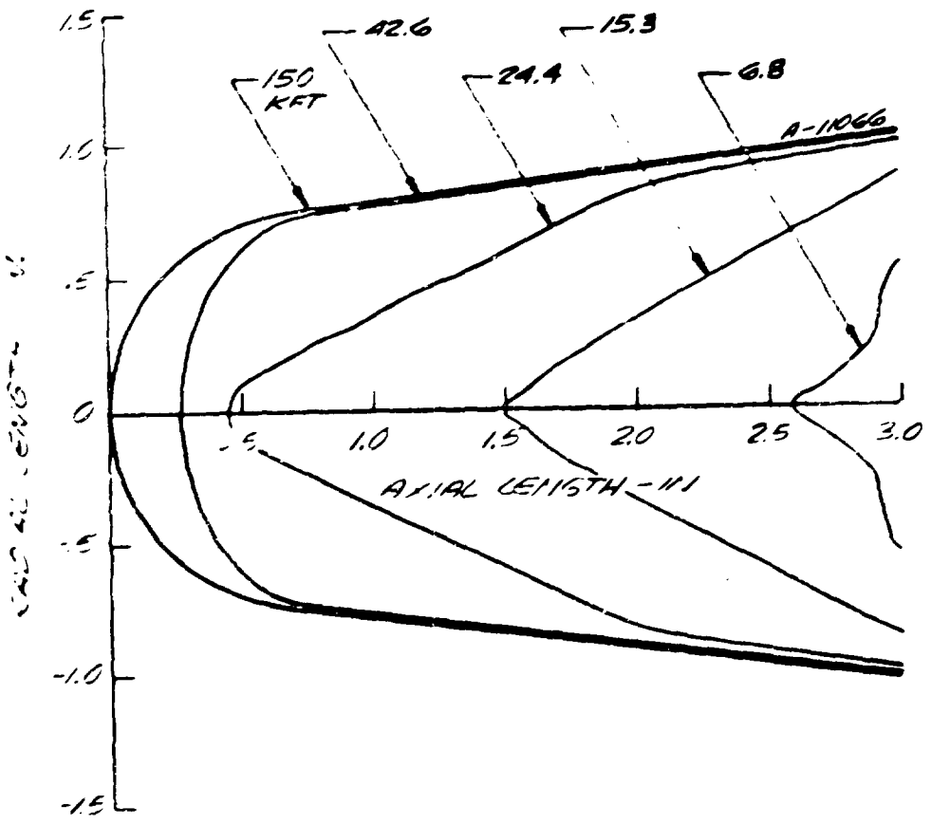

Figure A-6. Solution 6, case 2 baseline.

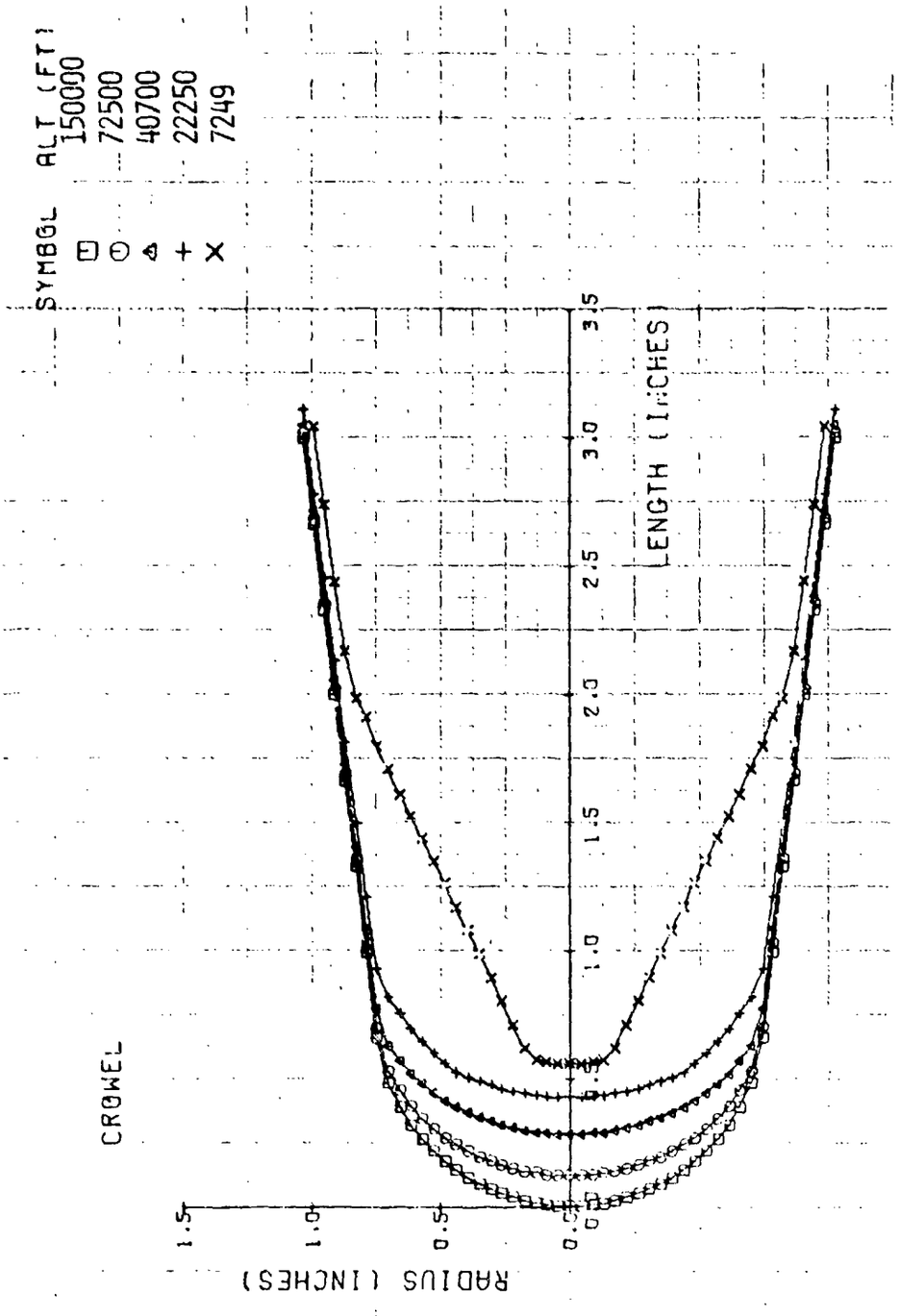

Figure A-7. Solution 7, case 2 smaller microroughness.

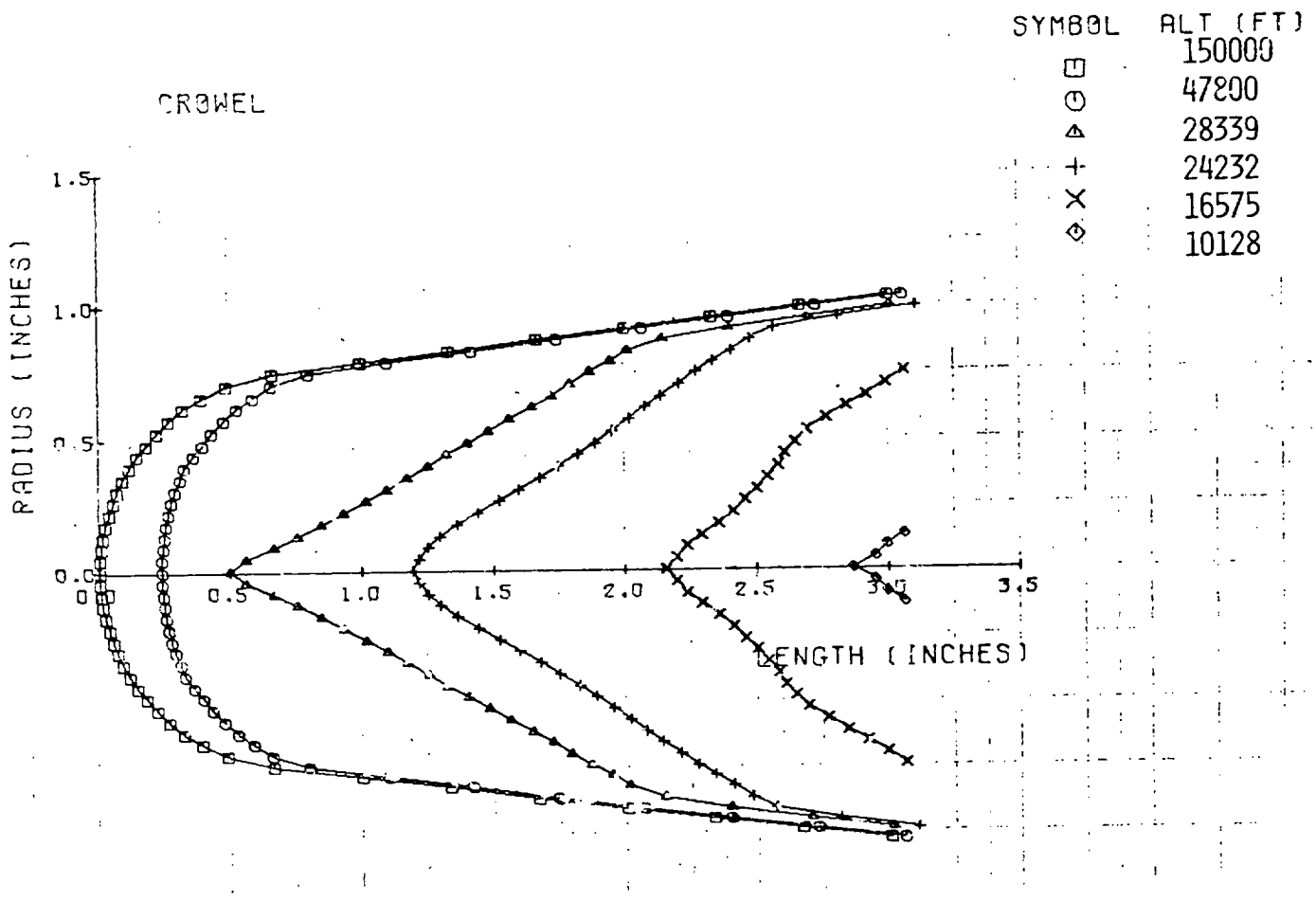

Figure A-8. Solution 8, case 2 larger microroughness.

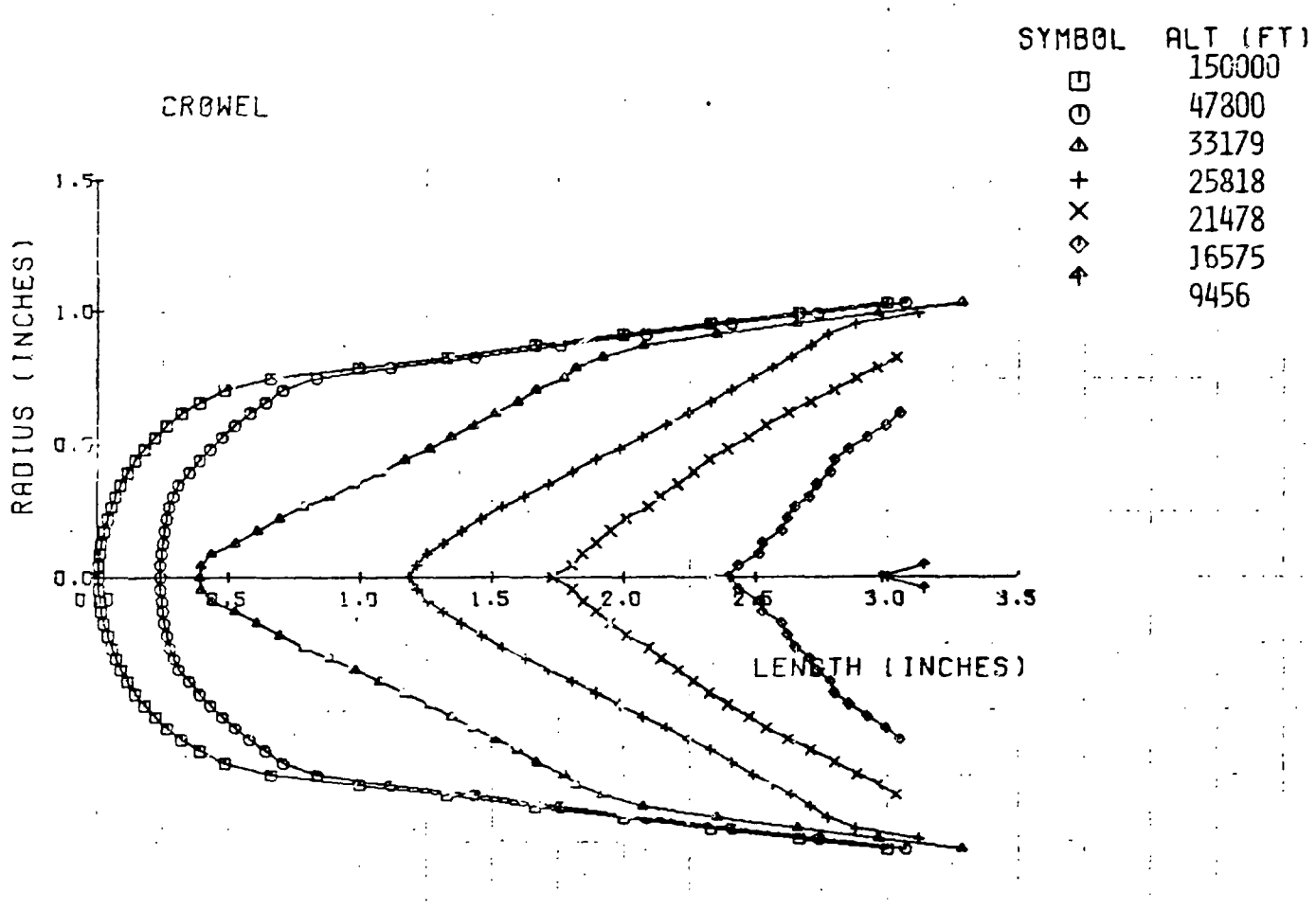

Figure A-9. Solution 9, case 2 alternate transition criterion (steady state).

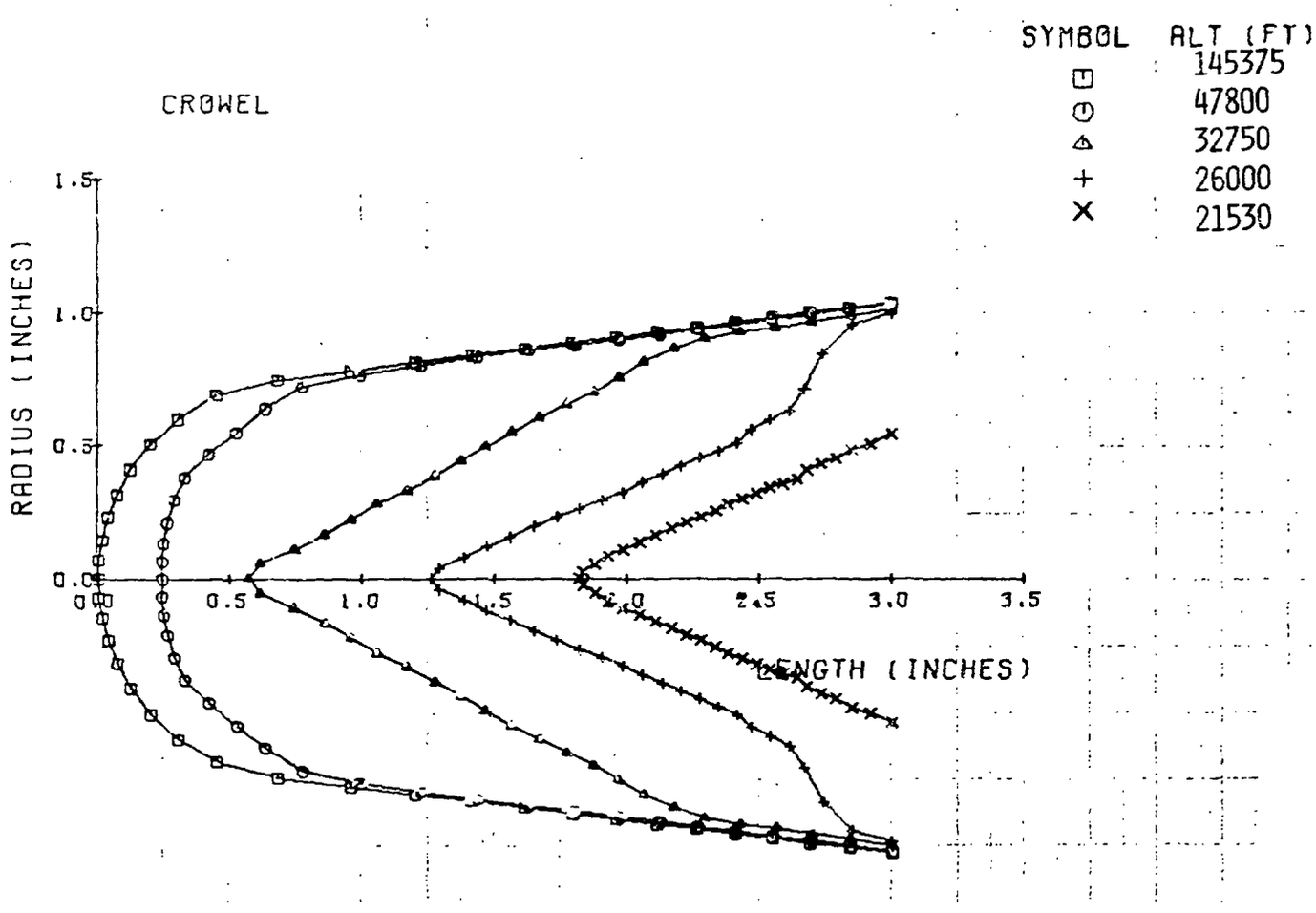

Figure A-10. Solution 9, case 2 alternate transition criterion (transient).

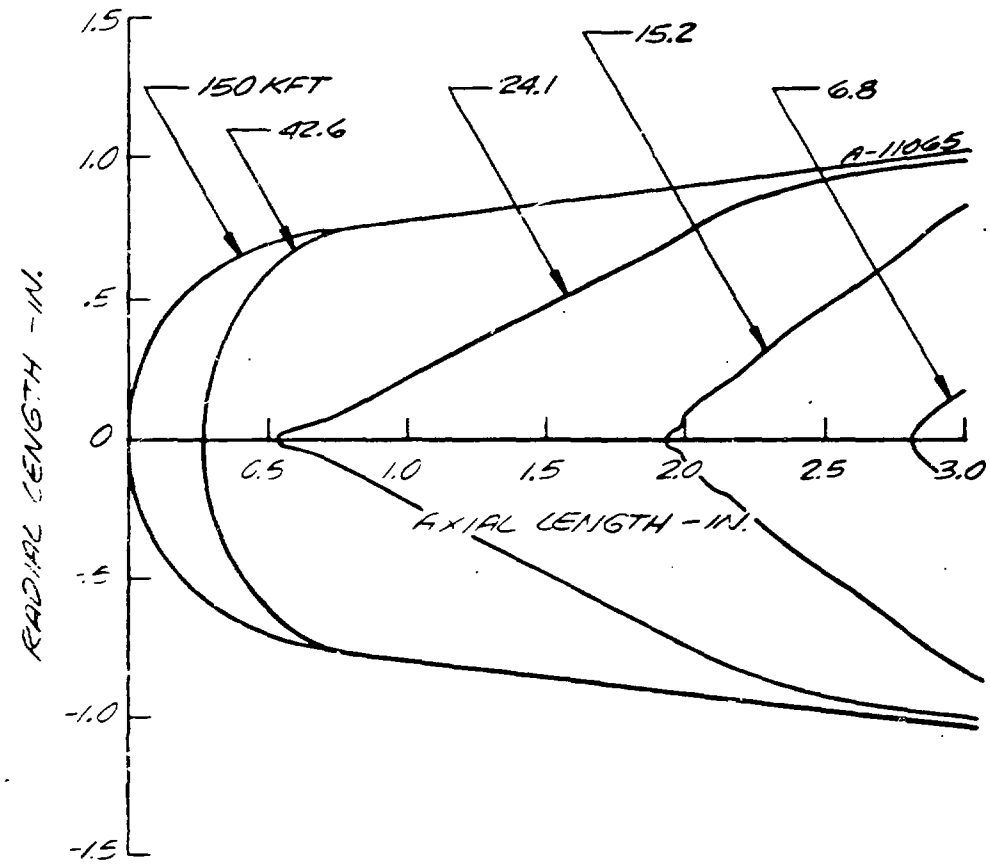

Figure A-11. Case 2 smaller macroroughness.

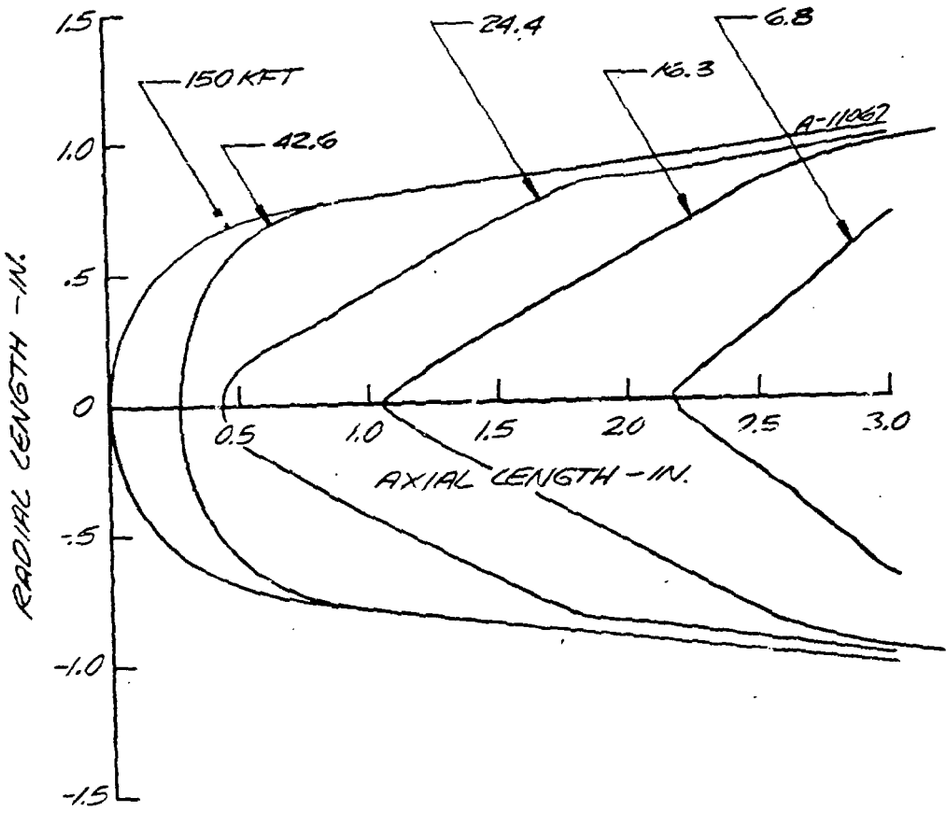

Figure A-12. Case 2, alternate transition criterion plus lower macroroughness.

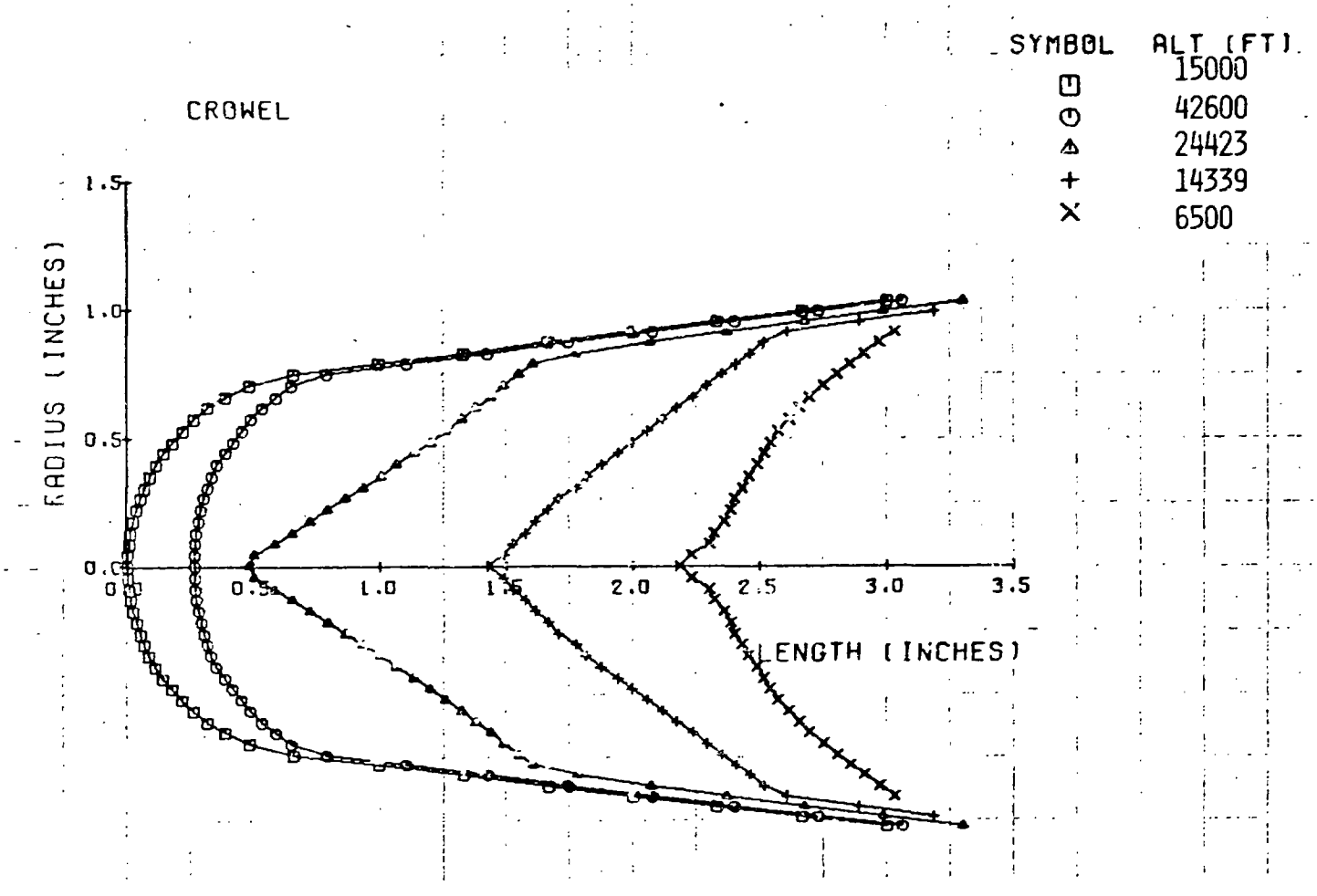

Figure A-13. Solution 12, case 2 alternate micro and microroughnesses (steady state)

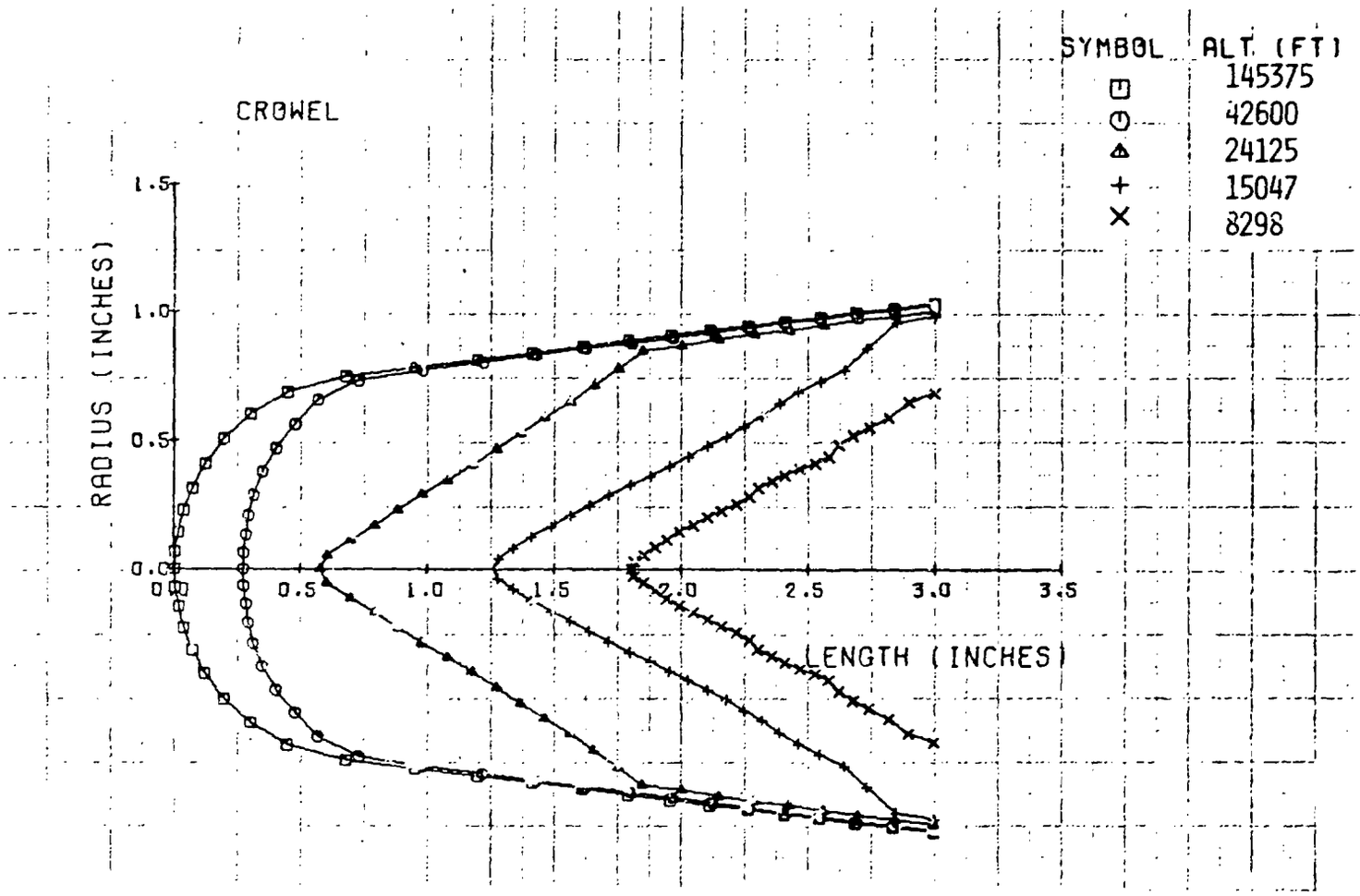

Figure A-14. Solution 12, case 2 alternate micro and macroroughnesses (transient).

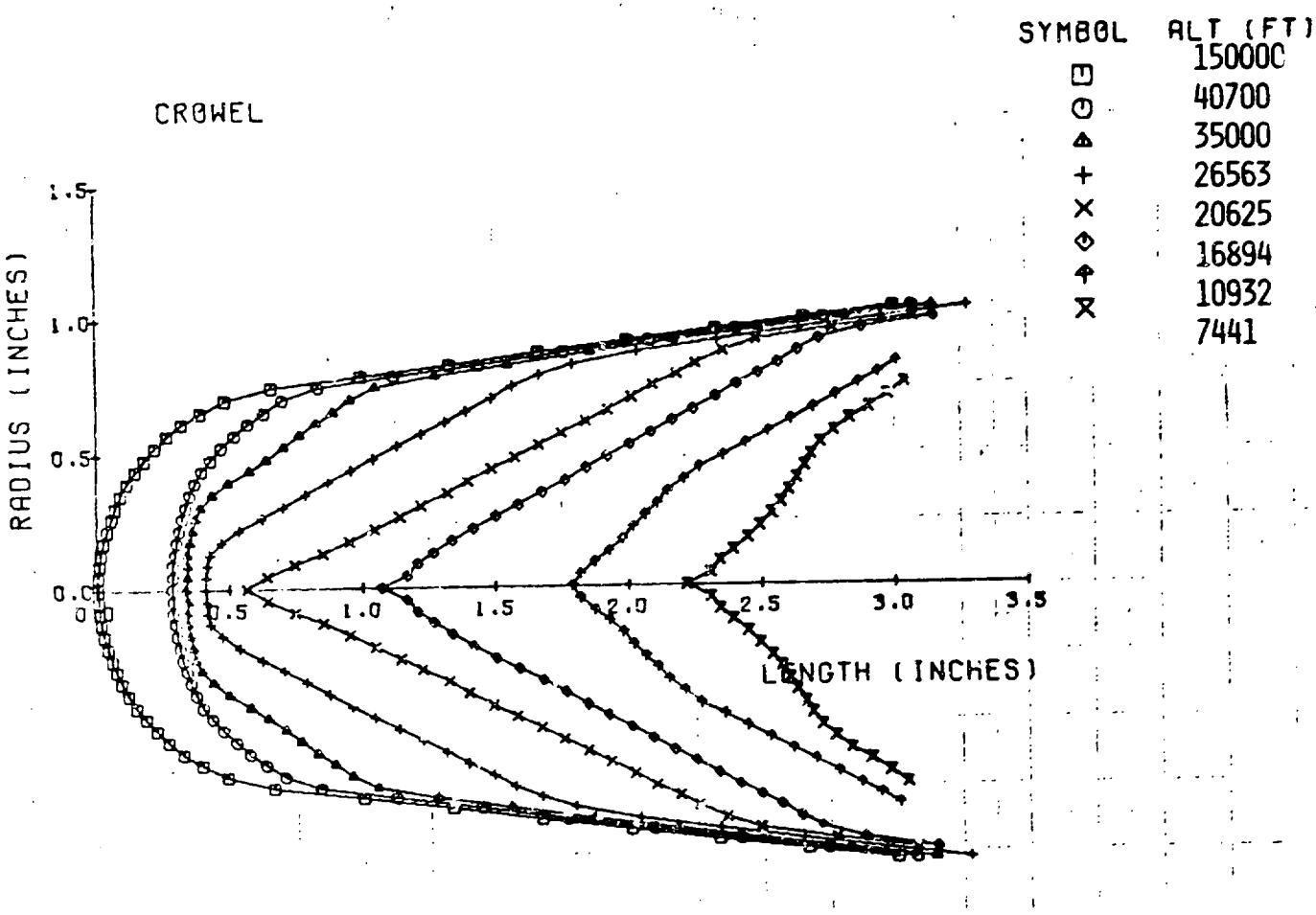

Figure A-15. Solution 13, case 2 effect of shock shape modeling.